Plume Dispersal in the Arctic Ocean - The Aurora Site at Gakkel Ridge

Master Thesis
at the Institute for Environmental Physics,
University of Bremen

by Jonathan Mette, born October 31, 1998 in Kiel

Supervisor: Dr. Maren Walter,
Institute for Environmental Physics
1st Examinor: Dr. Christian Mertens,
Institute for Environmental Physics
2nd Examinor: Prof. Dr. Torsten Kanzow,
Alfred-Wegener-Institute,
Helmholtz Center for Polar and Ocean Research

Bremen, May 16, 2025

Abstract

This thesis assesses the dispersal of the hydrothermal plume at the Aurora Vent Site in the Arctic Ocean, based on observational data and complemented by a numerical ocean model. The theoretical background of hydrothermal plumes in the Arctic is presented and the methods used are explained. This includes the processing of data acquired from a CTD probe, water samples and an oceanographic mooring with respect to the hydrographic setting and to the tracers for identification of the hydrothermal fluid. In addition a setup for simulating the plume dispersal with the Regional Ocean Modelling System is described. The observational results reveal a plume that ascends up to a height of 1200 m and spreads laterally to atleast a distance of 2500 m, although a strong core is confined to much smaller area. The plume dispersal is highly inhomogeneous for the different investigated tracers. This, as well as the small horizontal extent is explained by the presence of slow currents that are altered by tidal or inertial oscillations. A similar vertical extent can be obtained from the model simulation. However in regards to the currents and horizontal extent, the simulation shows large discrepancies compared to the observations, therefore suggestions for improving the model setup are presented.

Contents

Chapter 1.

Introduction

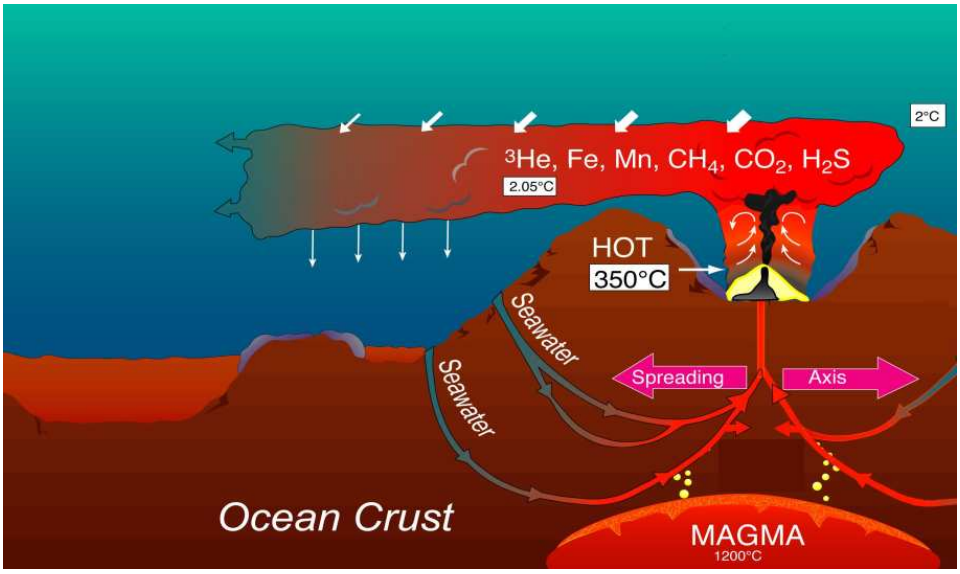

Figure 1.1.: Schematic of a hydrothermal vent system. Water gets entrained into the upper crust, where it is heated by magma sources, which often occur along spreading ridges. When the fluid exits, it is hotter and carries a variety of chemical species. As it rises it mixes with surrounding water and cools down until it reaches a layer of the equilibrium density. There it spreads out laterally and particles can precipitate. Modified from [5].

Hydrothermal venting is a key process for investigating seafloor-ocean interactions. It describes the process by which seawater is entrained into the crust and forced out again by heat sources, often occurring at oceanic ridges. Hydrothermal venting plays an important role for the flux of heat and chemical species such as ^{3}He from the lithosphere to the ocean [9][38]. The discharged hydrothermal fluid features a very different composition than the surrounding seawater, reacting with the host rocks and becoming enriched in dissolved minerals and gases. Due to its higher temperature, it is less dense than the surrounding

seawater and rises, forming the hydrothermal plume. As it mixes and cools during its ascent, the fluid reaches a density equilibrium and spreads horizontally with the ocean currents. This process is illustrated in Figure 1.1. The hydrothermal plume also modifies classical oceanographic properties [37]and the fluids can be the basis for vent specific ecosystems based on microbial communities that feed on the dissolved gases [57].

In the past the abundance of hydrothermal venting was attributed to the spreading rate of oceanic ridges [7]. However, discoveries on ultra-slow spreading ridges proved otherwise [19]. With the plume rise height being dependent on the heat flow from the vent, observations of the plume can provide further insight into into this question, as well as into the geologic environment, such as the host rock composition or geologic activity. One such slow-spreading ridge is the Gakkel Ridge in the Arctic Ocean. It hosts the Aurora Vent Field, one of the few confirmed hydrothermal vents in the Arctic, making it a highly interesting target. A selection of vents in this field are displayed in Figure 1.2. The vent field, discovered in 2014, covers the flank of a seamount within the axial valley of the ridge. It has been already targeted by several expeditions but is difficult to access due to year-round sea ice cover.

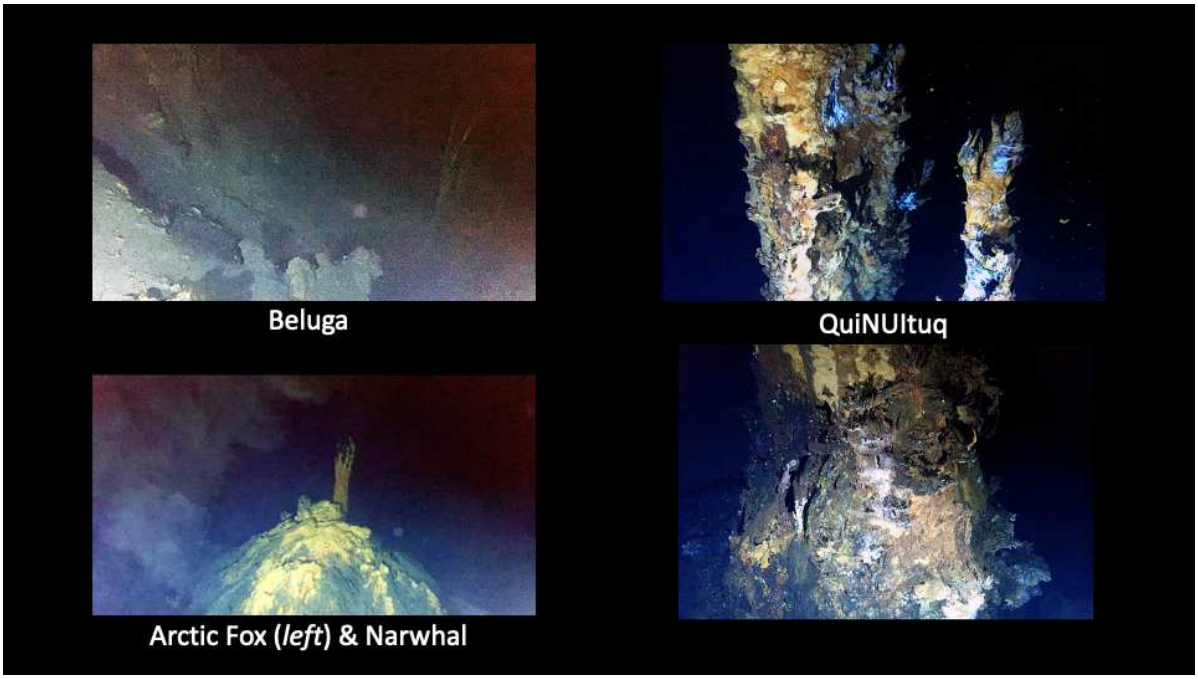

Figure 1.2.: Selection of different vents at the Aurora Vent Field. The images were taken during a Remotely Operated Vehicle (ROV) dive at the expedition *PS137*. Figure from [49].

With all this in mind, this thesis aims to

- asses the dispersal of the Aurora hydrothermal plume in vertical and horizontal dimensions,
- estimate the heat flux of the Aurora Vent Field,
- and investigate its interaction with the hydrography on longer time scales

It is mainly based on observational data, collected during the research cruise *PS137* aboard *RV Polarstern* in 2023. To complement these observations, a numerical ocean model is utilized, which together with data from a one-year mooring deployment on site, allows for a longer time period to be investigated. The plume dispersal is simulated with the Regional Ocean Modelling System (ROMS)[54], inspired by a similar study at the Endeavour segment of the Juan de Fuca Ridge [66].

Chapter 2.

Background

2.1. Hydrography of the Arctic Ocean and Gakkel Ridge

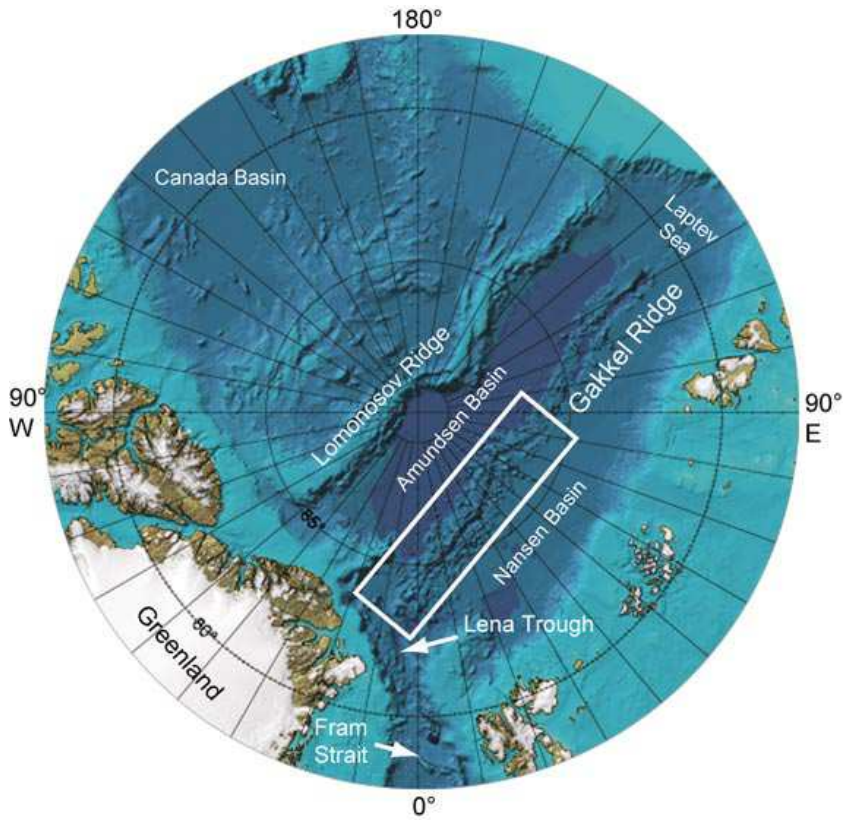

Figure 2.1.: Overview map of the major bathymetric features of the Arctic Ocean. Figure from [8].

The water column in the Arctic Ocean can be divided into a surface layer (approximately 0 m – 200 m), an intermediate layer (200 m – 800 m) and a deep layer (800 m to the bottom)[56]. The properties of the surface layer are controlled by ocean-ice and ocean-atmosphere in-

teractions while the intermediate layer, separated by the Arctic halocline, is influenced by Atlantic water inflow through the Fram Strait into the Eurasian Basin. Stratification in the Arctic Ocean is governed by salinity. Sills, separating the Arctic from the other oceans, cause the deep water to be highly isolated and homogenous [50]. Near the Gakkel Ridge, which divides the Eurasian Basin into the Nansen and Amundsen Basins, there is even evidence of a lower layer of water that is also highly homogeneous but warmer than most of the deep layer (see figure 2.2). This effect is caused by geothermal heating, where also hydrothermal venting plays a role [12][56]. Horizontal transport in the Arctic basins is mostly constrained by the height of the ridges separating the basins, such as the Gakkel Ridge with a minimum water depth of 1350 m [17] or the Lomonossov Ridge separating the Eurasian and Canadian Basins with a minimum water depth of 1700 m. The same basins shape mostly cyclonic circulation patterns in the respective depths [56].

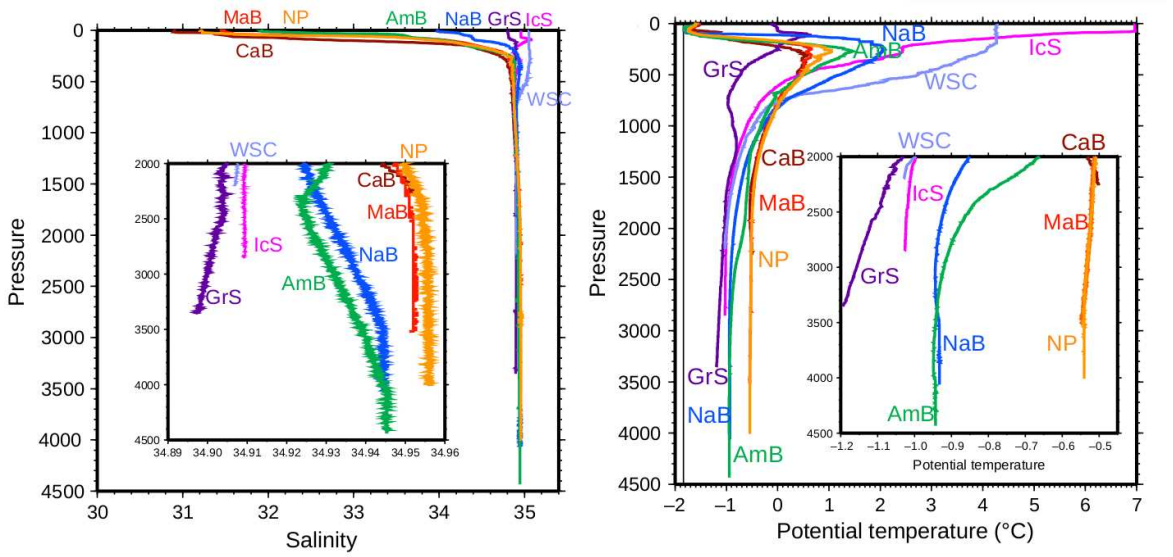

Figure 2.2.: **(a)** Salinity and **(b)** potential temperature versus pressure at various stations in the Arctic Ocean. Water masses in the different Arctic basins are highly homogeneous in the deep and bottom layers below 1700 m. Measurements at stations in the Nansen (NaB, blue) and the Amundsen Basin (AmB, green) next to the Gakkel Ridge show also a small increase in potential temperature towards the seafloor due to geothermal heating. The other stations are denoted as following: Canada Basin (CaB), Makarov Basin (MaB), North Pole (NP), West Spitsbergen Current (WSC), Greenland Sea (GrS), Iceland Sea (IcS) and Norwegian Atlantic Current (NaC). Figure from [56].

The hydrography within the valleys of mid-oceanic ridges such as the Gakkel Ridge is poorely studied, with only sparse hydrography observations available. This is especially true for the Arctic Ocean and the Gakkel Ridge. Investigations at the Mid-Atlantic Ridge revealed complex current systems that are strongly impacted by the topography. Observed

features include mean flows along the valley axis and subsequent recirculation, inflow into the valley across the flanks, enhanced diapycnal mixing through topography interactions and oscillations at tidal and near-inertial frequencies [34][58], which in principle can also be expected to play a role at the Gakkel Ridge.

2.2. Hydrothermal Plume Structure

When the hot hydrothermal fluid enters the ocean, it has a higher temperature and therefore a lower density than the surrounding water. This density difference causes the fluid to ascend. In the most idealistic model with a constant density ocean it would rise permanently, but several factors influence the propagation, which can be described as in [39]: First, the shear stress at the boundary between the plume and the surrounding water creates turbulence that entrains more dense water into the plume as shown in Figure 2.3. This dilutes the plume and reduces the overall density of the fluid as it rises. Second, in a realistic ocean the surrounding water is stratified, so the density changes with depth. The plume therefore reaches an equilibrium at a certain depth, where the density of the horizontal layer is equal to the density of the (already mixed) plume and stops rising. The momentum of the ascending fluid can cause an overshoot above the equilibrium layer and a subsequent fall back. Finally, cross-flow currents can modify the entrainment rate and therefore the density change and also the general propagation direction of the plume [35]. The ascending part of the plume is often referred to as the rising or buoyant plume, while the part which already reached a density equilibrium is the effluent or non-buoyant plume. In the non-buoyant part, the plume spreads laterally along isopycnals by horizontal advection and can extend over large distances.

The maximum rise height z_{max} of the plume allows the calculation of the heat flux as a measure for the amount of energy leaving the seafloor by hydrothermal venting as shown in [39] and summarized in [16]. It can be measured with reasonable effort. The rise height z_{max} can be described based on [59] as

$$z_{max} = 5 \cdot \left(\frac{F_0}{\pi}\right)^{1/4} N^{-3/4} \tag{2.1}$$

where 5 is an empirical constant, F_0 is the buoyancy flux and N is the Brunt-Väisälä frequency. N describes the stability of a fluid parcel in a stratified medium. When the fluid is vertically displaced, it experiences a restoring force resulting in an oscillation with the

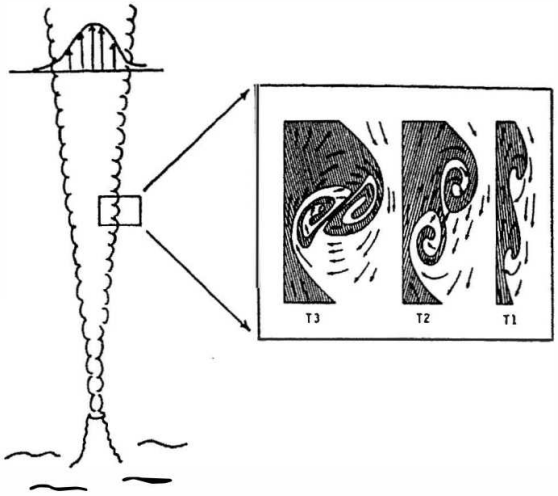

Figure 2.3.: Schematic of the entrainment of surrounding water (white) into the rising plume (black) by turbulence at different states of time (T1-T3). The upward arrows represent the resulting horizontal structure of the momentum. Figure from [39].

frequency N. It is given by

$$N^2 = -\frac{g}{\rho_0}\frac{d\rho(z)}{dz} \tag{2.2}$$

with g as the gravity acceleration factor, ρ_0 as the background density near the source as the reference density and $\frac{d\rho(z)}{dz}$ as the change of density with depth. In this work, the density gradient is not expressed as the in-situ density but the potential density anomaly σ_θ. It is now possible to calculate the heat flux H of the vent from the buoyancy flux F_0 as described in [60] by

$$H = F_0\frac{\rho_0 c_p}{g\alpha} \tag{2.3}$$

where c_p is the specific heat capacity of the fluid and α is the thermal expansion coefficient. This results in the heat flux being

$$H = \frac{\rho_0 c_p \pi}{g\alpha}\left(\frac{z_{max}}{5}\right)^4 N^3 \tag{2.4}$$

and depending on the measurable quantities ρ_0, z_{max} and $\frac{d\rho(z)}{dz}$.

2.3. Hydrothermal Plume Tracers

The detection of hydrothermal plumes and their intensity and dispersion can be observed by several tracer quantities, which are briefly described in this section. All of these tracers can vary for different vent sites and their observability depends on the composition of the surrounding water mass. In most cases, the differences between the plume fluid and the surrounding water mass decrease with the distance from the orifice towards small differences to no differences in the equilibrated, non-buoyant part due to entrainment and mixing. Therefore it can be useful to examine these quantities as the deviations Δ from the expected water mass without plume influence.

Temperature, Density and Salinity

Since the buoyant part of the hydrothermal plume is exerted with a higher temperature T and lower density ρ than the surrounding water, these two quantities can be used as plume tracers, as shown in [37]. Salinity S offers the same possibilities for some sites, but may also be lower in the plume. The potential temperature θ denotes the temperature of a fluid parcel that is moved adiabatically to a reference pressure (usually sea surface pressure p_0). This allows for a better comparison of temperatures at different pressures and therefore different depths.

The water density ρ is a function of salinity, temperature and pressure:

$$\rho = \rho(S, T, p) \tag{2.5}$$

For ρ it is often convenient to subtract the density of pure water and present the density anomaly σ:

$$\sigma = (\rho - 1000\,\mathrm{kg/m^3}) \tag{2.6}$$

A similar correction as for the temperature can be applied to density, resulting in the potential density anomaly, which is the density anomaly calculated from potential temperature θ:

$$\sigma_\theta = \sigma(S, \theta, p_0) \tag{2.7}$$

This does not take into account the pressure effect on salt and temperature expansion coefficients, which leads to the dependence

$$\sigma_p = \sigma(S, \theta, p) \tag{2.8}$$

with p as a value in the pressure range of interest.

The salinity S is derived by comparing the measured conductivity of the sample with the conductivity of a standard solution and is often given in practical salinity units (PSU) which is a dimensionless quantity. The calculations for these properties can be found in the TEOS 10 standard [29]. It is important to note, that some software modules used for processing *SeaBird* CTD data still use the old standard, EOS 80 [25].

Electron Reduction Potential

Hydrothermal fluids can be characterized by an increased amount of reduced chemical species. Their reactive potential can be measured as the electron reduction potential, in short E_h [61] (also called ORP). Sensors for E_h are subject to strong drift and hysteresis effects, as well as long response and relaxation times, which presents challenges when comparing different measurements. It is useful to analyze not only the direct E_h values but the time derivative [10], denoted in here as dE_h/dt. This allows for a better comparison, because the influence of drift and and partially hysteresis can be countered. For an increase in reduced species in a fluid, such as in a hydrothermal plume, E_h decreases, resulting in negative values in dE_h/dt.

Turbidity

Turbidity is a measure for the amount of particles in the water. Hydrothermal fluids often carry dissolved matter and transport them during their displacement, where they eventually precipitate out as particles. Turbidity can be measured with a nephelometer, which consists of a light source and a light detector. The more particles there are in the water in front of the source, the more light is scattered back to the detector. The amount of light scattered back is expressed in nephelometric turbidity units (NTU).

Helium Isotope Ratio

Helium in the Earth system can be characterized by the ratio R of the stable isotopes ^{3}He and ^{4}He with R_a as the characteristic ratio of atmospheric helium. As described in [48], helium fluxes into the ocean that alter the equilibrium between oceanic and atmospheric concentrations consist mainly of the uptake of atmospheric helium ($R = R_a$) by turbulence at the surface, the decay of tritium from anthropogenic sources to tritiogenic ^{3}He and the supply of primordial ^{3}He from the crust and mantle material. Therefore the isotope ratio is altered by the later two in the deep sea and one can utilize increased ratios as a tracer for primordial helium supply if the tritiogenic contribution is known. Primordial helium fluxes to the ocean occur at discrete locations which can be volcanic hotspots or mid-oceanic ridges. On these ridges hydrothermal circulation is a part of this flux and the hydrothermal fluid is enriched with primordial ^{3}He so the isotope ratio of the fluid is changed. This difference is described by the quantity δ^3He with

$$\delta^3\mathrm{He} = \left(\frac{^3\mathrm{He}/^4\mathrm{He}}{R_a} - 1 \right) \cdot 100 \tag{2.9}$$

The helium isotope ratio is not altered by chemical or biological processes in the ocean, making it an inert tracer for hydrothermal fluids, that can also be used as a dilution factor.

2.4. The Gakkel Ridge and the Aurora Vent Field

The Gakkel Ridge as an ultra-slow spreading ridge features a spreading rate of 14.5 mm/y – 13.5 mm/y in the area of interest, the western volcanic zone [45]. Previous studies attributed the frequency of hydrothermal vent sites per ridge kilometre F_s linearly to the spreading rate of the ridge but these studies were mostly based on medium to fast spreading ridges [7][8]. However, research about the Gakkel and the South West Indian Ridge (SWIR) show that this relationship does not hold for ultra-slow spreading ridges, when the magmatic delivery rate is also considered: When F_s is normalized by the magmatic delivery rate, the very low magmatic heat supply at the Gakkel Ridge leads to a high normalized site frequency as can be seen in Figure 2.4. This implies that ultra-slow spreading ridges are much more efficient at sustaining hydrothermal venting and suggests that the abundance of venting is controlled not only by the spreading rate, but by also other, partially still unknown factors [8][9].

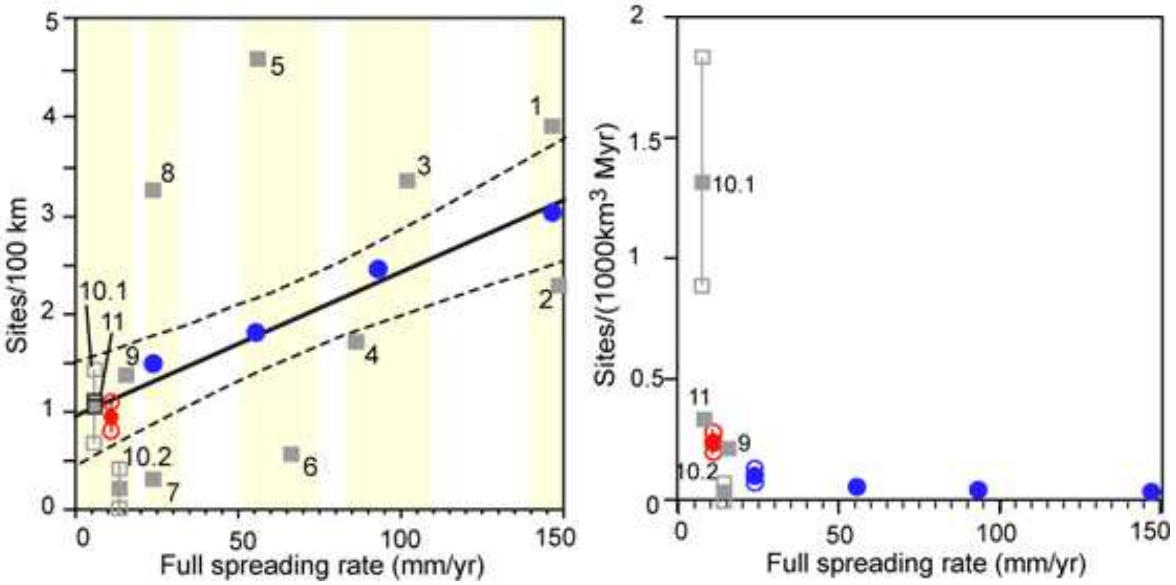

(a) **(b)**

Figure 2.4.: **(a)**: For the site frequency in relation to the spreading rate, the ultra-slow spreading ridges align in the linear trend. The gray squares mark individual ridges or ridge segments with 10.1 and 10.2 as the South West Indian Ridge and 11 as the Gakkel Ridge. For the blue and red markers, the data are categorized by spreading rate categories, with the solid symbols as mean values and the open symbols as maxima and minima, where available. The solid line shows a least squares regression fit with the dashed lines as 95 % confidence intervals.
(b): The site frequency normalized by the magmatic heat budget is much higher for ultra-slow spreading ridges, suggesting that factors other than the spreading rate alone control the abundance of hydrothermal venting at ultra-slow spreading ridges. Figures from [8].

The Aurora Vent Field is located at the southern part of the Gakkel Ridge in the Arctic Ocean (see Figure 2.6), on the southeastern slope of the Aurora Seamount, which lies within the ridge valley. The deepest point of the ridge valley next to the seamount is at 4390 m, while the ridge flanks reach up to 1000 m depth on the east side and 2700 m on the west side, as can be seen in Figure 2.5.

With first evidences documented in 2003 during the AMORE expedition [19], the first hydrothermal vent at Aurora was discovered by a combination of dredge hauling, CTD measurements and observations by the Ocean Floor Observing System (OFOS) during the *PS86* expedition at 82.897 166° N, 6.255 333° W at a depth of approximately 3900 m [13]. Further expeditions returned to the vent field, discovered more vents at the site and retrieved oceanographical, biological, chemical and geological samples with ROV support [49].

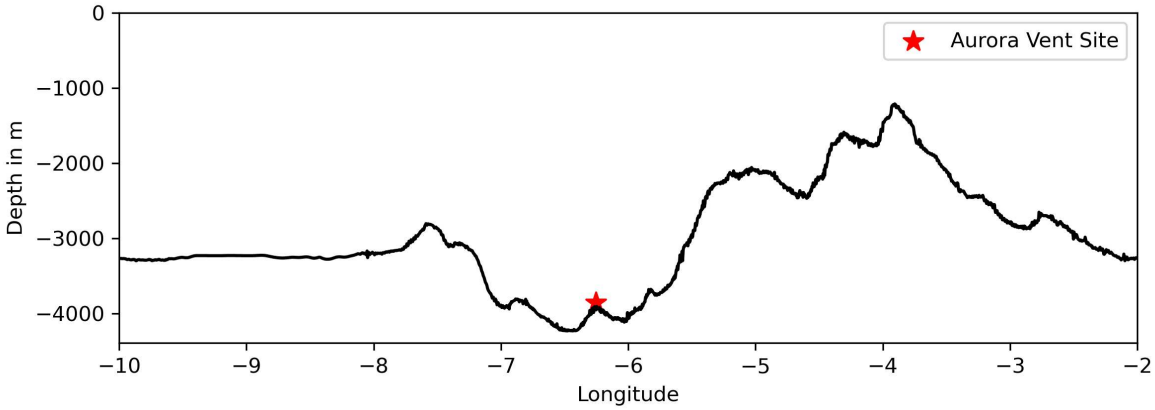

Figure 2.5.: Bathymetry along the latitude of 82.897 166° at the location of the Aurora Vent (marked with a red star). Data based on [26].

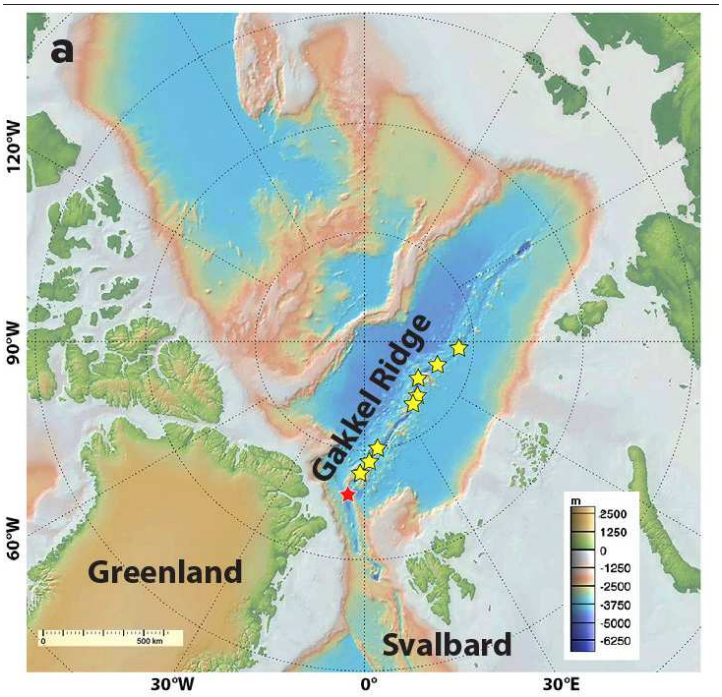

Figure 2.6.: Location of the Aurora Vent Site (red) discovered during the expedition PS86 [13] and other observed hydrothermal plume signals along the Gakkel Ridge from the AMORE expedition [19]. Figure from [47].

Although several expeditions have already targeted the Aurora Vent Field, data on the hydrothermal plume dispersal are still sparse. Sea ice covers the location year-round, making it difficult to conduct instrument work on a fixed location. The ship's manoeuvrability is limited by drift direction and speed of the ice, which leads to short observation time frames for instruments such as ship-borne CTDs, ROVs and camera sleds. To counter the low temporal resolution of measurements (ship expeditions are also only possible in sum-

mer) a mooring consisting of CTD logging instruments and acoustic current meters was deployed at the vent site between summer 2022 and 2023 [49].

Previous observations of the Aurora plume revealed diffuse venting with clear, shimmering water associated with low temperature venting as well as high temperature ($\geq 300\,^{\circ}C$) fluid colored dark by metal sulfides. Water samples contained elevated amounts of hydrothermal tracers such as primordial helium, methane and manganese at depths between 2800 m to 3700 m [27].

Chapter 3.

Observational Methods

3.1. CTD Operations

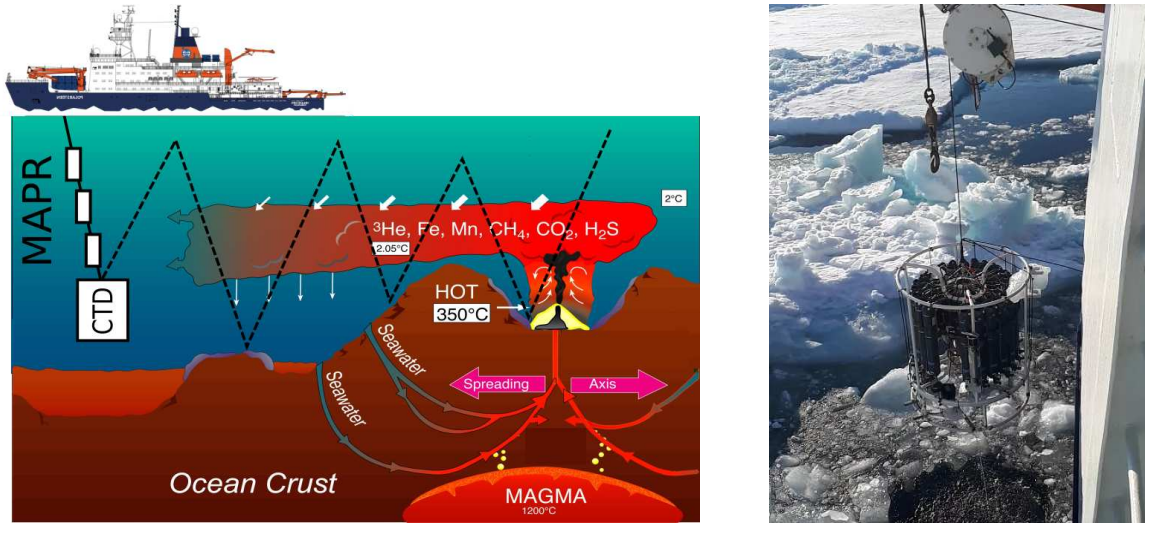

(a) **(b)**

Figure 3.1.: **(a)** Principle of Tow-Yo operations. As the ship moves forward and the CTD is lowered and heaved a larger area is covered, resulting in a cross-section-like profile. MAPRs, which are mounted on the cable above the CTD, increase the vertical resolution. The chance to measure the hydrothermal plume is increased, especially for the non-buoyant part, which spreads horizontally over larger distances. Based on [5].
(b): Recovery of the CTD rosette. Operation may be restricted by the presence of ice cover, which can limit the ships maneuverability or cause sudden stops of deployments.

One of the the main strategies to investigate hydrothermal plumes is the use of a ship-borne probe, measuring conductivity, temperature and depth (short CTD). The principals

of operation as used on the cruise *PS137* are described in this section and are fully documented in [49]. The CTD surveys aimed to assess the spatial distribution of the plume in horizontal and vertical dimensions, as indicated by the tracers described in Section 2.3 and to subsequently allow conclusions about the hydrothermal activity at this part of the Gakkel Rigde. Additionally the surveys guided the collection of water samples for further biogeochemical analysis such as for δ^3He.

Instrument Setup

The CTD probe is a multi-sensor package that can be lowered from a research vessel and provides real-time data as well as the option to collect water samples with the so-called rosette. Additional sensors can be mounted on the system, where the relevant for hydrothermal plume research are the sensors for electron reduction potential (E_h) and turbidity. The CTD sensor setup is documented in Table A.1. The CTD features two sensor groups providing independent measurements of temperature and conductivity, which are the basis of the derived quantities for plume anomaly detection. These can be compared to verify the basic functionality. If the results are similar for both sensor groups it is sufficient to base the investigation in this work on one of these groups alone.

The CTD is complemented by Miniature Autonomous Plume Recorders (MAPR)[6] which also measure temperature, pressure, turbidity and E_h but are self-contained and mounted on the cable above the CTD for each deployment. This increases the vertical spatial resolution. The CTD-based sensors measure with a resolution of 24 Hz while the MAPRs were set to 0.2 Hz due to battery limitations. The MAPRs and the E_h sensor for the CTD during *PS137* were provided by Sharon Walker, *Pacific Marine Environment Laboratory (PMEL)*. The turbidity sensor on the CTD was not operational during cruise *PS137*, so only turbidity measured by the MAPRs is considered in this work. The sensors were set to 5× gain which corresponds to a measurement range of 500 NTU. The underwater position of the CTD rosette was georeferenced by an acoustic position tracker. Additionally, at some CTD stations a self-contained acoustic current meter (*Nortek* Aquadopp) was mounted on the rosette for current measurements. At one of these stations, *PS137-028-01*, the CTD rosette was stationary in the vertical for a duration of approximately 2 h and 20 min. Only for this station the current measurements of the Aquadopp instrument are used.

Observation Strategy

When searching for plumes, the CTD is deployed in a special way: As the ship moves forward at a speed of 0 to 3 kn, the CTD is lowered and heaved repeatedly like a yo-yo, travelling along zig-zag fashioned pattern across the area of interest. Because it is towed behind the ship, this operation is called "Tow-Yo" or, if the ship movement (and CTD operation) is restricted by the surrounding ice floes, a "Floe-Yo". Tow-Yos increase the chance of intersecting the plume compared to a stationary CTD cast, as sketched in Figure 3.1. The area of interest can therefore be surveyed systematically for hydrothermal plumes. The tracks of CTD Floe-Yo's on *PS137* are shown in Figure 3.2.

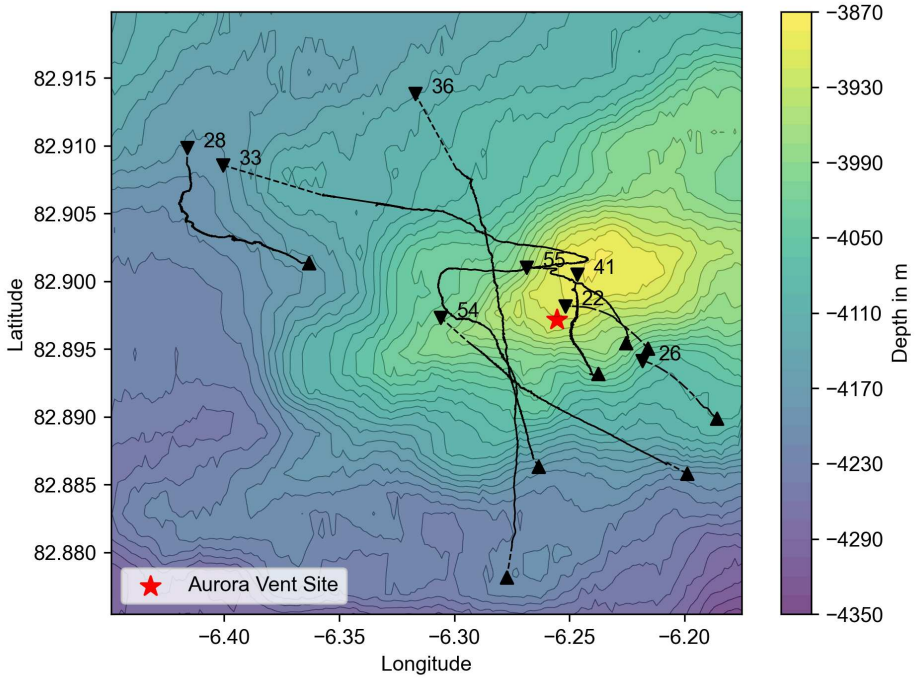

Figure 3.2.: Tracks of the CTD stations at the Aurora Vent Field during cruise *PS137*. The numbers denote the station number (see Table 3.1) and the downward (▼) and upward (▲) pointing triangles indicate the start and end points of the track. Tracks with positions from the acoustic tracker are represented as solid lines, where these are not available the ship's position is shown as a dashed line.

The presence of different water masses and thus of hydrothermal fluid can be detected in real time by the change in the measured quantities. Turbidity, as the amount of particles in the water is expected to increase, as well as the potential temperature anomaly $\Delta\theta$. The electron reduction potential (E_h) also changes, but can only be measured as a relative quantity, without comparison to a reference point.

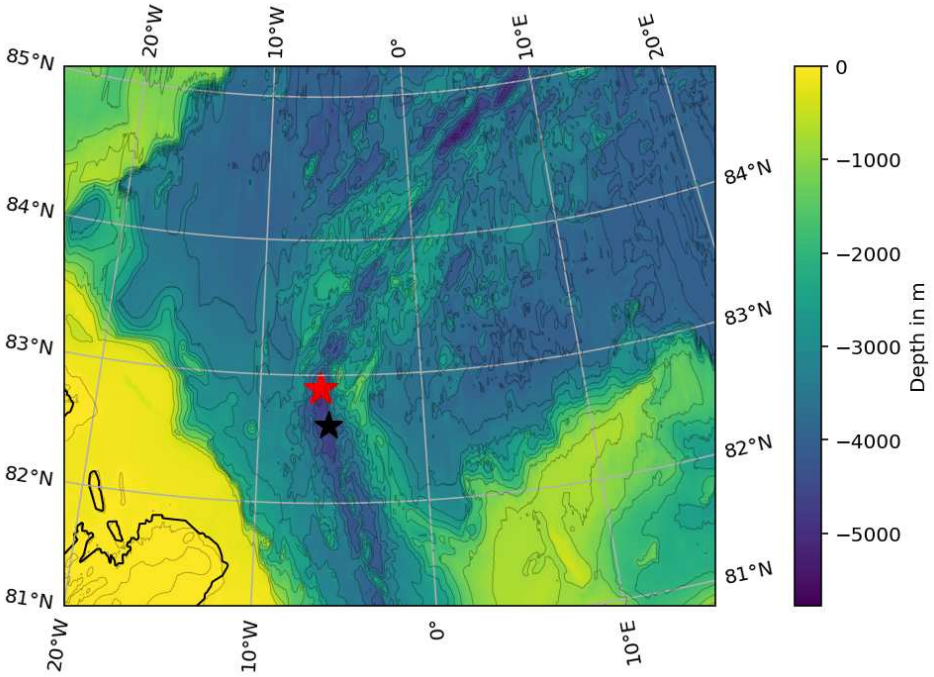

Figure 3.3.: Overview of the vent site marked by the red star and the background station *PS137-018-01* to the south of it marked by the black star and its locations along the Gakkel Ridge northeast of Greenland. The bathymetry data are taken from [26].

The data from the CTD stations listed in Table 3.1 are presented and evaluated in the following chapters. Station *PS137-018-01* was intended as a background measurement at a location where no hydrothermal plumes were expected, about 17.5 NM (or 32.5 km) away from the Aurora site, as can be seen in Figure 3.3.

3.2. Helium Isotope Sampling

To determine the helium isotope ratio, water samples are collected using the water sampling system attached to the CTD rosette. The helium isotope ratio is the most inert and therefore the most reliable tracer of hydrothermal fluid, so δ^3He results from discrete water samples can complement the real-time CTD data to assess the spatial distribution of the plume. Niskin sample bottles can be closed remotely, with the time of closure usually guided by the real-time measurements of the other quantities. Immediately after the rosette arrives back on deck, water is sampled from the Niskin bottles into airtight copper tubes and analyzed post-cruise at the *Helium Isotope Laboratory Bremen*. There the concentrations of ^{3}He and ^{4}He are measured in a mass spectrometer which gives δ^3He

Station	Location	MAPR	Aqua-dopp	Helium	Position data	Comments
PS137-018-01	Lena Trough 82.609 672°N 5.886 912°W	X	X	X		intended as background
PS137-022-01	Aurora					
PS137-026-01	Aurora	X	X	X		
PS137-028-01	Aurora	X	X	X	X	
PS137-033-01	Aurora	X	X	X	X	
PS137-036-01	Aurora	X	X	X	X	
PS137-041-01	Aurora	X			X	
PS137-054-01	Aurora	X	X	X	X	
PS137-055-01	Aurora	X	X	X	X	

Table 3.1.: Overview of the CTD stations and their measurements. Stations that had to be aborted are already excluded. Station *PS137-018-01* was intended as a background station with a large distance to the Aurora site. Based on [49].

as the deviation of the $\frac{^3He}{^4He}$ ratio from air in percent. The principle of the analysis is described in detail in [55]. The influence of tritiogenic ^{3}He and possible deviations from the atmospheric ratio are not considered in this quantity and have to be discussed separately.

3.3. Vent Sampling

The Nereid Under Ice (NUI) deep submergence vehicle from the *Woods Hole Oceanographic Institution (WHOI)* sampled a high-temperature vent fluid and measured temperature directly from the orifice of a vent in the Aurora Field, providing a less ambiguous description of the plume fluid properties than compared to CTD surveys. The fluid sample was taken with a fluid sampler developed by Jeff Seewald, *WHOI* and analyzed post-cruise for the helium isotope ratio in the *Helium Isotope Laboratory Bremen*, similar to the water samples described in Section 3.2. The measurements from this sampling are not the focus of this work, but are used for discussion in Chapter 6.

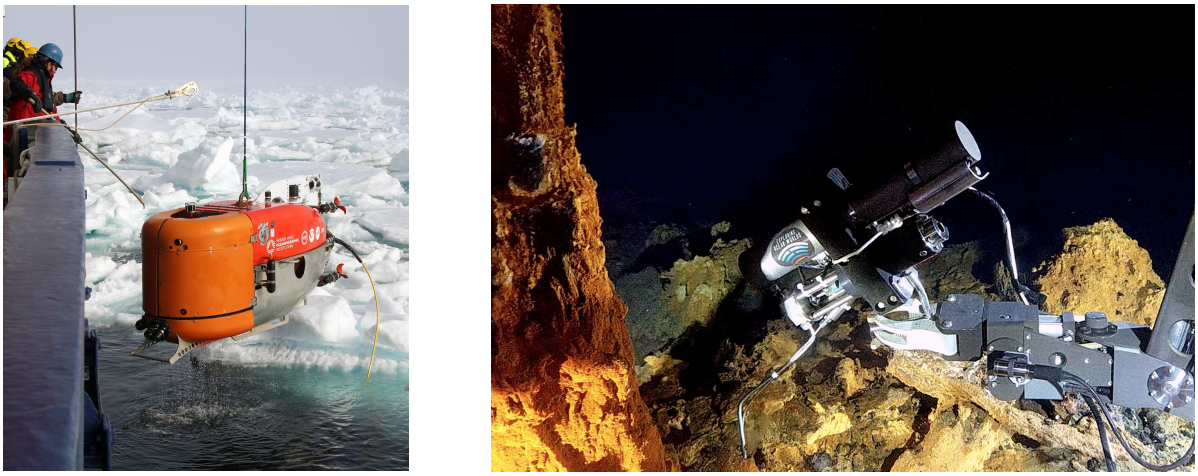

(a) **(b)**

Figure 3.4.: **(a)** NUI vehicle being recovered after a dive.
(b) NUI vehicle sampling the exiting hydrothermal fluid next to the *Lander* site.
Pictures courtesy of the PS137 NUI team. Copyright WHOI.

3.4. Mooring

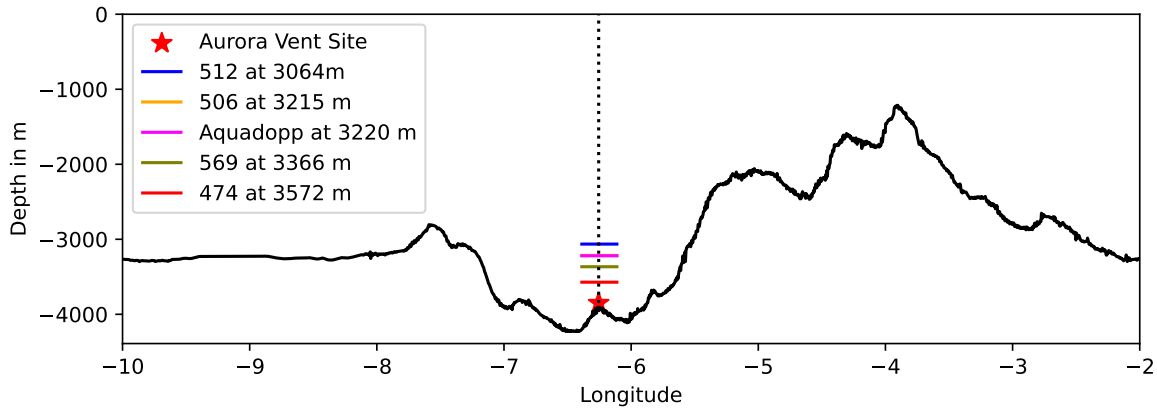

Figure 3.5.: Depth of the four current meters of the mooring and the Aquadopp measurement of the CTD in relation to the bathymetry along the latitude of 82.897 166° at the position of the Aurora Vent (marked by the red star). Data based on [26].

Vessel-based methods such as the CTD system are limited to a short time period, during the visit of the site. Therefore they were complemented by a series of moored instruments that measured hydrographic properties at the vent site more continuously for almost one year, providing a long-term context for the CTD observations and more data on the general hydrographic conditions. The mooring was deployed between 25/07/2022 and 02/07/2023 at the site at 82.897 766° N and 6.250 716° W and consisted of four acoustic current meters

and five CTD loggers (setup in Table A.2). The position of the four current meters relative to the a bathymetry cross section is shown in Figure 3.5. For more documentation see [32] and [49].

3.5. Data Processing

The data collected from the observations were processed in different ways, depending on the device used. The complete software documentation can be found in B.1.

CTD & MAPR Data

The data collected with the *SBE 911plus* CTD were first processed using the *SeaBird* data processing software according to the manual [51] with the following modules:

- Raw files were converted to ASCII readable files.
- All measurements except turbidity and E_h were filtered with "Wild Edit" based on the departure from the standard deviation.
- All measurements except turbidity and E_h were filtered with "Filter" with a low pass.
- A correction to the conductivity measurements was applied to both conductivity sensors with "Cell Thermal Mass".
- The measurements during each sample bottle closure were extracted into a separate file with "Bottle Summary".
- All measurements were averaged to 1 s intervals with "Bin Average".

Additional data processing was done in *Python*. This includes the merging of the CTD measurements with position data from the ship's navigation system and from the acoustic position tracker based on timestamps. In the acoustic tracker data timestamps were corrected manually and outliers in the position were excluded based on the interquartile range. The position data and the helium data from the laboratory analysis were merged with measurements during bottle closure based on the timestamp.

For the MAPR data, binary files were converted to ASCII-readable files, the pressure was corrected by a reference pressure before deployment and data before and after the deployment was removed. Again, position data was merged based on timestamps.

Various hydrographic properties such as potential temperature θ and potential density σ_θ derived from the in-situ measurements were calculated with the *GSW-Python* toolbox [24]. Since the MAPRs are not equipped with conductivity cells and therefore cannot measure salinity, their θ and σ_{3000} results are calculated based on an averaged salinity profile over all stations conducted at the vent site. For the plume tracer quantities several methods were employed which are described below in Chapter 3.5.

While conducting stations *PS137-018-01* and *PS137-028-01* the CTD rosette was stationary in the vertical at 3200 m for about 2 h and attached pumps for microbiological experiments were run (see [49]). This sections are excluded from the CTD data and discussed separately due to possible measurements errors and are further referenced as *PS13-018-01-level* and *PS13-028-01-level* respectively.

Plume Anomalies

Two different approaches to calculate the potential temperature anomaly were investigated, where the first is based on measurements from a reference station far away from the vent site and the second based on the θ-σ_θ relationship. The background station *PS137-018-01* was located about 17.5 nm south of the vent site, where no hydrothermal activity was expected. The θ-depth relationship from this station is fitted with a polynomial of a high order (here an order of 10 was used) excluding shallower layers with high θ variability (here above 2000 m). This fit is evaluated on the depth values of the station at the vent site and the result is subtracted from θ resulting in the potential temperature anomaly $\Delta\theta$. This approach will be referred to later as the background comparison.

The second method, based on [8], does not rely on such a background station. Here the θ-σ_3 relationship in the deep layer (below 2500 m) of the cast with the smallest θ anomaly in each station is used as the basis for a third-order polynomial fit. If a θ increase is nevertheless visible, that range is excluded from fitting, as described in the example in Figure 3.6. The coefficients are used to calculate another θ-depth profile which is again subtracted from the original θ, yielding $\Delta\theta$. This will be referred to as the in-station comparison later on. The most important aspects here are, that for the first approach no plume influence at the background station and no other strong differences in the compared profiles are

assumed, while for the second method already the fit can be modified by some plume influence in the measurement.

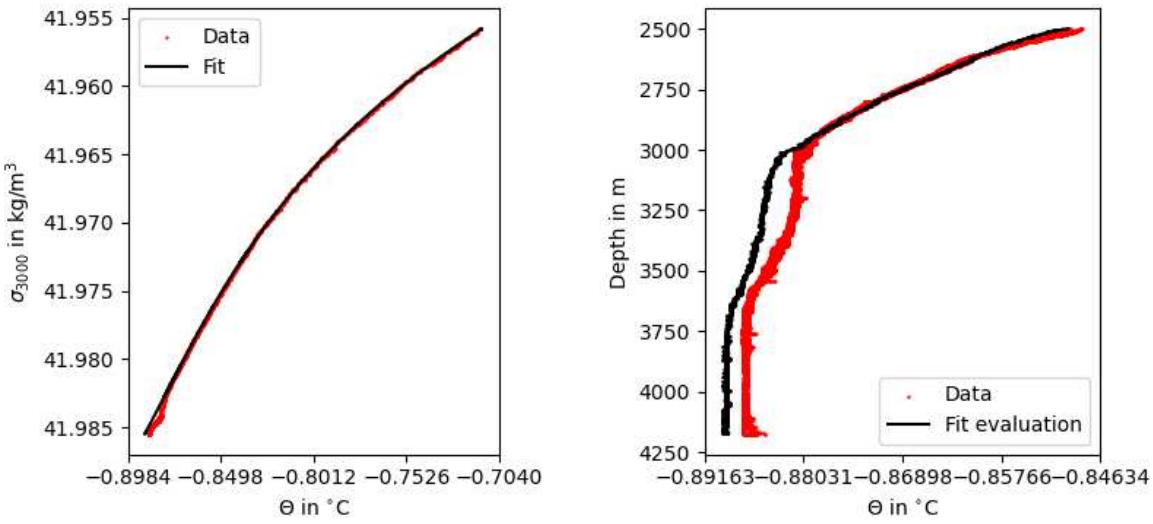

(a) **(b)**

Figure 3.6.: Example fits for the determination of $\Delta\theta$ utilizing the in-station comparison method for station *PS137-028-01*.
(a) Polynomial fit (black) of the θ-σ_{3000} relation (red). For the highest density values, a positive temperature deviation is visible marking the influence of the plume. For stations with similar increases, this range is excluded from fitting.
(b) Evaluating the fit on the θ profile (red) results in an idealized profile (black) without the influence of the θ increase visible in Figure 3.6a. The deviation is defined as the resulting potential temperature anomaly $\Delta\theta$. It is visible, that not all plume influence could be removed from the idealized profile, causing the increase in θ between 3000 m and 3600 m.

To use E_h measurements from the E_h sensor as a plume tracer, the discrete difference for the last 30 s is calculated. This is equivalent to 30 values for the CTD and six for the MAPR data. The difference divided by 30 gives the averaged dE_h/dt in mVs^{-1}.

Anomalies in δ^3He were calculated by subtracting the mean as 7.146 % of all samples at the background station below 900 m, because shallower samples are often altered by surface processes.

Finally the turbidity anomaly is also calculated in two ways: First, as the difference to the background station and second, as the difference from the mean of each profile and per instrument in the range of 1000 m to 2700 m. Water masses above this layer are assumed to be influenced by surface and photic zone processes and below by possible vent fluid.

Outliers were removed based on the interquartile range and then the data were smoothed with a Savitzki-Golay filter before averaging.

Aquadopp Data

The current data of the stationary measurement conducted with the rosette-mounted Aquadopp were merged with the position data of the acoustic position tracker based on time stamps. The horizontal velocity components u and v were then corrected by the velocity calculated from the position change of the CTD rosette.

Mooring Data

The speed and direction data from the four RCM11 acoustic current meters were exported from the instruments as binary values and then scaled to the the instruments resolution range. Gaps in the timestamp data were filled by linear interpolation. For some sections of the analysis the u and v components were filtered with a 24-point Hanning window. The spectral analysis was performed using J. Lilly's Ocean / Atmosphere Time Series Analysis toolbox [36]. Positive and negative rotating components were filtered with the multitaper method as implemented in [46] with the time-bandwidth product $P = 16$ as the parameter controlling the number of adjacent frequencies used for the filter. The tidal frequencies f_{Tides} are taken from [28] and the Coriolis frequency f_C is calculated based on a latitude of 82°.

Chapter 4.

Regional Ocean Modelling System

The Regional Ocean Modeling System (ROMS) [54] is a numerical primitive equation ocean model, that uses terrain-following vertical and orthogonal-curvilinear horizontal coordinates. The ROMS model offers a variety of different configurations and adjustments as well as coupling with other models such as ice [15] or biological ones [23]. Input files such as the grid configuration and boundary forcings can be supplied by common *netCDF* format files.

This section describes aspects that are central to the simulation of the dispersal of the Aurora plume. The configuration of the model framework was guided by a study about the plume dispersal at the Endeavour segment of the Juan de Fuca Ridge [66] and in correspondence with its author. It is important to note that this is neither a documentation of all the options and capabilities of ROMS nor a complete description of the test setup, as that would go beyond the scope of this work. For the former, the ROMS Wiki and the ROMS forum provide extensive information, for the latter, the model setup can be found in the appendix B.2.

4.1. Time-Stepping and Output

For this work the setup is run with a time step length of 1 s for 669 600 steps corresponding to 31 days. The data is written to an output file averaged over 900 time steps resulting in 744 time steps in the output data.

4.2. Modeling Domain and Bathymetry

The construction of the grid is documented in this section. The grid construction is done using the *MATLAB* toolbox *GridBuilder* [31].

The location of the domain is chosen in a way, that main bathymetric features are included but also that the edges don't intersect with steep seafloor changes. The grid is orthogonal with a resolution of 256×256 cells, with each cell having a side length of $80\,\text{m} \times 83\,\text{m}$ with the location of the domain being shown in Figure 4.1a.

The bathymetry data is taken from [63] and was collected using a ship-based echosounder. This bathymetry data is the basis for the ROMS terrain-following vertical S coordinate, shown in Figure 4.1. To avoid steep changes between grid cells, the bathymetry is smoothed by negative adjustment. This is controlled by the grid stiffness parameter rx_0, which is a measure of the change in the topography relative to the mean water depth for adjacent cells [11]. The chosen target value for rx_0 here is 0.2.

The distribution of the vertical layers is controlled by several parameters: The number of vertical layers as chosen by the user, the vertical transform algorithm $V_{transform}$, the vertical stretching algorithm $V_{stretch}$, the surface stretching parameter θ_S and the bottom stretching parameter θ_B. $V_{transform}$ transforms the depth coordinate z to the ROMS own S-coordinate, while $V_{stretch}$ controls the depth-dependent stretching for each cell. For $V_{transform}$, the transformation described in [65] under (2) is the ROMS default option (option 2) and for $V_{stretch}$ the function described in [41] (option 4) and are the settings also used here. The non-dimensional vertical coordinate in the model, σ, which has values between -1 and 0 is transformed accordingly to water depth z for the analysis if the results. For an overview of the different options see also [65].

θ_S and θ_B control how much the cells near the surface or bottom are stretched. For this grid, the properties are set to $\theta_S = 0$ and $\theta_B = 3$, to achieve a high vertical resolution near the bottom. The distribution of vertical levels can be characterized by the Haney number rx_1. It describes how consistent a hydrostatic regime between the grid cells would be, with values less then 6 being considered as usable [18]. The grid properties for the grid are summarized in Table 4.1 and Figure 4.2.

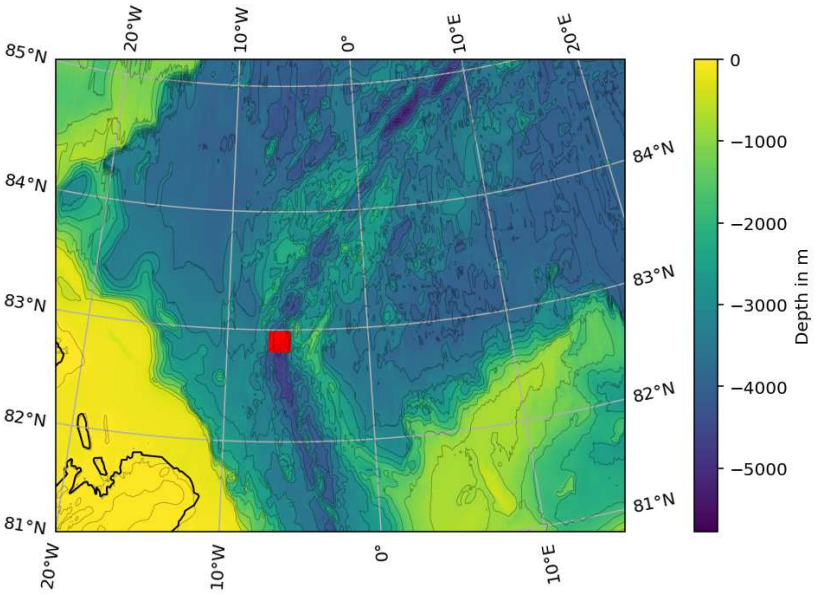

(a)

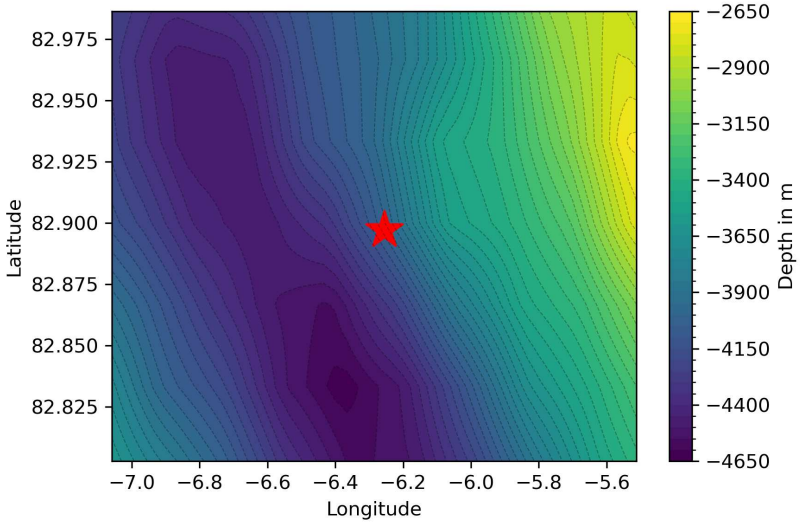

(b)

Figure 4.1.: **(a)** The location of the modeling domain within the Arctic Ocean is marked by the red square. Bathymetry data are taken from [26].
(b) Bathymetry inside the domain based on [63]. The Aurora Vent Field is marked by the red star. The domain consists of 256×256 orthogonal cells with a side length of $83\,\text{m} \times 80\,\text{m}$.

Vertical layers	30
$V_{transform}$	2
$V_{stretch}$	4
θ_S	0
θ_B	3
Orthog. error	0
rx_0	0.2
rx_1	0.443

Table 4.1.: The main grid parameters.

Figure 4.2.: Distribution of vertical layers in the grid. Figure generated with [31].

4.3. Initial and Boundary Conditions

ROMS can start the simulation with initial conditions in the domain, which can be provided by analytical functions or by a *netCDF* file. While the first option is useful for testing purposes, in this case data from the 3-hourly time-averaged Global Ocean Physical Multi Year reanalysis product [21] is used and interpolated to the ROMS grid.

The usage of boundary conditions is somewhat similar: it is possible to choose between boundary conditions that act with or without external values. For the first option, an example would be a closed boundary. For the second option, external values have to be provided as a *netCDF* file, like for the initial conditions. Here they are inferred from the same data product as the initial conditions [21]. Ocean-atmosphere fluxes for all variables are set to zero as a simplification representing permanent ice cover. The files for initial and boundary conditions were generated with a *MATLAB* script provided by G. Xu (see Appendix B.2). The vertical boundaries of the domain are specified as radiative and nudging boundaries [40]. This allows property fluxes in both directions across the boundary. The properties inside the domain can radiate outwards and in the opposite direction the grid cells at the boundary are nudged, i.e. influenced by the specified boundary conditions from the reanalysis data.

4.4. Bottom Flux Forcing

ROMS can include additional forcing *netCDF* files, that can be used to simulate the flux input from a hydrothermal vent. For simplicity, the input is treated as a point source (e.g. from one grid cell) and volume-less. The heat flux from the Aurora vent is estimated to be 180 MW as inferred from the observed maximum rise height of the plume, based on the plume tracer dE_h/dt measured by the CTD. The corresponding results are shown in Section 5.3 and the calculation is described in Section 2.2. An additional forcing file is used to describe the input of a passive tracer. This tracer represents the input of inert ^3He through the vent system and is only advected between the grid cells but does not interact with other properties. The amount of ^3He is quantified in this work in terms of the δ^3He ratio (see Section 2.3) but passive tracers in the model can only be described as mass particles in the unit of kg/m^3. Since this simulation focuses on the passive tracer as a visualization aid for the plume fluid dispersal, it is assumed for simplicity that 1 % of δ^3He can be represented by 1 kg/m^3 of the passive tracer. Based on measurements at an active chimney the amount of δ^3He which is delivered by the vent is assumed to be 650 %.

Both forcings are prescribed as an input to the grid cell associated with the vent location for each time step of the simulation, representing a continuous supply from the vent system. The forcing files were generated using a *MATLAB* script provided by G. Xu (see Appendix B.2).

4.5. Tidal Forcing

ROMS is able to infer the influence of tidal forcing and incorporate it as a lateral force. It is calculated from the gradient of the difference between the sea surface ζ and the sea surface, if it were in equilibrium with the tide generating forces, ζ_{EQ}. The resulting acceleration of the water mass a can then be described as

$$a = -g\frac{\partial}{\partial x}(\zeta - \zeta_{EQ}) \tag{4.1}$$

The equilibrium sea surface is calculated for each tidal constituent according to [4].

The tidal constituents are provided by the output of the Arctic Ocean Tidal Inverse Model [20]. It is an assimilation and forward model on a polar stereographic grid with 5 km resolution and provides gridded data for sea surface height and depth-integrated currents

for the tidal constituents. For the assimilation, data from tide gauges and satellite radar altimetry is used. The tide model output is written to ROMS input files in *netCDF* format using the *otps2frc_v5.m* script provided by the ROMS *MATLAB* suite [2].

Chapter 5.

Results

The basis of this chapter is the evaluation of CTD measurements. Figure 5.1 shows exemplarily some of the plume tracers at one station at the Aurora Vent Field. As the properties of seawater vary greatly near the surface and the shallower layer is not of interest here, it is neglected for better presentation, as in most of the figures in this section. The depth curve in black follows the lowering and heaving of the CTD rosette from the surface to the bottom, then yoyo-ing in the suspected plume depth and back to the surface. The potential temperature θ and potential density anomaly σ_{3000} match this pattern, with different amplitude and orientation. Here σ_{3000} is calculated with the reference pressure of 3000 dbar. In dE_h/dt there is an independent behavior: while it mostly varies around 0 mVs^{-1}, at one point the amplitudes become larger with a strong negative peak and a slow return to the original level. This can be interpreted as a clear signal of a hydrothermal plume.

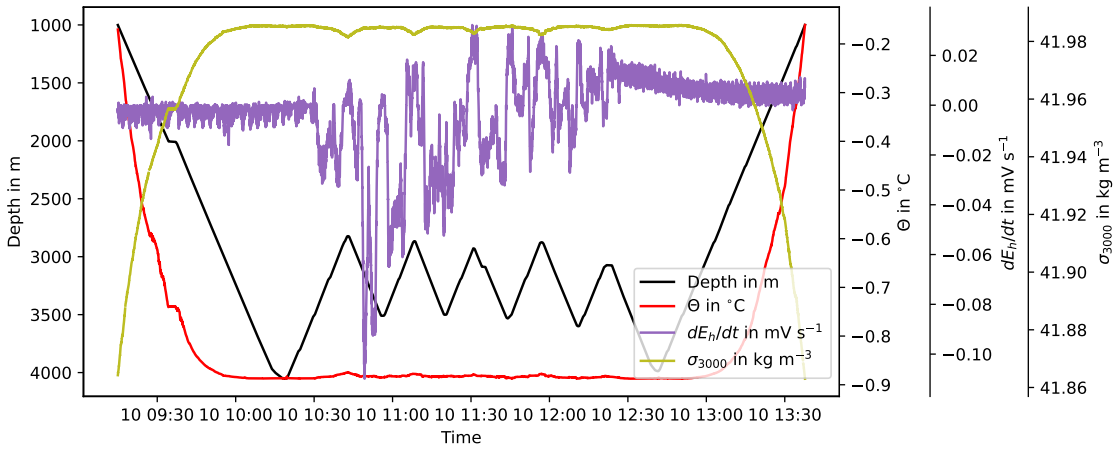

Figure 5.1.: Depth, potential temperature θ, dE_h/dt and potential density anomaly σ_{3000} versus time. The measurements show the data below 1000 m for station *PS137-036-01*.

For the other quantities, this depiction shows no such clear sign. If there are any in this station, their magnitude appears to be too small to be visible in here, so they need to be investigated in more detail.

5.1. Water Masses

The data measured by the CTD sonde can be analyzed in terms of the relationship between practical salinity S and potential temperature θ, which allows for the characterization of water masses by their potential density anomaly σ_{3000}. Figure 5.2 displays this relationship for the data collected at the vent site while Figure 5.2b is a close-up of the area of high σ_{3000} values. The characteristic relations of the different stations are mostly aligned with each other with different levels of θ. The aforementioned high σ_{3000} region has the largest deviation between stations: For station *PS137-041-01* θ increases relative to the overarching curve between 41.984 008 kg/m^3 to 41.985 337 kg/m^3, similarly for some data points of station *PS137-054-01*, but most strongly for station *PS137-033-03*. Some data points of the stations *PS137-022-01*, *PS137-026-01* and especially *PS137-028-01* are located at higher S values compared to the other stations.

Attributing the 3D geometric distance to the vent location to the data described above shows, that some stations were conducted closer to the vent than others (Figure 5.3). But the most interesting pattern can be observed in the close-up pf the high σ_{3000} values: Here the high S values correspond to measurements more than 2000 m from the vent. Conversely, data points very close to the vent (less than 250 m) follow a similar distribution with a curve of increased θ as those of station *PS137-041-01* in Figure 5.2b. The measurements of station *PS137-033-03* with the strongest θ peaks are also close to the vent, approximately 700 m. In all figures the resolution of the sensor for determining salinity is visible, as data points are distributed over some discrete x-axis values.

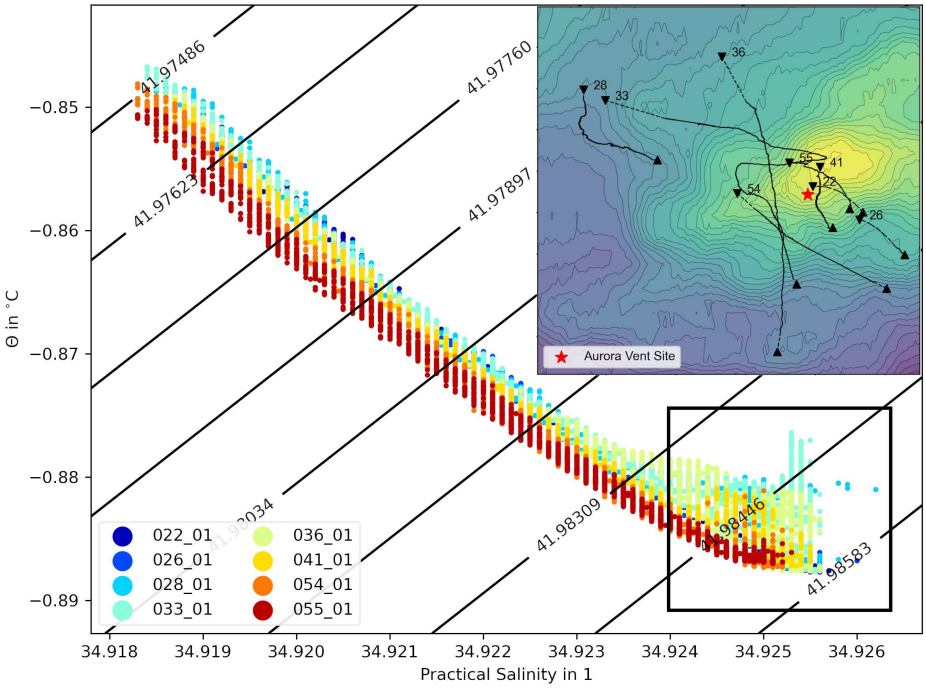

(a)

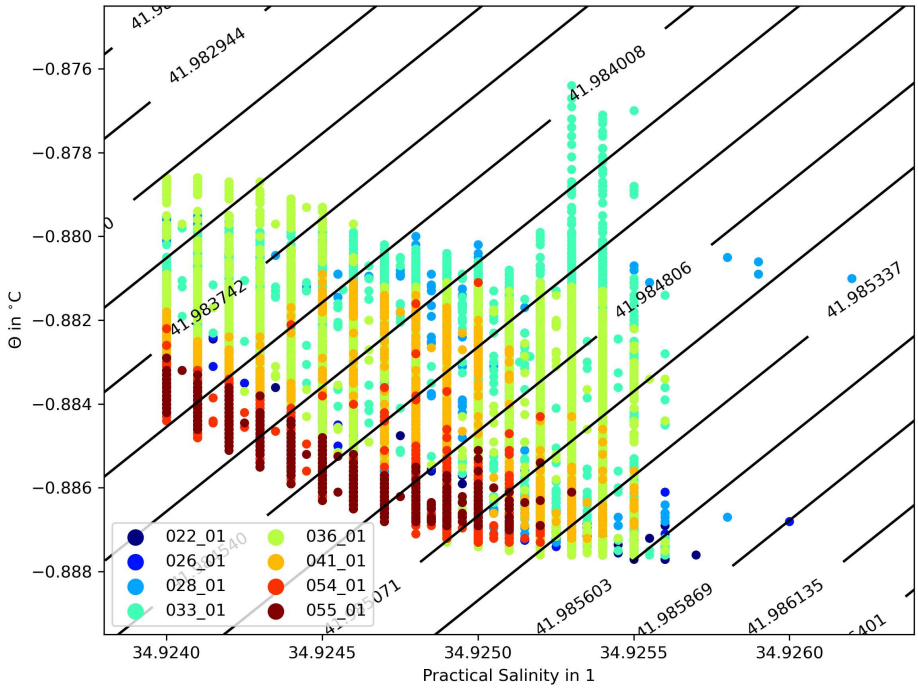

(b)

Figure 5.2.: **(a)** Practical salinity versus potential temperature with lines of equal potential density σ_{3000} below 2500 m for all stations at the vent site with the color indicating the individual stations. The upper right corner shows the CTD tracks of Figure 3.2 for reference.
(b) Close-up of the high σ_{3000} region of Figure 5.2a.

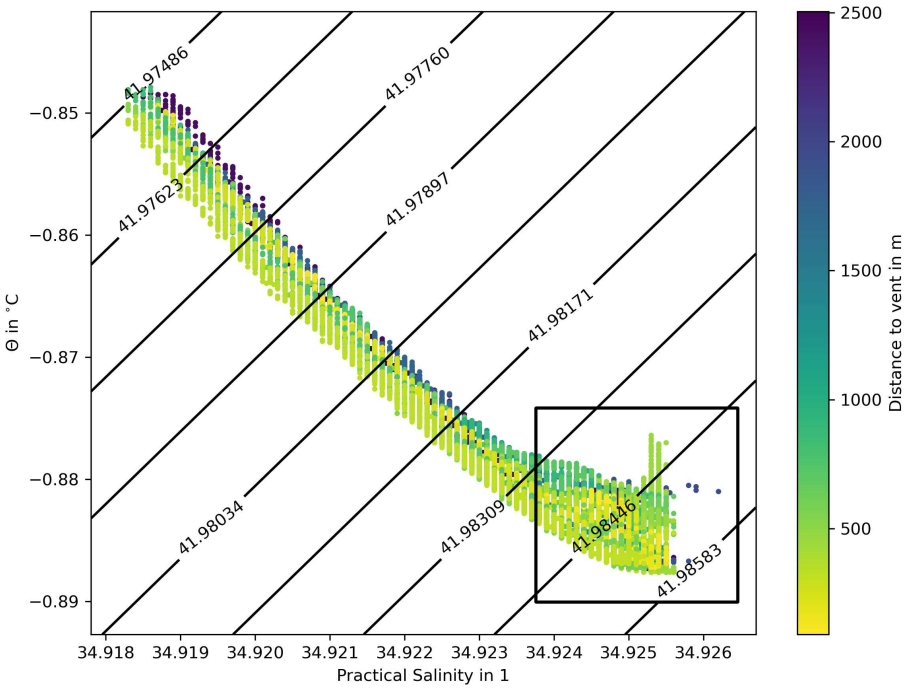

(a)

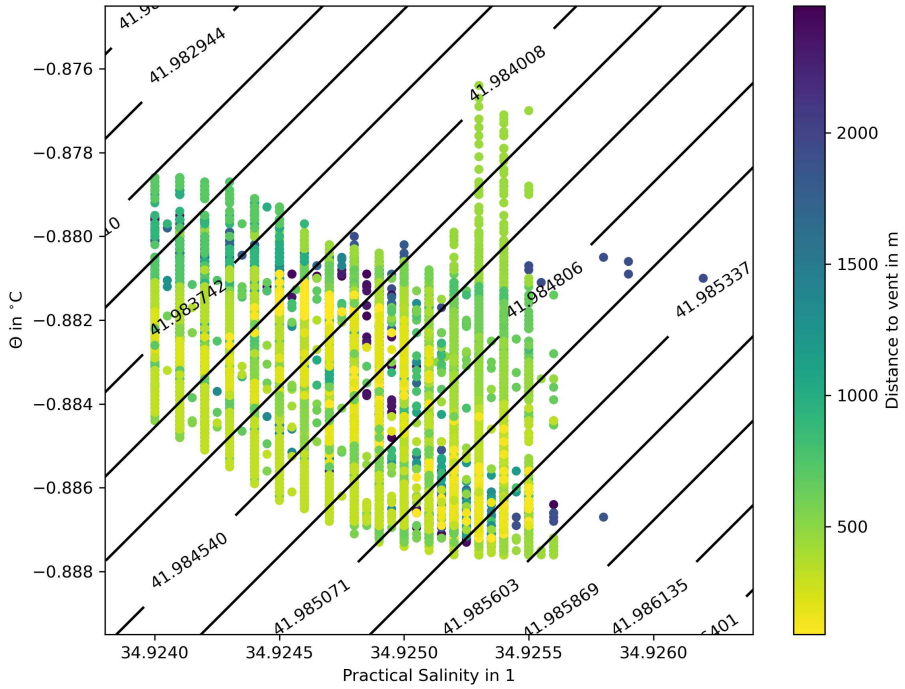

(b)

Figure 5.3.: **(a)** Practical salinity versus potential temperature with lines of equal potential density σ_{3000} below 2500 m for all stations at the vent site, where the color indicates the 3D geometric distance to the vent.
(b) Close-up of the high σ_{3000} region of Figure 5.3a.

5.2. Vertical Extent

To investigate the vertical plume dispersal, the profiles of the plume tracers from the CTD Floe-Yos are analyzed first. The vertical extent or the maximum rise height z_{max} is also important later to estimate the heat flux of the vent system as described in Section 2.2. The focus here is on examining the non-buoyant part of the plume and the usefulness of different plume tracers.

The variation in the tracer quantities between different stations at the Aurora Vent Field, as measured by the CTD sensor package, can be seen in Figure 5.4 as vertical profiles plotted against depth. In the potential temperature (Figure 5.4a) variations are small except between 3000 m to 3700 m where some positive peaks are also visible. Interestingly, there is no warmer bottom layer visible as described in Section 2.1. Variations in σ_{3000} (Figure 5.4b) are also small compared to the overall change with the strongest at approximately ~3000 m and some small peaks around 4000 m. dE_h/dt in Figure 5.4c also shows a strong variation, here between 2800 m to 4000 m with a maximum at ~3300 m. The helium isotope ratio δ^3He, determined from discrete samples and shown in Figure 5.4d, has higher values in a similar range as dE_h/dt with 2700 m to 3300 m and a maximum at approximately 3100 m with over 13 %.

The black lines in each of these plots in Figure 5.4 show the measurements of the background profile *PS137-018-01*. The full background profile is shown in Figure A.3. For θ and σ_{3000} they roughly agree with the other stations, but there are some differences: The background θ curve between 2500 m and 3100 m follows the maximum temperature curves at the vent site, but in deeper layers it follows the minimum curves, with differences of approximately 0.01 °C. A similar but inverted behavior is observed for σ_{3000} where densities are lowest in the background from 2300 m to 3100 m and then higher than the other profiles for depths below 3500 m. The dE_h/dt background profile varies mostly around zero, with noise-like spikes in a range of 0.01 mVs^{-1} and one large symmetric spike at the lowermost measurement. The δ^3He background station features values between 6 % to 8.5 % with a small maximum at 3100 m. The dE_h/dt background behaves similarly at the deepest measurement.

Figure 5.5 shows the same curves for the measurements of the three MAPR instruments mounted on the CTD rosette cable. These contain about three times the amount of profiles as the CTD measurements since for most stations three MAPRs were deployed. The potential temperature profile in Figure 5.5a is very similar to the CTD measurements, with a

similar increase between 3000 m to 3700 m. σ_{3000} (Figure 5.5b) is also similar and follows the background curve even more strictly . For dE_h/dt in Figure 5.5c there is also a similar pattern with a strong decrease between 2900 m to 3700 m. But the profiles and especially the background signal are much more spiky then in the CTD data. The background amplitudes are also larger. Turbidity data (Figure 5.5d) are only available from the MAPR measurements. The data shown here have been smoothed and large outliers have been removed. The signal here follows three different curves with different levels, the background curve follows two different curves. This corresponds to the different instruments used, as most of the stations were conducted with three MAPRs while the background station was conducted with only two. All curves follow a minimal baseline down to approximately 2000 m and then increase to a higher baseline in the range of 2000 m to 4000 m. Centered in this range at 3100 m is a strong peak with up to 0.057 NTU for the MAPRs with the highest level. A similar behavior is visible in the background measurements, but the central peak has a lower amplitude.

From these profiles can be concluded, that dE_h/dt, turbidity and δ^3He give strong hydrothermal plume signals in a similar range, which is not the case for θ and σ_{3000}. The deviations in the first three are clearly distinguishable from the rest of the profile and from the background profile and give a plume signal with a maximum at approximately 3200 m and a minimum plume depth $z_{plume} = \sim$2800 m. Therefore, dE_h/dt can be confidently used as plume tracers and also turbidity and δ^3He with some adjustments, while θ and σ_{3000} need further detailed investigation.

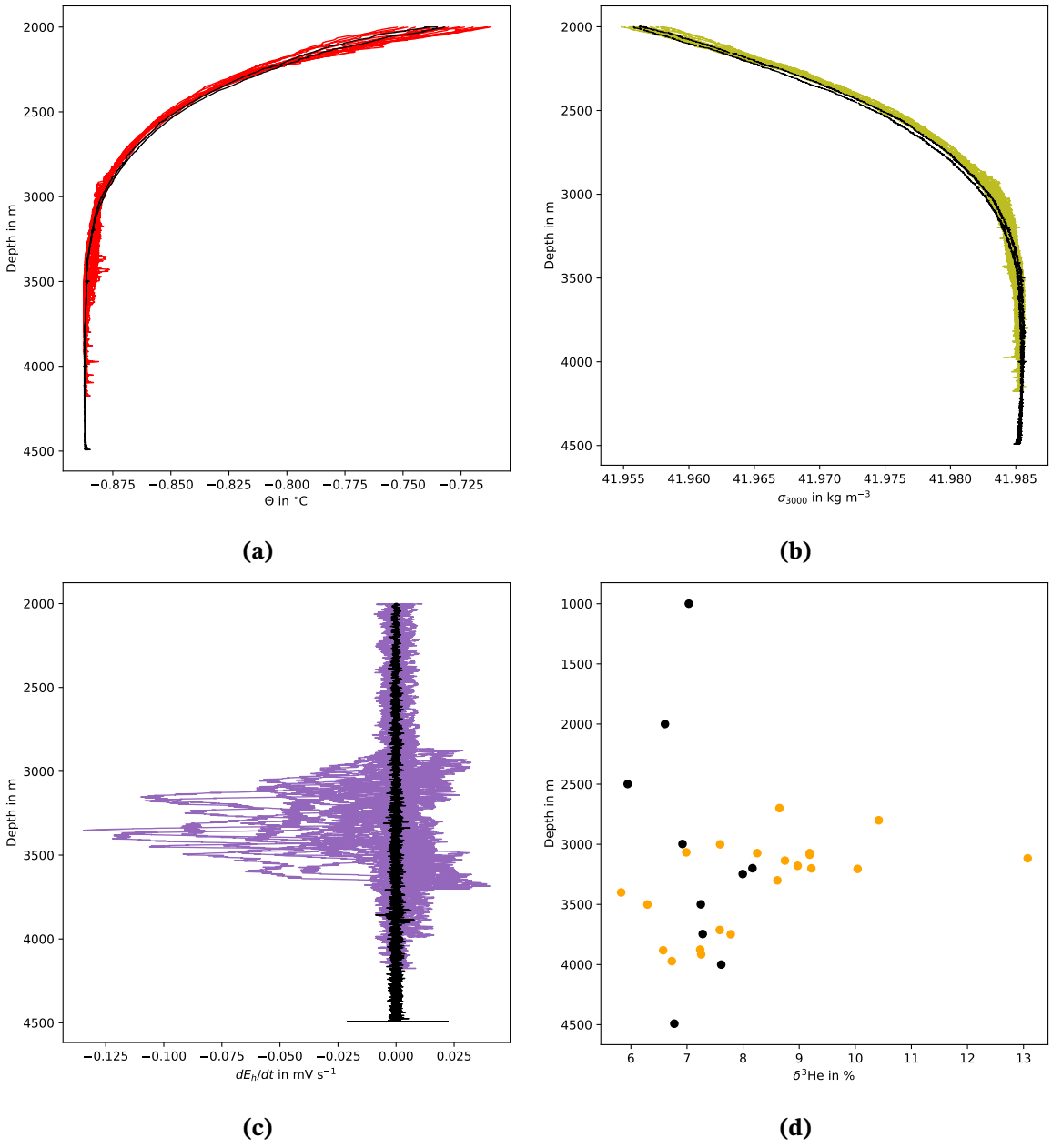

Figure 5.4.: **(a)** Potential temperature θ, **(b)** potential density anomaly σ_{3000}, **(c)** dE_h/dt and **(d)** δ^3He versus depth of the CTD profiles. Measurements below 2000 m (below 1000 m for δ^3He) from all stations at the Aurora Vent Field are superimposed. The black curves show the profiles of the background station *PS137-018-01*.

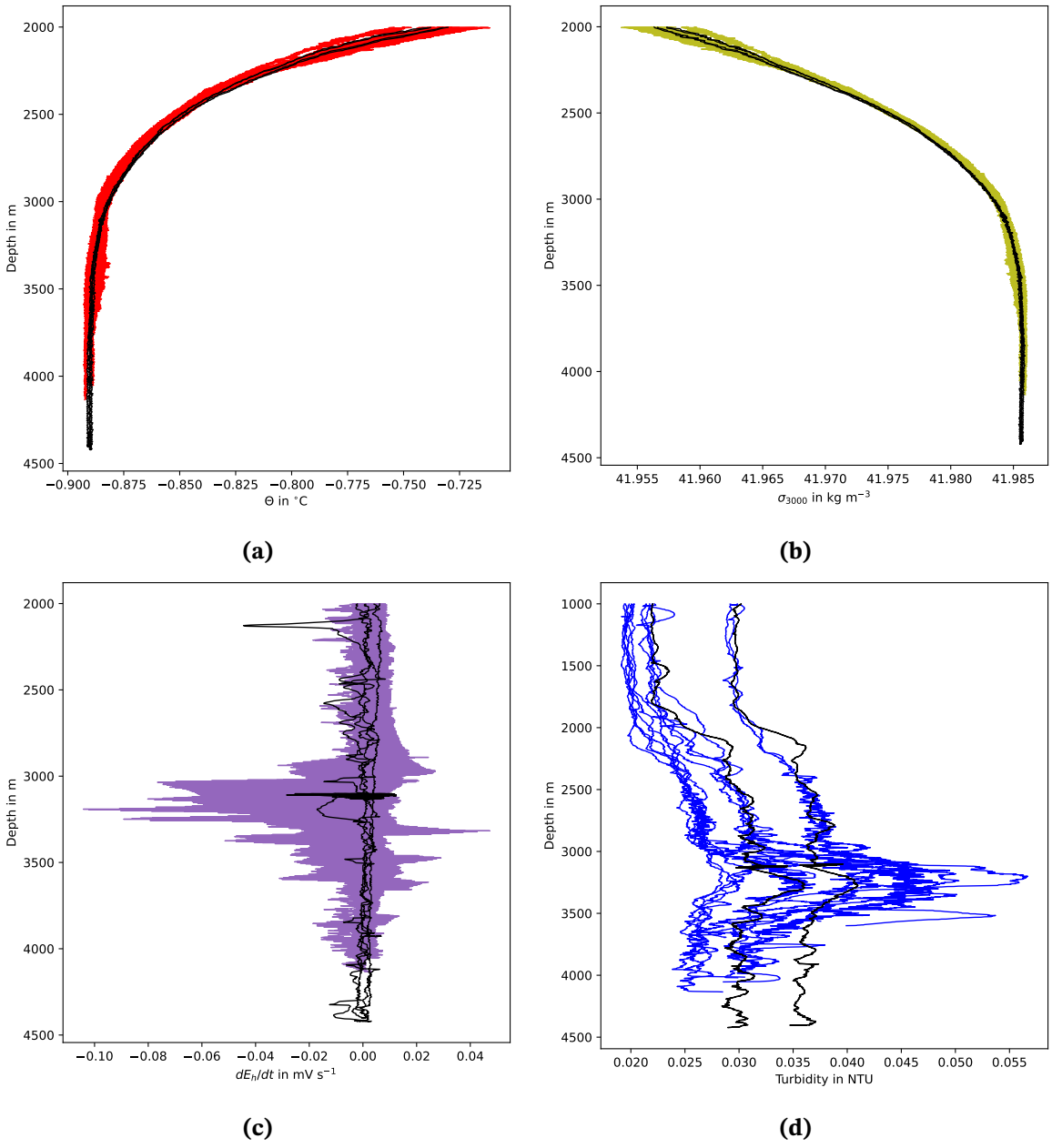

Figure 5.5.: **(a)** Potential temperature θ, **(b)** potential density anomaly σ_{3000}, **(c)** dE_h/dt and **(d)** turbidity versus depth of the MAPRs mounted on the CTD rosette wire. Measurements below 2000 m from all stations at the Aurora Vent Field are superimposed. The black curves show the profiles of the background station *PS137-018-01*.

Plume Anomalies

To asses the deviations of the water column properties attributed to the plume influence, different methods need to be employed for different quantities:

The deviation in potential temperature θ is calculated by fitting a polynomial function to the θ-σ_{3000}-relation, the in-station comparison method, resulting in an anomaly Δ (see Section 3.5). In Figure 5.6 these anomalies are shown for the measurements made by the CTD and by the MAPR. Both show positive anomalies in the plume depth, up to 0.005 °C and peaks up to approximately 0.01 °C. Above the plume depth, anomalies reach a minimum at 2900 m and increase again towards shallower depths. Below the plume depth, the CTD data still feature some profiles with smaller anomalies, the MAPR data decrease subsequently towards the seafloor.

Anomalies in σ_{3000} calculated by the background comparison show only small deviations (see Figure 5.7). They are in the order of $\pm 0.001\,\mathrm{kg/m^3}$ in the expected plume depth. Anomalies are also positive and negative around zero. In principle, density anomalies would only be expected in the buoyant part of the plume and they should also be negative. Therefore σ_{3000} is not considered further in this section regarding the extent of the

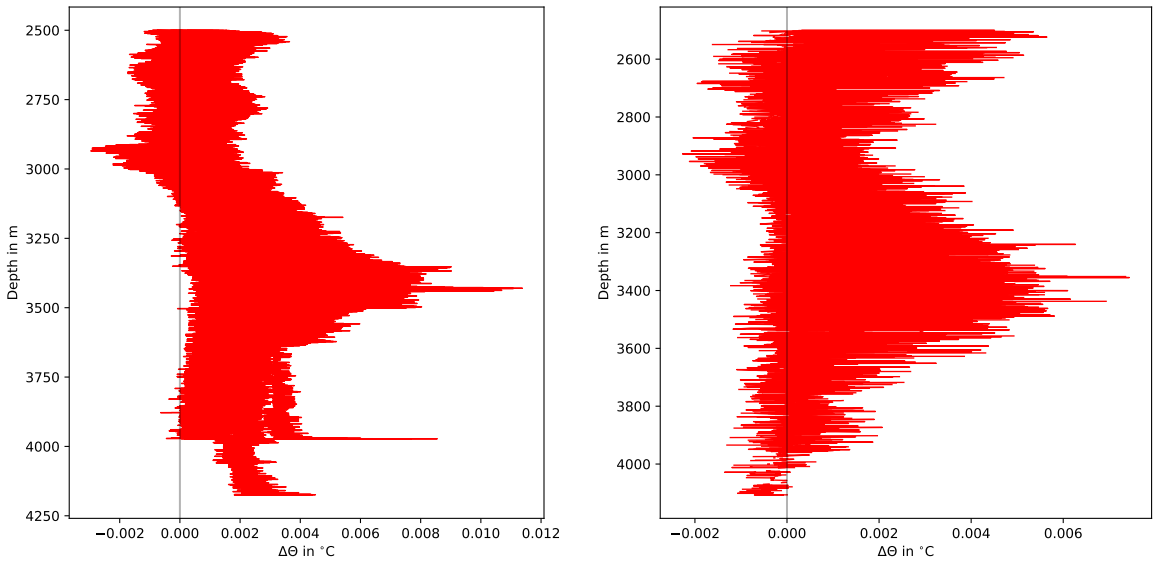

(a) **(b)**

Figure 5.6.: Potential temperature anomaly $\Delta\theta$ measured by **(a)** the CTD and **(b)** the MAPR instruments at the Aurora Vent Field compared to the fit of the background profile. In **(b)** the fit is calculated for the profile of the corresponding instrument taken at the background station. The black line marks the level of zero deviation.

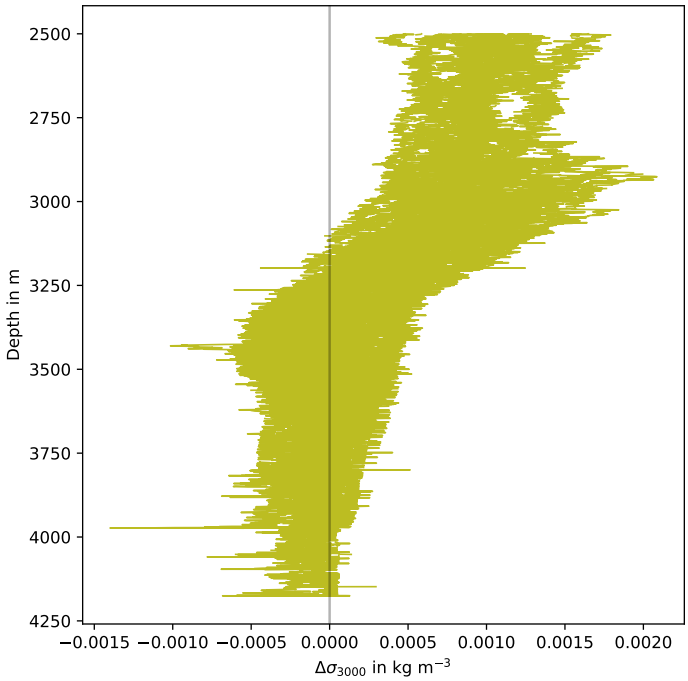

Figure 5.7.: Anomalies in σ_{3000} for all CTD measurements at the Aurora Vent Field compared to the fit of the background profile. The black line marks the level of zero deviation.

non-buoyant plume. σ_{3000} data calculated from the MAPR temperatures is also neglected, as it shows similar results (see Figure A.1). In addition, the MAPRs lack salinity sensors and σ_{3000} is calculated using the salinity measured by the CTD, and is therefore not independent of the CTD measurements.

δ^3He is expected to be mostly constant through the water column, except for the influence explained in Section 2.3. Therefore, only the mean at the background station, excluding surface samples, is subtracted. Tritiogenic components in δ^3He are estimated to be approximately 6 % based on tritium samples taken at the site in 2014 [62]. Figure 5.8 shows δ^3He where a background mean of 7.146 % is subtracted. Due to the increased accumulation of tritiogenic helium since 2014 this background seems reasonable. Most of the Aurora samples show some positive anomalies with approximately 3 % and for one sample 6 % above the background. Samples below the non-buoyant plume depth are close to or even below the background.

Anomalies in turbidity can be seen in Figure 5.9. As one can already suspect from Figure 5.5d, it is necessary to distinguish between the three different instruments when calculating the turbidity anomaly. The direct comparison with the background station is neglected here for the same reason, but is further discussed in Section 6.1. The reference used here

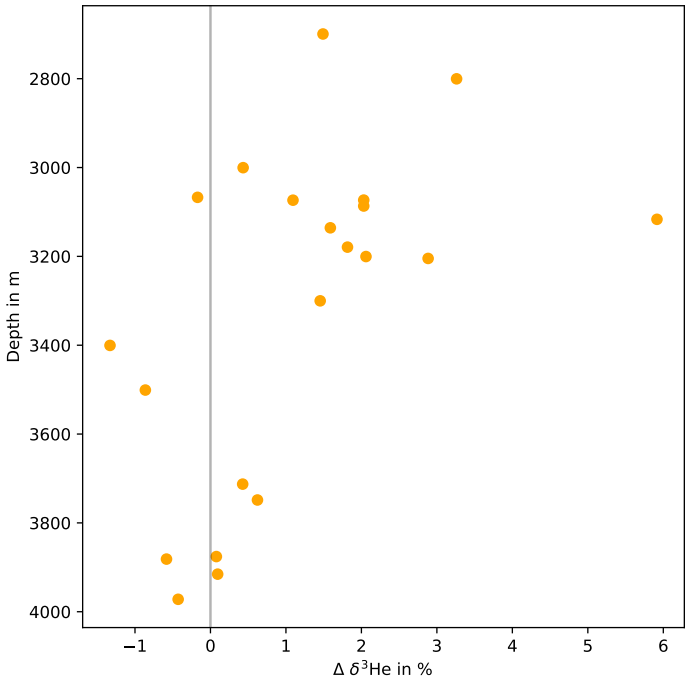

Figure 5.8.: Anomalies in δ^3He for all CTD measurements at the Aurora Vent Field compared to the mean of the background profile. The mean is calculated as 7.146 %. The black line marks the level of zero deviation.

is the deviation from the mean per station and instrument in the layer above and below the expected plume depth (for details see Chapter 3.5). Positive anomalies in turbidity are visible between 2200 m and 4000 m for some measurements. The central peak from before is limited to 3000 m to 3500 m. Most of the profiles have peaks of up to approximately 0.015 ΔNTU and one up to 0.03 ΔNTU.

Plume Simulation

The results of the ROMS simulation in Figure 5.10 show the daily averaged tracer concentration at the location of the simulated vent. Above 2600 m depth the concentration is zero but below this depth maxima at 3500 m can be observed for the first six days of the simulation period. This would correspond to a minimum plume depth z_{plume} of approximately 2600 m with a non-buoyant plume forming below. The curve formed by this tracer maximum extends from 2500 m to the seafloor while decreasing. For the subsequent days the concentration is always zero above 3700 m from where it increases sharply towards the seafloor with the overall highest values. A similar behavior is shown in Figure 5.11,

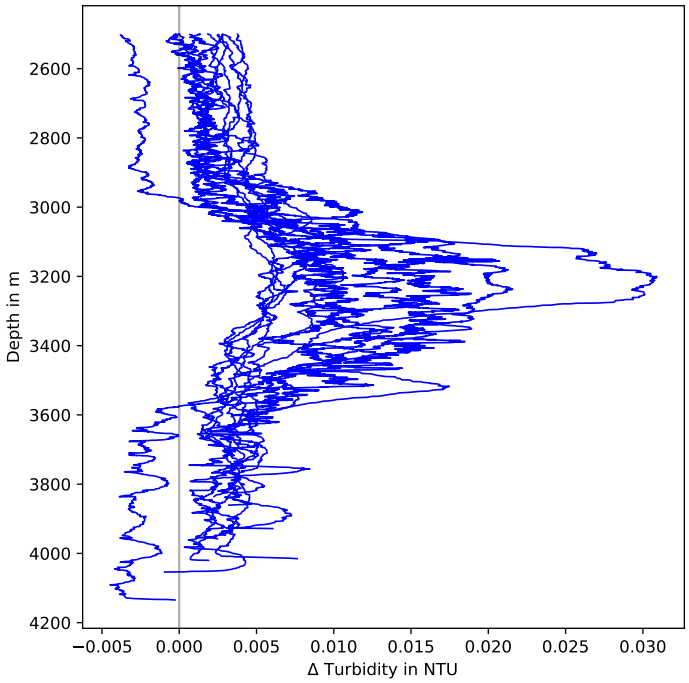

Figure 5.9.: Anomalies in turbidity for all MAPR measurements at the Aurora Vent Field compared to the mean above and below the plume depth per station and instrument. The black line marks the level of zero deviation.

where the concentration change over time is more clearly visible. It is particularly interesting that the tracer layer is more clearly pronounced four days after the start, rather than right at the beginning. There it also reaches a larger vertical extent. After the first of August the accumulation of the tracer at the bottom starts and becomes weaker with time except for two small peaks close to the end of the simulation period.

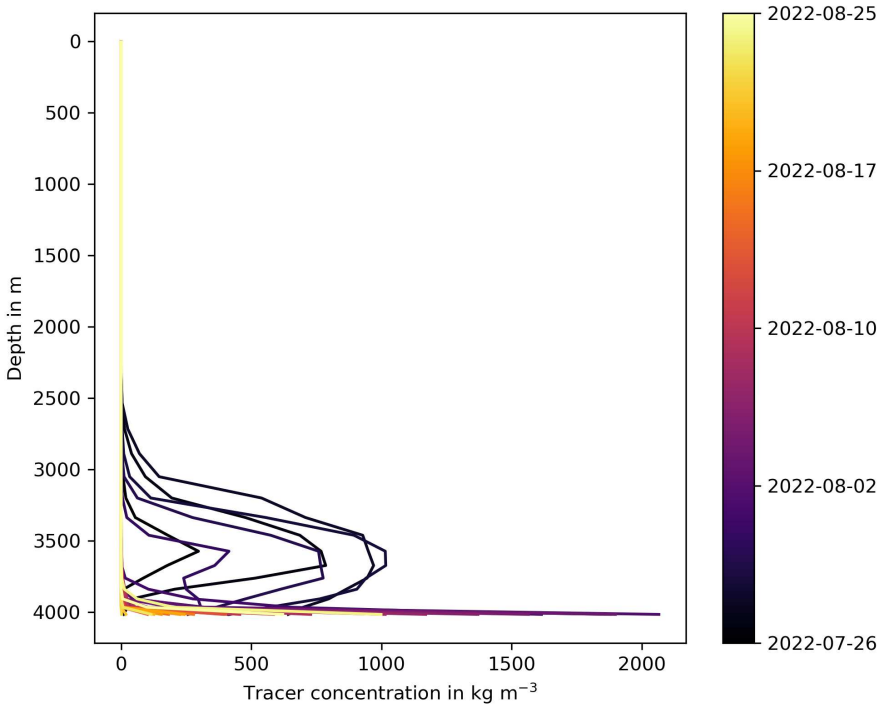

Figure 5.10.: Tracer concentration from the ROMS simulation at the location of the simulated vent versus depth. Each line represents a daily average, with the darkest lines at the beginning and the lightest at the end of the simulation period.

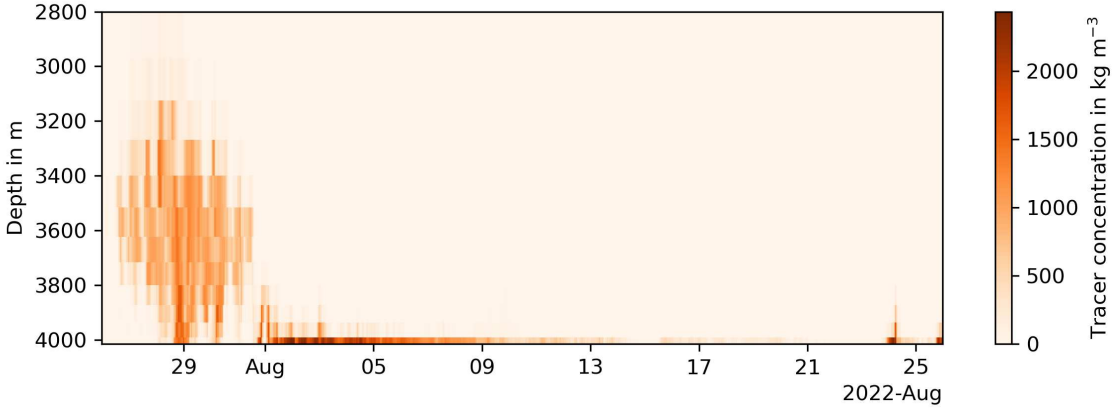

Figure 5.11.: Tracer concentration below 2800 m averaged per hour from the ROMS simulation at the location of the simulated vent versus depth and time during the 31 day simulation period.

5.3. Heat Flux Estimate

The maximum rise height z_{max} of the plume can be inferred from the minimum depth z_{plume} at which an anomaly is observed in the examined quantity. This minimum is chosen based on the anomalies presented in the section above in a way that it is marked by the depth, where an increase towards a maximum in the plume depth is visually recognizable in the envelope of all stations. It is then rounded to 100 m. N^2 is calculated with the term $\frac{dp(z)}{dz}$ as the density gradient between the vent depth and z_{plume} with the values from a nearby CTD profile, station *PS137-055-01*. The heat flux can then be estimated according to Chapter 2.2. In general, for a given stratification, a larger rise height will result in a larger heat flux, because more energy is required to make the fluid ascend. This is reflected in the results in Table 5.1 with the heat flux rounded to 10^6 Watt. One can also see, that z_{max} and thus the heat flux varies strongly within a range of 330 m or 330 MW respectively, depending on the quantity.

	θ_{CTD}	dE_h/dt_{CTD}	δ^3He	θ_{MAPR}	dE_h/dt_{MAPR}	Turbidity$_{MAPR}$
z_{plume} in m	2900	2800	2700	2900	2900	3000
z_{max} in m	1000	1100	1200	1000	1000	900
N^2 in $s^{-2} \times 10^{-8}$	3.09	4.01	5.06	3.09	3.09	2.47
Heat flux in MW	83	181	363	83	83	39

Table 5.1.: Minimum plume depth z_{plume}, maximum rise height z_{max}, buoyancy frequency N^2 and estimated heat flux of the plume inferred from the highest anomaly of the different quantities. N^2 is calculated from a nearby CTD profile, station *PS137-055-01*. The constants used are listed in Table A.3.

5.4. Horizontal Extent

The horizontal distribution of the quantities varies, also with respect to the instrument used. Figure 5.12 shows the distribution for $\Delta\theta$ and dE_h/dt measured by the CTD and δ^3He samples. For all three, the strongest plume influence is concentrated near the vent site, for $\Delta\theta$ and dE_h/dt to the northwest, but also with maxima at different locations. The δ^3He maximum instead is located southeast of the vent but even closer. The westernmost station *PS137-028-01* shows only weak signals in $\Delta\theta$ and dE_h/dt, while no δ^3He samples were taken there.

A similar distribution is visible in the MAPR results in Figure 5.13 for $\Delta\theta$ and dE_h/dt, although the anomalies are smaller, especially for $\Delta\theta$. But again the maxima are located close northwest of the vent, while measurements further away show only small anomalies. Turbidity values show two points with the strongest anomalies in the southeast very close to the vent, similar to δ^3He. To the northwest turbidity anomalies are not particularly strong and are also irregular. Notably station *PS137-028-01* to the west features also high values but with very little variation between it's data points. from the highest anomaly of the different quantities.

The relationship between anomaly strength and distance from the vent site is displayed in Figures 5.14 for the CTD measurements and 5.15 for the MAPR measurements. For the former, all three tracers show strong peaks between 300 m to 750 m while very close to the vent only δ^3He shows strong anomalies in two samples. At 850 m there is another strong peak in $\Delta\theta$ and dE_H/dt but from 750 m to 1800 m the $\Delta\theta$ anomalies are weaker except for occasional peaks and dE_H/dt is close to zero. Further out than 1800 m there are still oscillating anomalies in $\Delta\theta$ but at a lower level. In the close-up of the first 800 m in Figure 5.14b it is particularly visible, that the anomalies very close to the vent site, up to 250 m, are quite low, except for the few δ^3He samples.

The anomalies in $\Delta\theta$ of the MAPR data in Figure 5.15 are similar as in the CTD data. For the part closest to the vent site, also shown as a close-up in Figure 5.15b, anomalies are small but there are strong peaks between 300 m to 900 m. For larger distances the overall level decreases slightly with occasional peaks. Between 1900 m to 2300 m there is a section with almost constant anomalies but also with two different levels. The turbidity anomaly follows a very similar pattern as $\Delta\theta$, except that very close to the vent there are two very strong peaks, which are also the strongest overall. In addition, during the section of constant $\Delta\theta$ between 1900 m to 2300 m the turbidity anomaly is also constant and very high. This is the section that was excluded in the CTD data and will be discussed later in Chapter 6.1. dE_H/dt also features some stronger peaks in the 300 m to 900 m range but then decays to zero for larger distances and is similar to the CTD data, but with generally a low amplitude. There are also no notable peaks in the constant region.

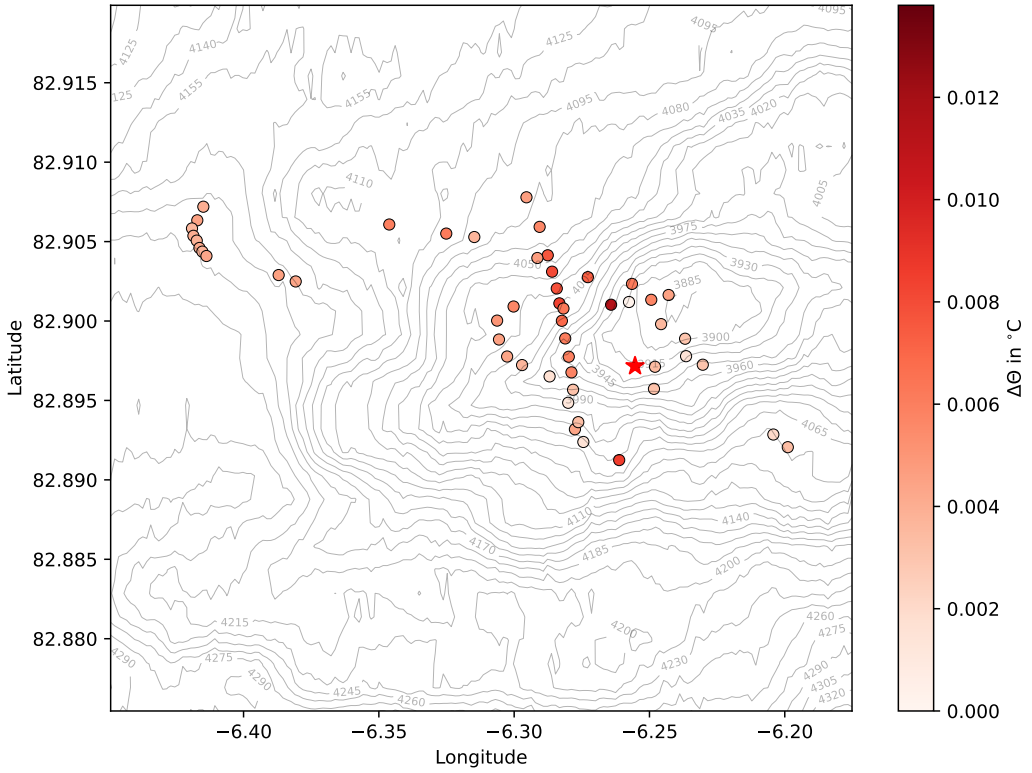
Latitude
Longitude
82.915
82.910
82.905
82.900
82.895
82.890
82.885
82.880
−6.40
−6.35
−6.30
−6.25
−6.20
0.012
0.010
0.008
0.006
0.004
0.002
0.000
ΔΘ in °C

(a)

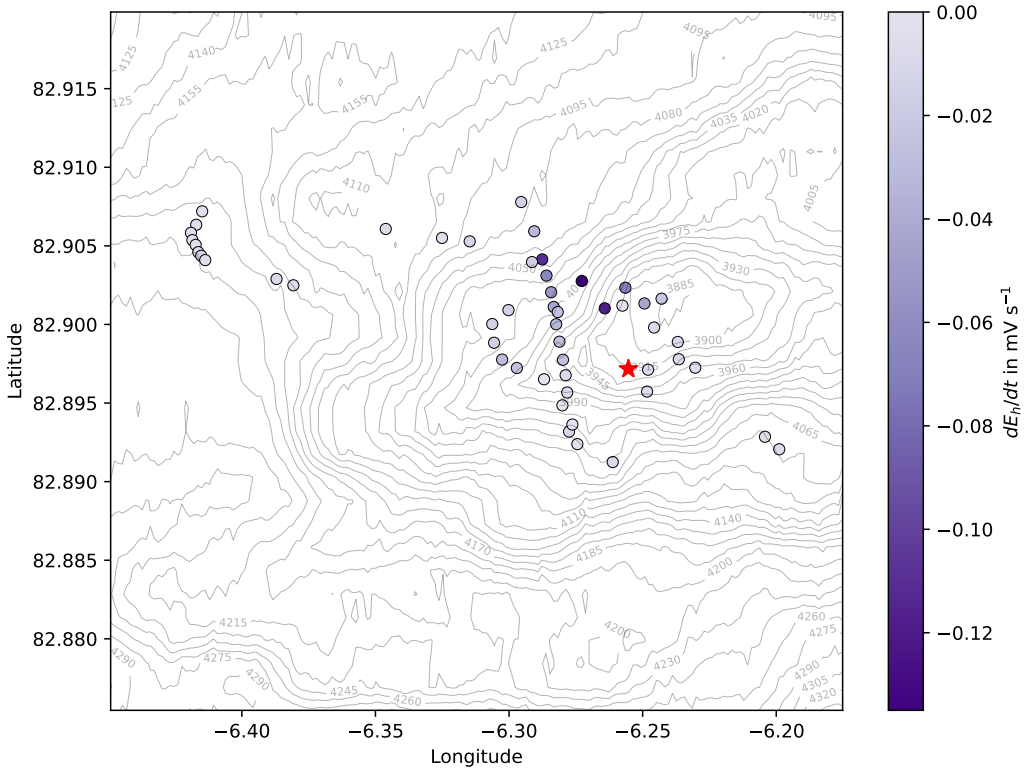
Latitude
Longitude
82.915
82.910
82.905
82.900
82.895
82.890
82.885
82.880
−6.40
−6.35
−6.30
−6.25
−6.20
0.00
−0.02
−0.04
−0.06
−0.08
−0.10
−0.12
dE_h/dt in mV s^{-1}

(b)

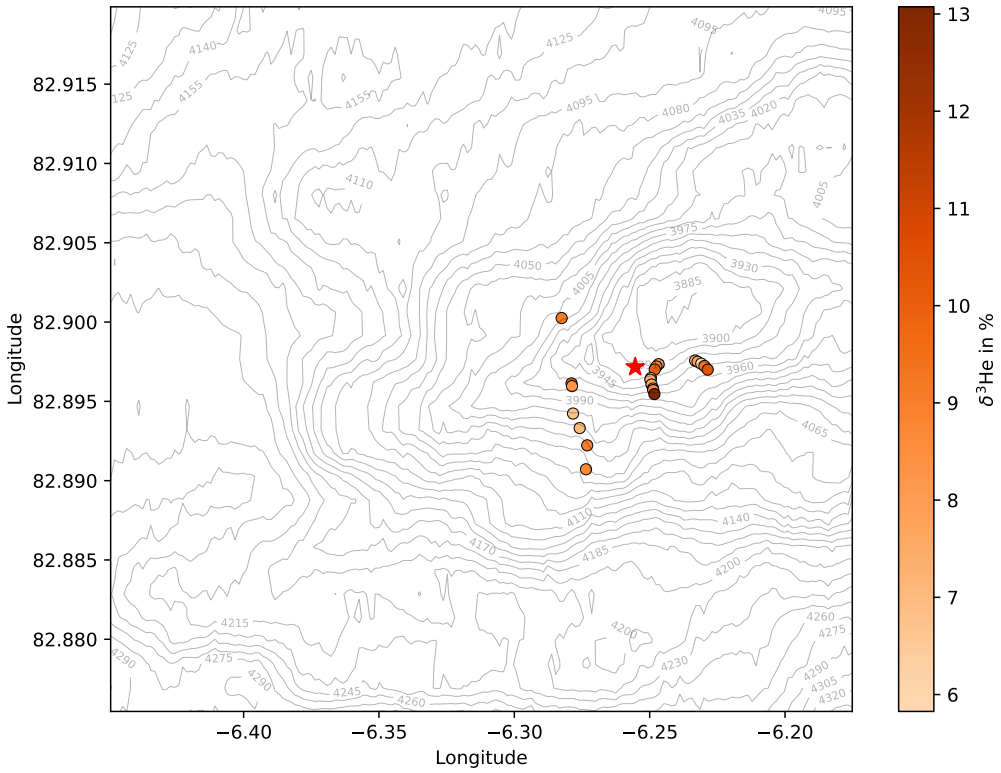

(c)

Figure 5.12.: (a) Potential temperature anomaly $\Delta\theta$, **(b)** dE_H/dt and **(c)** δ^3He of the CTD measurements in relation to position and bathymetry. Temperature anomalies are calculated using the in-station comparison method. Each circle shows the maximum anomaly value per upcast or downcast below 2000 m depth. The color grading is chosen so, that darker colors indicate a stronger influence of the plume fluid. The location of the vent field is marked by the red star.

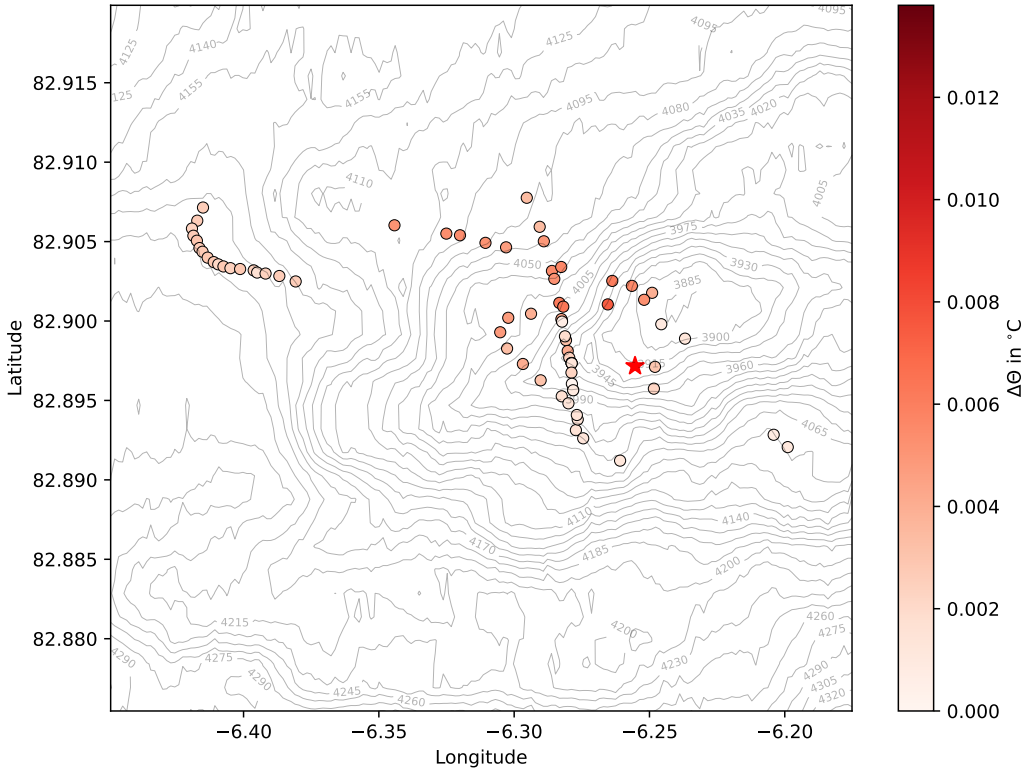
Latitude
Longitude
82.915
82.910
82.905
82.900
82.895
82.890
82.885
82.880
−6.40
−6.35
−6.30
−6.25
−6.20
0.012
0.010
0.008
0.006
0.004
0.002
0.000
ΔΘ in °C

(a)

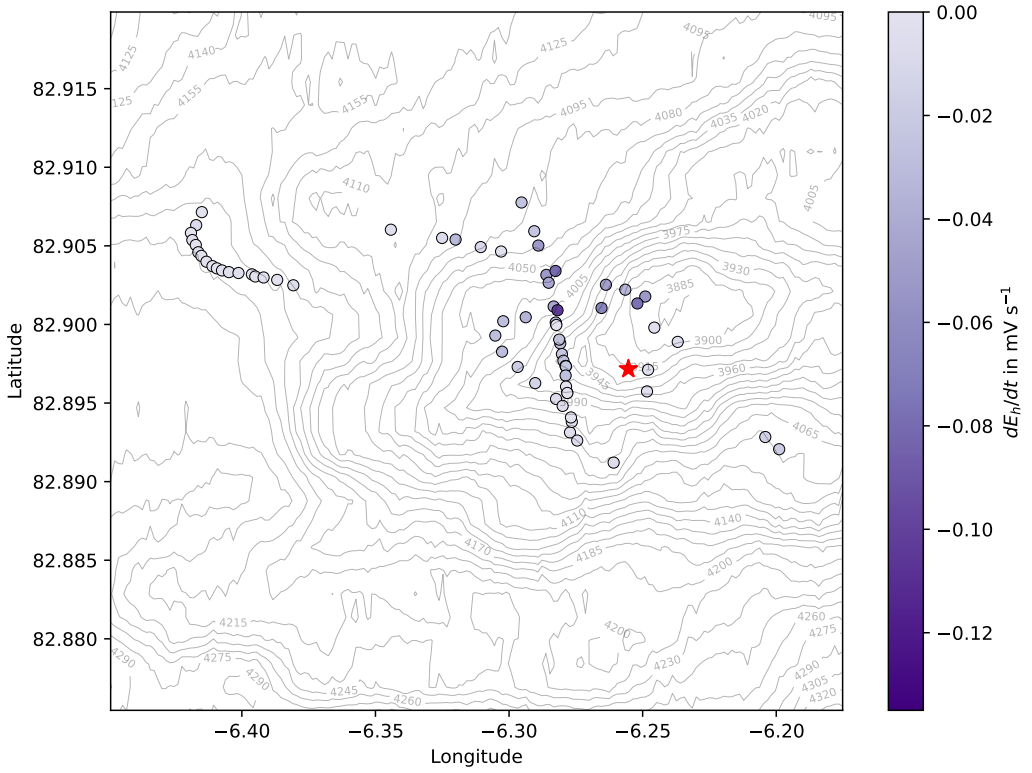
Latitude
Longitude
82.915
82.910
82.905
82.900
82.895
82.890
82.885
82.880
−6.40
−6.35
−6.30
−6.25
−6.20
0.00
−0.02
−0.04
−0.06
−0.08
−0.10
−0.12
dE_h/dt in mV s^{-1}

(b)

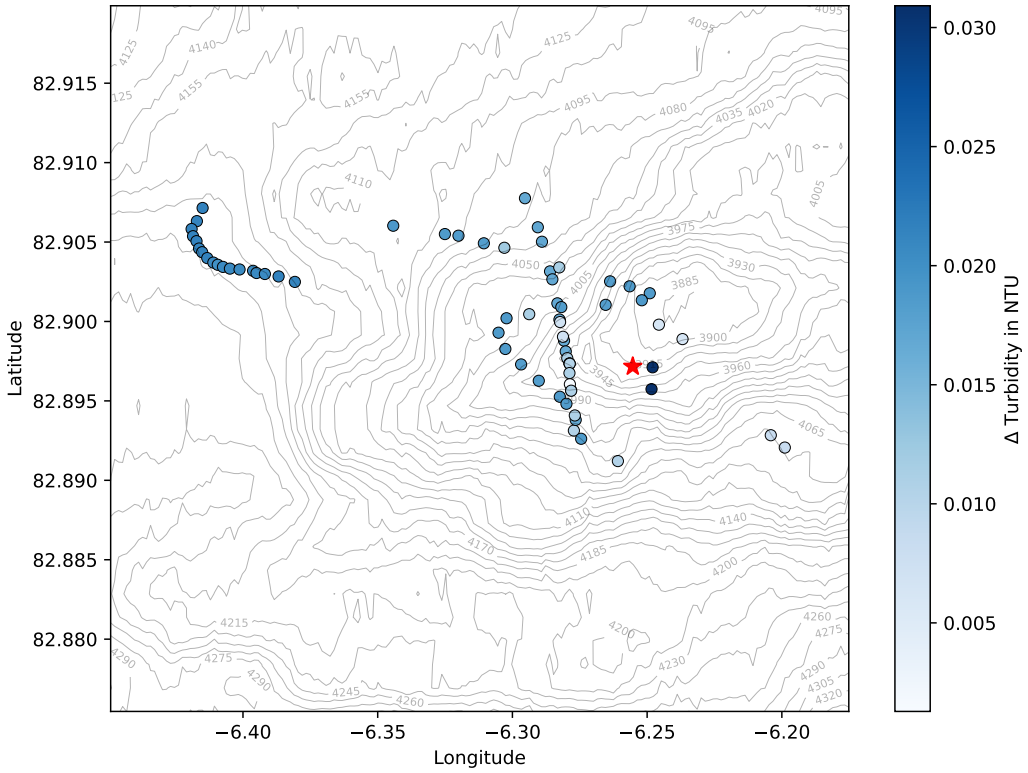

(c)

Figure 5.13.: **(a)** Potential temperature anomaly $\Delta\theta$, **(b)** dE_H/dt and **(c)** δ^3He of the MAPR measurements in relation to position and bathymetry. Temperature anomalies are calculated using the in-station comparison method. Each circle shows the maximum anomaly value per upcast or downcast below 2000 m depth. The color grading is chosen so, that darker colors indicate a stronger influence of the plume fluid. The location of the vent field is marked by the red star.

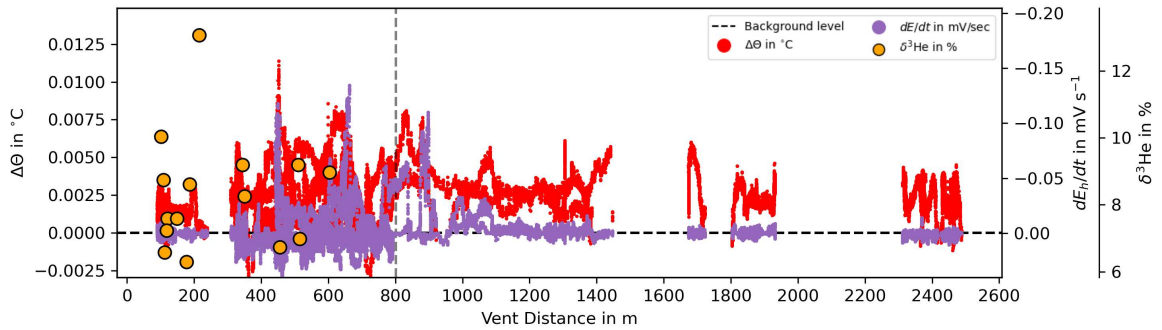

(a)

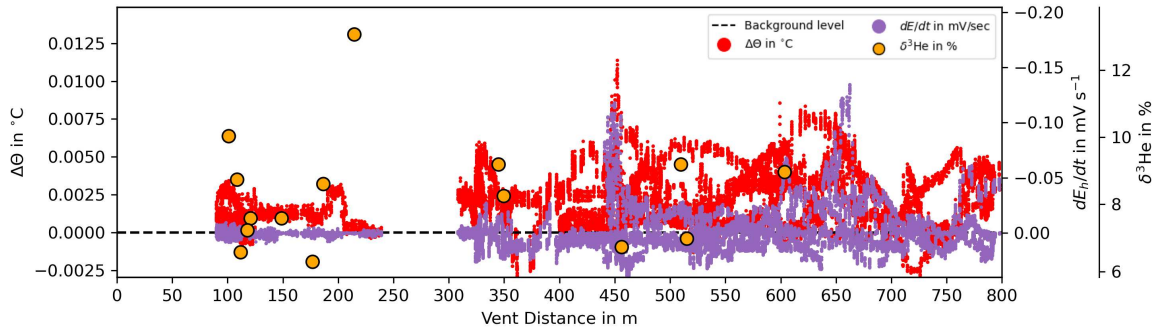

(b)

Figure 5.14.: **(a)** Potential temperature anomaly $\Delta\theta$, dE_H/dt and δ^3He of the CTD measurements versus geodesic distance from the vent position for measurements below 2900 m. The dashed black line marks the level assumed as the background.
(b) Close-up of 5.14a up to the dashed line marking the 800 m distance to the vent site.

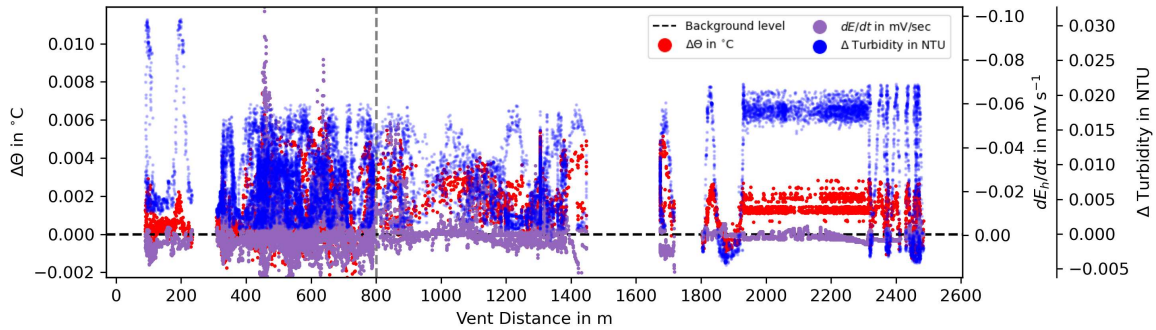

(a)

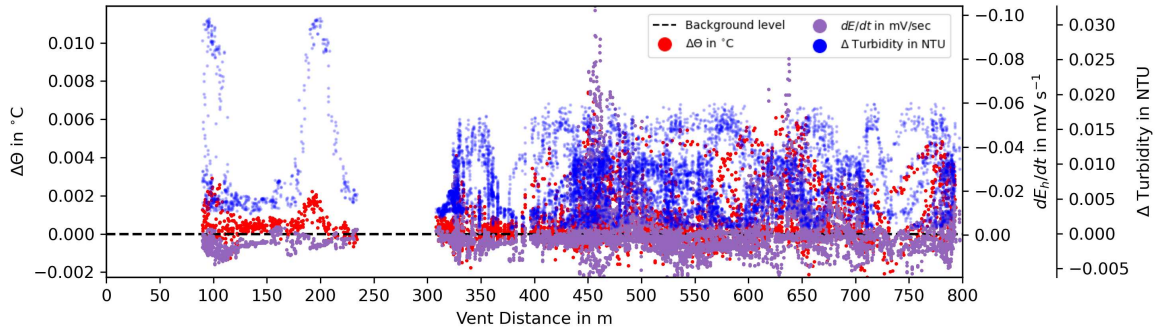

(b)

Figure 5.15.: **(a)** Potential temperature anomaly $\Delta\theta$, dE_H/dt and δ^3He of the MAPR measurements versus geodesic distance from the vent position for measurements below 2900 m. The dashed black line marks the level assumed as the background.
(b) Close-up of 5.15a up to the dashed line marking the 800 m distance to the vent site.

Plume Simulation

The horizontal dispersion of the tracer in the ROMS simulation over time is shown in Figure 5.16. To evaluate all tracer occurrences in a potential plume layer the tracer concentration is summed up between 2500 m and 3900 m. The figures 5.16a to 5.16e show the initial entrainment and subsequent dispersion of the tracer during the first 10 days of the simulation. The main propagation direction is to the north with a small westward component in Figure 5.16e. The tracer accumulation mostly propagates in one cluster and does not disperse strongly before radiating out of the domain at the northern boundary. This is even more the case for the box defined by the gray crosses, which corresponds to the observed area in the section above in Figure 5.12). In this area the tracer accumulation is even more concentrated. Representative for the rest of the simulation time (not shown here), Figure 5.16f shows the last day where almost no tracers are present. Only very low concentrations relative to the initial entrainment are visible, but now to the east of the simulated vent location. The direction of the plume dispersal shown here differs strongly from the direction observed in the data, which appeared to be westward if at all.

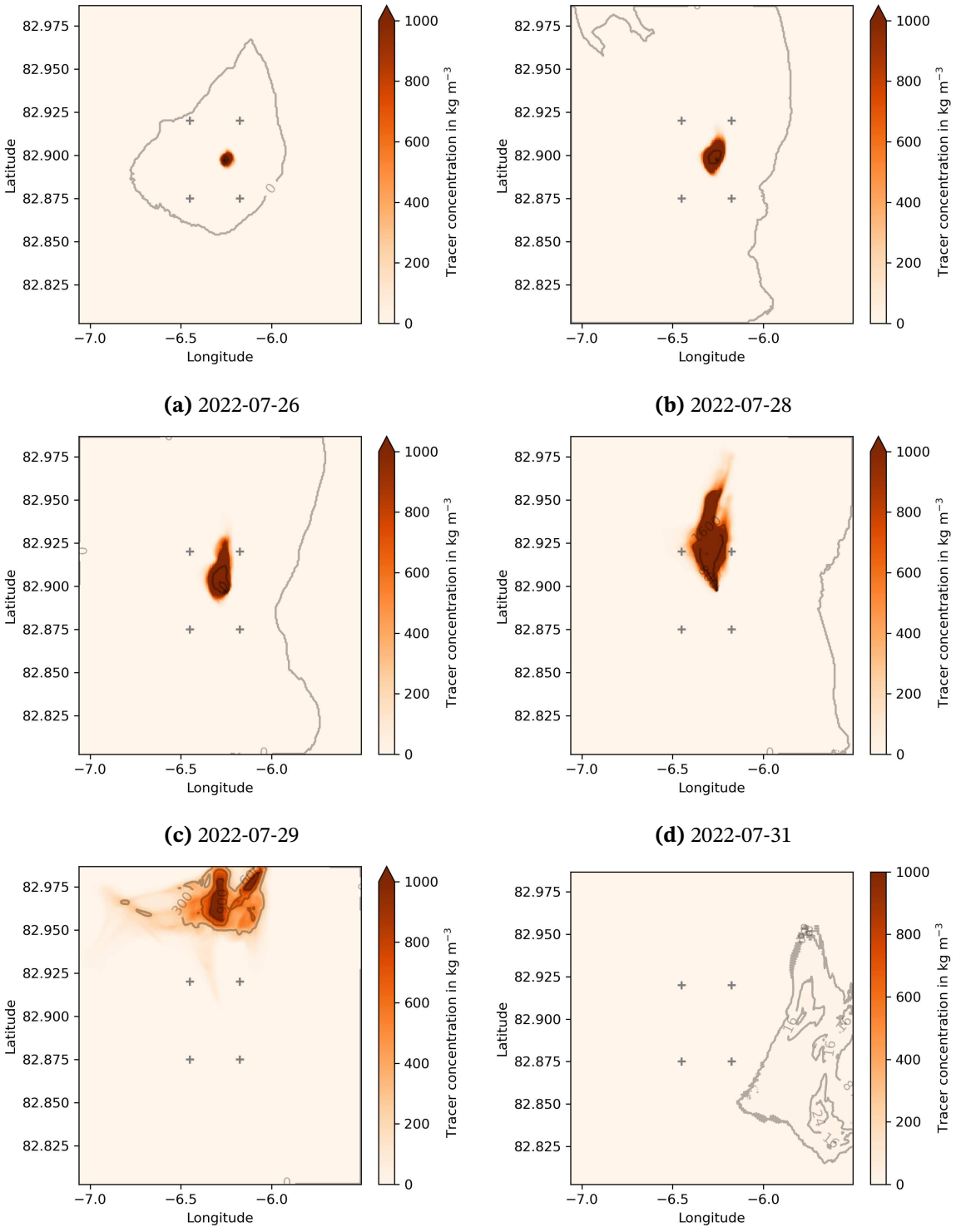

(a) 2022-07-26

(b) 2022-07-28

(c) 2022-07-29

(d) 2022-07-31

(e) 2022-08-02

(f) 2022-08-25

Figure 5.16.: Daily averaged tracer concentration summed up over the plume layer (2500 m to 3900 m) for different days of the simulation period. The four gray crosses mark the area displayed in Figure 5.12, were observational data were collected. Note that the shown time steps are not equidistant.

5.5. Current Measurements

Current velocities at the Aurora Vent Site were measured by two separate strategies: The Aquadopp acoustic current meter mounted on the CTD rosette was used at one station where the CTD rosette was stationary in the vertical. The four RCM11 acoustic current meters in the AURORA 1 mooring observed currents for a long-term time series of one year at four different depth levels in the expected plume layer.

Aquadopp

The Aquadopp time series in Figure 5.17 shows only negative u and positive v values over the measurement duration of approximately 2 h and 20 min. Around 02:00 there is a maximum visible in the v-component and less variation in the u-component, otherwise both signals vary only between $-2.5\,\mathrm{cms}^{-1}$ to $-9\,\mathrm{cms}^{-1}$ for u and $2.7\,\mathrm{cms}^{-1}$ to $12.2\,\mathrm{cms}^{-1}$ for v. The mean u- and v components are $-4.5\,\mathrm{cms}^{-1}$ and $2.6\,\mathrm{cms}^{-1}$, respectively, resulting in a northwestward mean flow. Compared to the mean velocities measured at the mooring over a full year, the short-term mean flow measured by the Aquadopp is more northerly and several times larger (see Table 5.2).

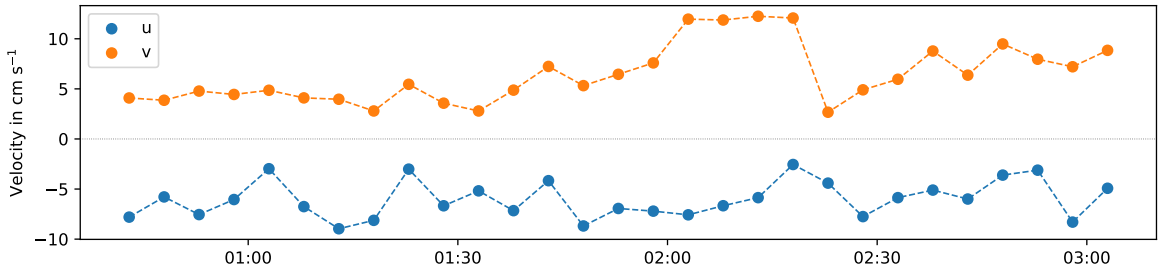

Figure 5.17.: Time series of u- and v components of the stationary Aquadopp measurement at station *PS137-028-01*.

	RCM512	RCM506	Aquadopp	RCM569	RCM474
Depth in m	3064	3215	3220	3366	3572
u-mean in cms^{-1}	-1.2	-1.3	-4.5	-1.2	-0.2
v-mean in cms^{-1}	-0.5	0.3	2.6	-0.4	0.1

Table 5.2.: Mean u- and v components for each current meter of the mooring AURORA 1.

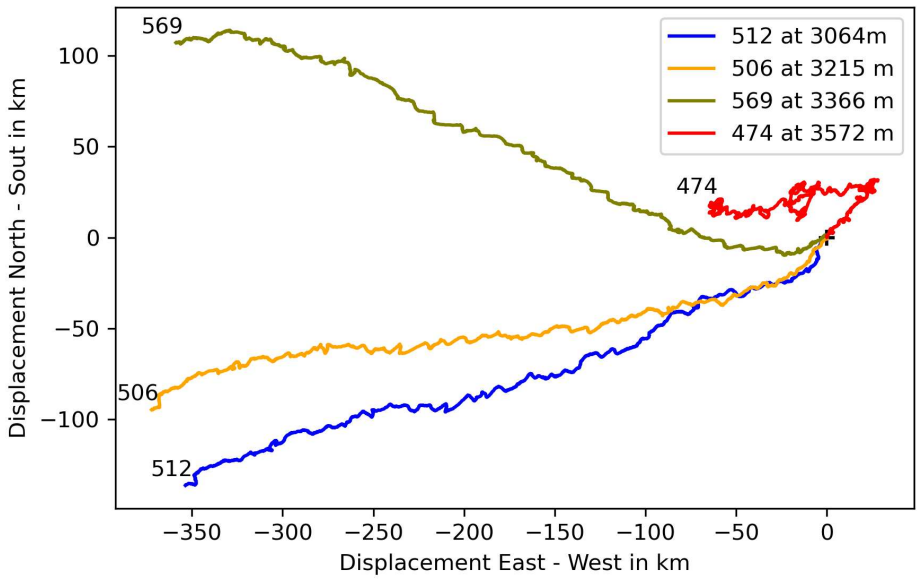

Figure 5.18.: Progressive vector diagram of the four different current meters in the Aurora 1 mooring for one year of observations. The black cross marks the point of zero displacement.

Mooring

The current velocities of the mooring show a different behavior at the different depths, as can be seen in Figure 5.18. It shows the displacement a particle would experience if it were affected by the measured velocities for the one year of measurement. The data from the bottommost instrument 474 differs significantly from the other three. Here the displacement is first oriented to the northeast and then varies in an east-west direction. The flow at the next current meter 569 is directed towards the northwest while the two topmost (506 and 512) show a displacement towards the southwest, but of a similar magnitude. Especially when considering the three uppermost current meters, the mean flow is orientated towards the west, as shown in Table 5.2.

If one examines the time series shown in Figure 5.19, a notable feature is the low amplitude. The maximum varies between 0 cms^{-1} and 6 cms^{-1} depending on the instrument. The mean flow directions from Figure 5.18 are also visible: For 512, 506 and 569 the u component is almost completely negative resulting in the westward flow while the mean v component is closer to zero. The data from the 474 current meter is closer to zero except for a few peaks. While the data has a high variability in general, the amplitude of the peaks increases during Arctic winter for all four instruments.

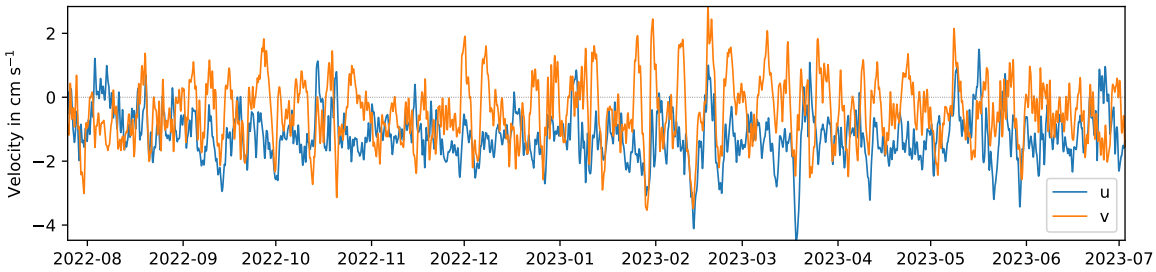

(a) 512 at 3064 m

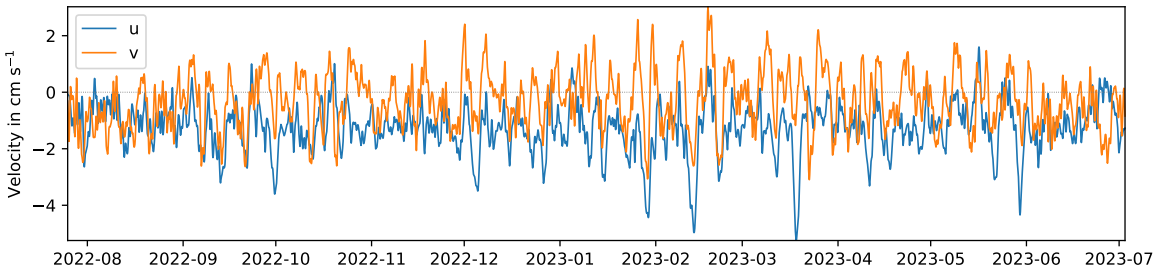

(b) 506 at 3215 m

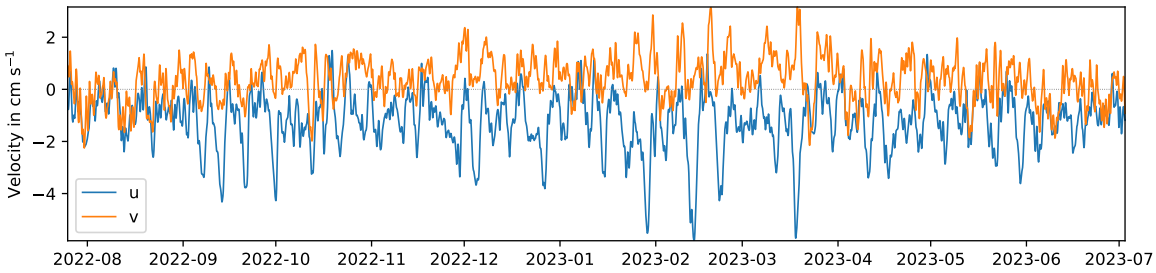

(c) 569 at 3366 m

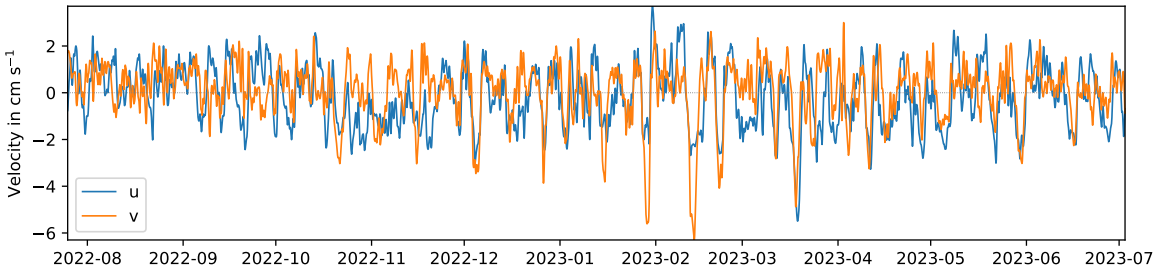

(d) 474 at 3572 m

Figure 5.19.: Time series of the u and v components of the four different RCM11 current meters in the Aurora 1 mooring. The data are filtered with a 24-point Hanning window.

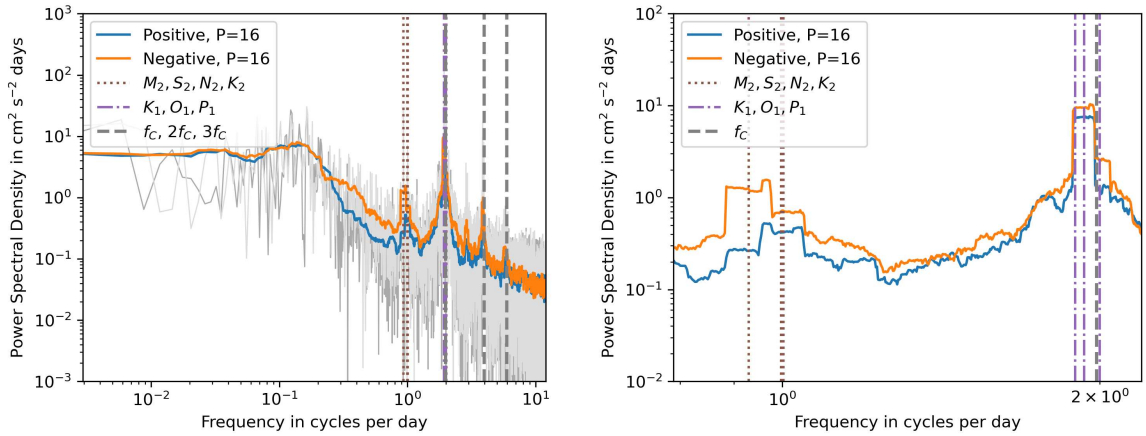

(a) **(b)**

Figure 5.20.: Spectral estimates of the positive (blue) and negative (orange) rotating components of the most lowest current meter 474 for **(a)** the full frequency range and **(b)** a close-up of the peaks at 1 and 2 cycles per day. It is filtered using the multitaper method with $P = 16$, while the gray background represents the unfiltered components. Seven tidal frequencies are marked by the dotted and dashed-dotted lines and the Coriolis frequency f_C as well as its multiples by the dashed lines. Tidal frequencies are based on [28].

The spectral estimates of the current data displayed in Figure 5.20 reveal distinctive peaks in the filtered signal in both the positive and negative rotating components. These peaks align with characteristic frequencies: The first peak is located close to the diurnal tidal frequencies of K_1, O_1 and P_1. From approximately 0.2 cycles per day up to this peak the positive rotating component has a higher amplitude than the negative rotating component while they level again afterwards. The second peak, which is also the strongest, corresponds to the Coriolis frequency f_c and the semi-diurnal tidal frequencies of K_1, M_2, S_2, N_2 and K_2. With increasing frequency, it is followed by a very small peak independent of tidal or Coriolis frequencies and two other peaks with a decreasing amplitude at $1f_C$ and $2f_C$ respectively. The same peaks appear in the measurements of the other current meters with only some differences in amplitude, as shown in Figure A.2.

Plume Simulation

The currents in the ROMS simulation are analyzed at the location corresponding to the mooring and at the depth levels corresponding to the four acoustic current meters as described above. Figure 5.21 shows this data as a progressive vector diagram similar to Figure 5.18 but now only for the simulation period of 31 days. All depth levels feature a strong

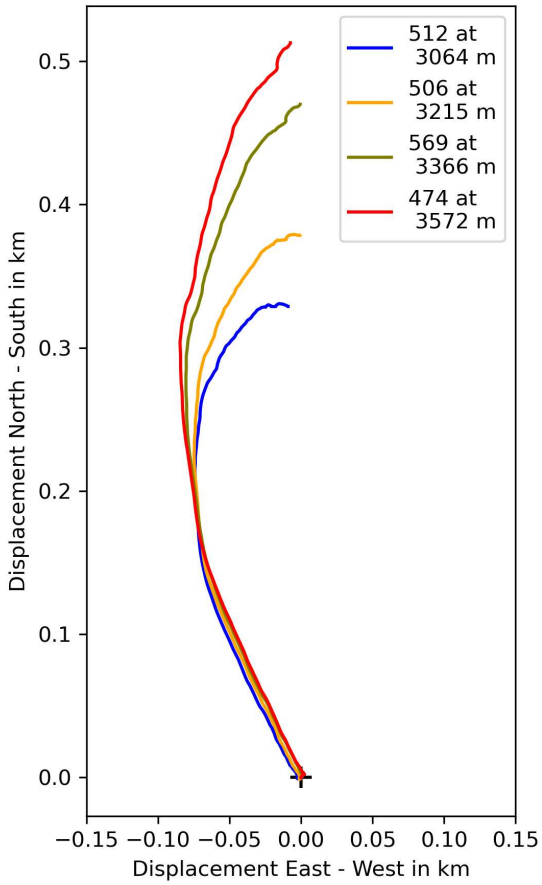

Figure 5.21.: Progressive vector diagram at the mooring location based on the ROMS simulation for a duration of 31 days. The four depth levels correspond to the depth of the current meters as shown in Figure 5.18. The black cross marks the point of zero displacement.

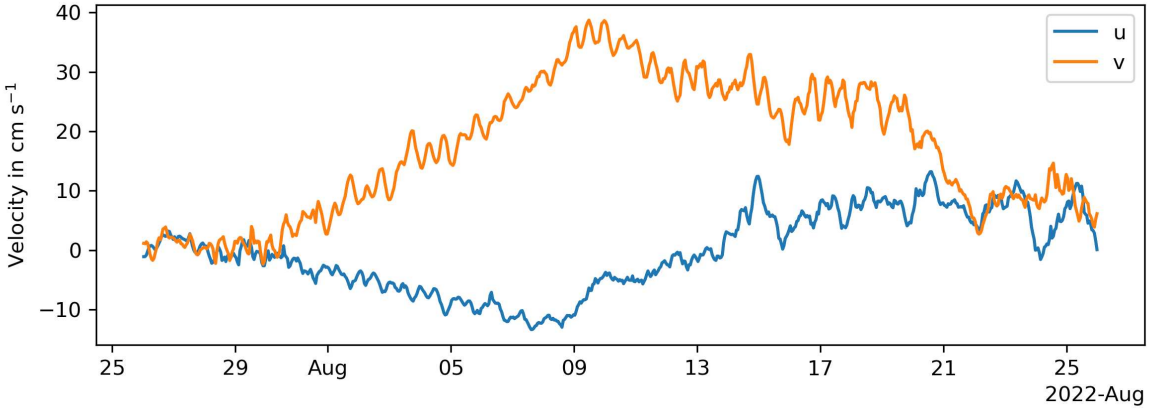

Figure 5.22.: Time series of the u and v components at the mooring location based on the ROMS simulation at the depth of 3572 m corresponding to the current meter 474.

northward component (v) and an east-west component (u) that changes its orientation with time. The four different depth levels show a very similar trajectory with a variation of 0.2 km in the northward transport. The dominant northward component is consistent with the horizontal tracer dispersion in Figure 5.16 but contradicts the results from the mooring measurements which were governed by westward currents. The displacements in the model are two orders of magnitude smaller when compared to the mooring measurements during the first month. However, when comparing the time series, where Figure 5.22 shows it exemplarily at the depth of the 474 current meter, it can be seen that the raw velocities are one order of magnitude larger in the model with maxima of approximately 40 cms^{-1}. The dominant northward and the smaller, varying east-west component are also clearly visible here.

Chapter 6.

Discussion

6.1. Plume Anomaly Determination

Temperature, Density & Salinity

Figure 6.1 compares the two sensor groups for temperature and conductivity which are the basis for the derived plume tracers. The two sensor groups follow the 1 to 1 relationship marked by the black line for both quantities, except for some outliers. Given the agreement of the two sensor groups, it is reasonable to base the analysis in this work on the primary sensor group.

During stations *PS137-018-01* and *PS137-018-01* the CTD rosette was kept at a constant depth as described in Chapter 3.5. During both periods spikes were observed in the primary CTD temperature sensor with a maximum spread of 0.0038 °C and 0.0109 °C respectively. Similar spikes are measured by the second CTD sensor but not by the MAPR instruments (see Figure 6.5). The amplitude of these spikes is of a similar order of magnitude as the temperature anomalies near the vent, resulting in $\delta\theta$ anomalies up to 0.013 °C. Due to the distance to the vent and the absence of strong anomalies in the MAPR temperature data and also in the other plume tracers, these peaks were excluded from the main analysis, but only for the CTD data. A possible reason for this could be, that the measurement was affected by the exhaust heat from the microbiological pumps. While these are the only periods, when the pumps were running for such a long time, they are also the only ones with constant depth, making it challenging to discuss the influence of the pumps. Also at least one MAPR for each of the two periods was mounted next to a pump on the CTD wire, and should therefore also record similar spikes.

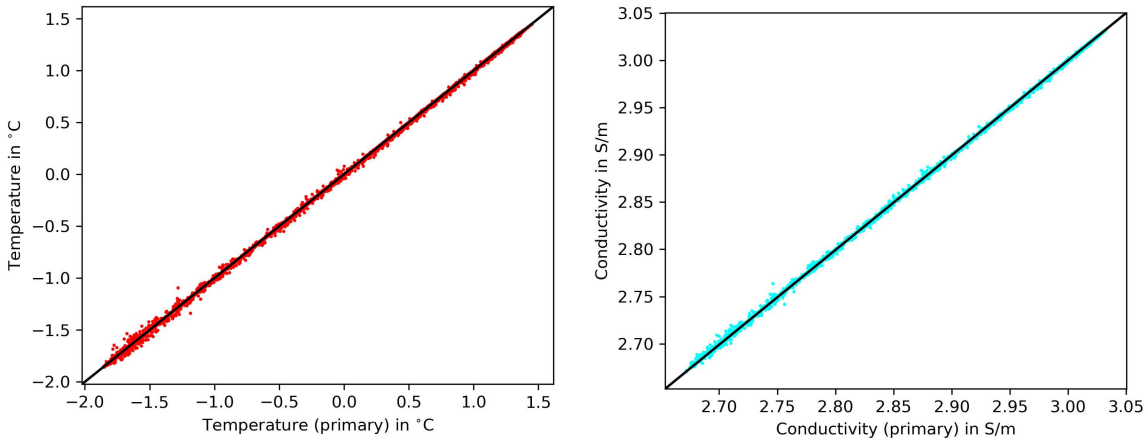

(a) **(b)**

Figure 6.1.: **(a)** Temperature and **(b)** conductivity of the primary and secondary sensors of the CTD for all measurements below 20 m at the vent site, with the black line as the 1 to 1 relationship. The limit of 20 m is chosen because the equilibration stops at the beginning of each cast are always above this depth.

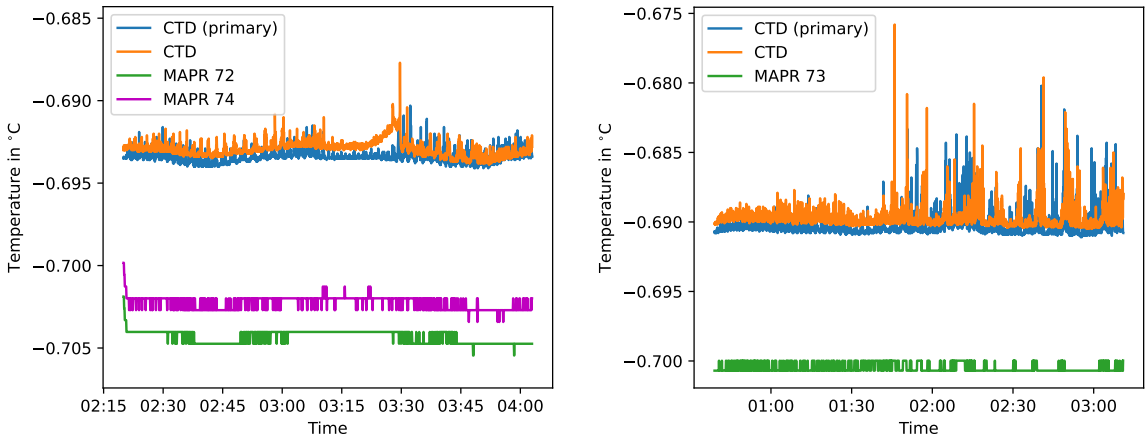

(a) **(b)**

Figure 6.2.: **(a)** Temperature measurements of the two CTD sensors and two MAPRs during the constant depth period of station *PS137-018-01*.
(b) Temperature measurements of the two CTD sensors and one MAPR during the constant depth period of station *PS137-028-01*.

In this work, two different approaches were tested to determine a plume anomaly for the potential temperature, $\Delta\theta$: the background comparison and the in-station comparison as explained in 3.5. For the first approach, station *PS137-018-01* was intended as the background profile, against which each measurement at the vent site should be compared. This method assumes similar stratification profiles without plume influence in the relevant quantities for the compared profiles. As can be seen in the Figures 5.4a for θ and 5.4b for σ_{3000} this assumption seems weak, especially since the differences are not only due to a constant offset but vary with depth. Therefore the background method was discarded for $\Delta\theta$ and the in-station comparison method (as explained in Chapter 3.5) based on [8] was implemented. Here one up- or downcast is used as the reference profile. This cast is chosen as a compromise between being close enough to the vent site to feature a similar stratification and far away enough to minimize possible θ deviations caused by plume influence in the θ-σ_{3000} relationship. While for some of the casts, the θ-σ_{3000} fit has already been adjusted to exclude this bias, its influence on the resulting profile cannot be neglected, as can be clearly seen in Figure 3.6. Therefore the in-station comparison method in this work gives conservative results with $\Delta\theta$ values being lower than they should be for the casts, where the plume influence could not be completely excluded. Figure 6.3 shows the comparison between both methods exemplarily for the station *PS137-033-01*. One can observe that they agree well below 3100 m even for single spikes. In general the in-station method gives slightly higher results. But above 3100 m the curve for the background method decreases, which occurs at a similar depth level as the turning point from minimum to maximum for the background temperature in Figure 5.4a. Therefore it can be assumed, that the in-station method is better suited in this case, as it is less dependent on the assumption of similar stratification and also gives higher $\Delta\theta$ even considering its conservative nature. The high variability in the resulting $\Delta\theta$ curve is caused by the variability in the idealized depth-θ fit, which is even increased due to the subtraction. This high variability makes it necessary to use only the envelope for determining the vertical plume extent (described in Section 6.2). Hence this method would benefit from improved processing beforehand.

For θ and σ_{3000} results based on the MAPR measurements it is important to keep their dependence on the CTD data in mind, as explained in Section 3.5, which is why the results based on the CTD data will guide the discussion in this chapter and the MAPR results will only be considered complementary. With regard to their suitability as plume tracers, the salinity S and σ_{3000} profiles were also investigated. However, for both quantities only minor variations were observed in the plume depth, with magnitudes of 0.002 PSU in practical

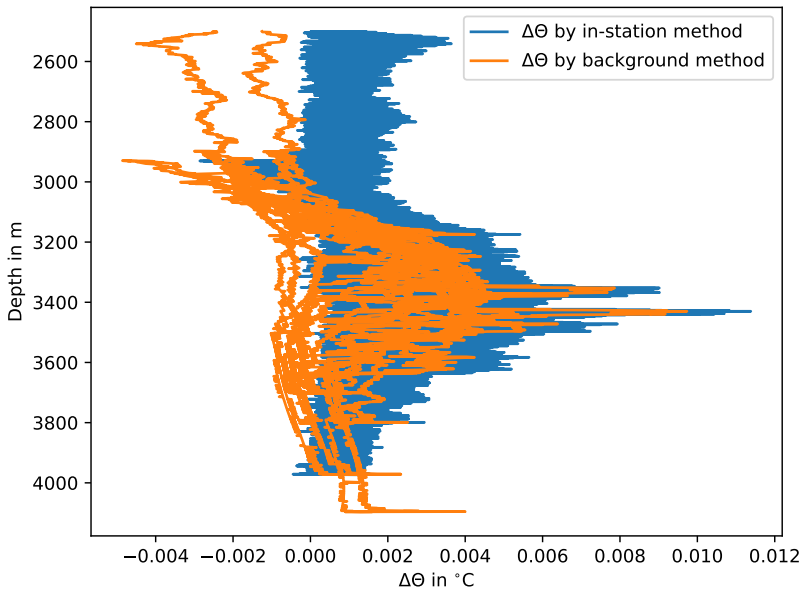

Figure 6.3.: Example comparison of the potential temperature anomaly $\Delta\theta$ for the in-station and the background comparison for station *PS137-033-01* below 2500 m.

salinity and 0.003 kg/m^3 for σ_{3000}. Therefore, in this work, they are only considered as secondary and the focus is on the other quantities.

The uncertainties of the different sensors are only partially known (see Table A.1). Also due to the lack of error propagation in the implementation of the derived quantity calculations, they can only be discussed in relation to the uncertainties of their original measured quantities. The accuracy of the CTD temperature measurements is ±0.001 °C, which would be one order of magnitude smaller than the largest temperature anomalies. But for the subtraction the accuracies compensate, resulting in only half the resolution as the uncertainty, which is ±0.0005 °C. Therefore the plume anomalies in potential temperature are much larger than the associated uncertainty, while neglecting the error propagation and the influence of the other quantities.

Electron Reduction Potential

The behavior of the E_h sensor is displayed in Figure 6.4: It shows the relation between the measured E_h and the calculated plume anomaly dE_h/dt for an exemplary station. For E_h two strong decreases at approximately 16:30 and 17:30 are visible. After the local minimum the signal increases again with several smaller peaks along the way. This can be explained by the sensor being lowered through a very strong plume layer and it's subse-

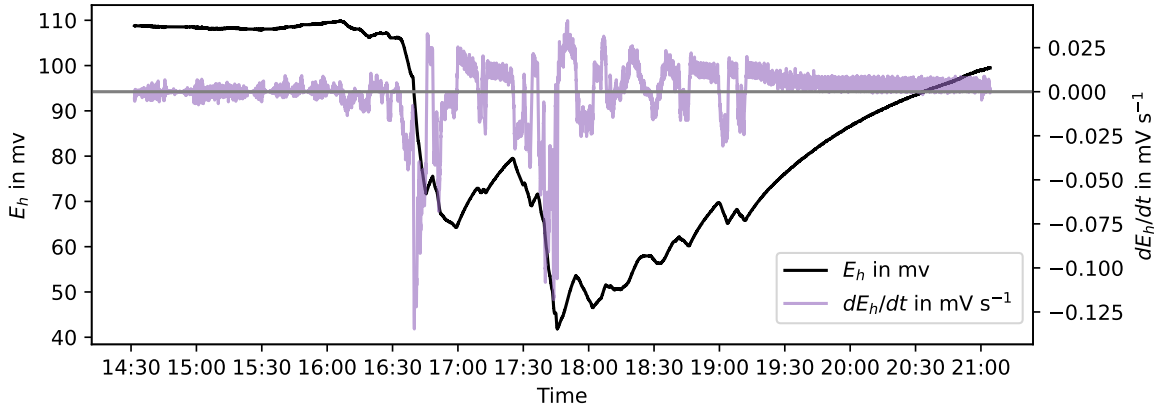

Figure 6.4.: E_h and calculated dE_h/dt versus time for station *PS137-033-01* below 1000 m. The gray horizontal line marks the level of dE_h/dt =0 mVs^{-1}.

quent relaxation to the original level, superimposed by multiple weaker plume layers. The relaxation of the sensor is slower than the initial response, resulting in the second minimum starting at the level of the first minimum. This behavior is accounted for by using the backward time derivative over 30 sec as the plume anomaly tracer, to detect decreases in E_h on the order of 10 mV to 100 mV.

Turbidity and δ^3He

As can be seen in Figure 5.9, all turbidity profiles follow roughly three separate curves. Figure 6.5a shows that these three levels are grouped by the three different MAPR instruments. This is most likely due to the different roughness of the translucent surfaces of the sensor, which affects the intensity of the transmitted light and therefore the measured result. These different levels are accounted for by calculating the turbidity anomalies relative to each instrument as described in Section 3.5.

Figure 6.5b also shows that even the background station *PS137-018-01* features elevated turbidity values below 2000 m and even peaks in the plume depth. This leaves three possibilities: First, the background station could have been inadvertently carried out close to a hydrothermal vent. Second, the turbidity signal was advected over a long distance without mixing from a distant source. Finally, that these are just general background values in this part of the Arctic Ocean. In [19] a background of approximately 0.04 NTU was measured along the Gakkel Ridge which would attribute all values except the strongest peak to the general background. When inspecting the background values for δ^3He there

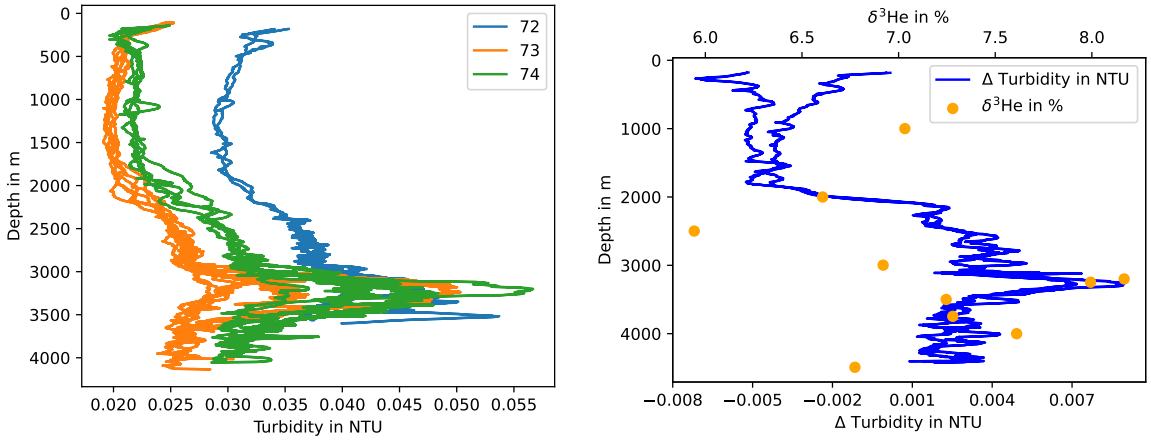

(a) **(b)**

Figure 6.5.: **(a)** Turbidity measurements at the Aurora Vent Site grouped by the three different MAPR instruments used, with the serial numbers 72, 73 and 74.
(b) Turbidity anomaly and δ^3He vs depth for the background station *PS137-018-01*.

are two slightly elevated samples at a depth of approximately 3200 m corresponding to the turbidity peaks. This two phenomenons suggests the possibility, that there is indeed a plume influence present at the background station and supports the need for background-independent anomaly calculations.

The interpretation of the anomalies for δ^3He in Figure 5.8 must also be adjusted with this assumption, although they would only be reduced by the offset depending on the true background value. In [62] the non-hydrothermal δ^3He background is estimated to be approximately 6 % based on results from PS86, which is consistent with the background values here. In principle, a higher background would also be reasonable because over time more tritiogenic helium would accumulate in deep water masses without ventilation. However, tritium measurements revealed much higher concentration in the plume depth, with approximately 0.1 TU for PS68 and 0.6 TU to 0.7 TU for the recent PS137 cruise (see Figure A.4 and Figure A.5). This contradicts this hypothesis and needs to be investigated further outside of this work.

6.2. Vertical Extent and Heat Flux

Determining the exact extent of the non-buoyant plume presents a challenge due to the many phenomena in the different instruments for the different quantities described above. Maxima in the respective plume tracers are easy to define but to derive a more or less bi-

	θ_{CTD}	dE_h/dt_{CTD}	δ^3He	θ_{MAPR}	dE_h/dt_{MAPR}	Turbidity$_{MAPR}$
z_{plume} in m	3400	3400	3100	3400	3200	3200
z_{max} in m	500	500	800	500	700	700
N^2 in $1s^{-2} \times 10^{-8}$	0.75	0.75	2.05	0.75	1.73	1.73
Heat flux in MW	1	1	18	1	8	8

Table 6.1.: Minimum plume depth z_{plume}, maximum rise height z_{max}, buoyancy frequency N^2 and estimated heat flux of the plume inferred from the different quantities, based on the maximum anomaly as in [64]. N^2 is calculated from a nearby CTD profile, station *PS137-055-01*. The constants used are listed in Table A.3.

nary condition for plume presence is strongly dependent on the choice of a threshold. A large fraction of the anomalies are above a zero level, so an additional threshold would be required. For the vertical extent this is done by the general curve of the envelope and then rounded to 100 m to account for the uncertainties of this method (see Section 5.3). Nevertheless the maximum rise height z_{max} for the different plume tracers agrees well. It also seems reasonable that the δ^3He values are the highest and the turbidity values the lowest, since its concentration can be assumed to be the most inert tracer for δ^3He and the least inert for turbidity. [64] inferred a rise height of 800 m based on the turbidity maximum at approximately 3100 m depth and calculated a heat flux of 17 MW with a stratification of N^2=2.5 $\times$ 10^{-8} s^{-1} based on measurements from the *PS86* cruise. Compared with the heat fluxes in Table 5.1 they are larger overall, but a recalculation with the depth of the maximum anomalies gives lower results (see Table 6.1). Thus the vertical plume extent seems to be smaller than for the *PS86* measurements. Since both approaches lead to quite different rise heights and heat fluxes, it is necessary to compare the maximum-based result. Nevertheless in principle the rise height should be related to the anomaly signal that reaches the highest depth, z_{plume}, although this depth is less recognizable, because it is the maximum depth to which the energy of the vent carries its tracers against the stratification.

While the minimum plume depth z_{plume} was inferred from the envelope of all upcasts and downcasts, the maximum of a plume tracer has the advantage, that it can be easily analyzed in regard to the distribution per depth. This is shown in Figure 6.6 for the CTD and the MAPR data for the continuously measured plume tracers. The $\Delta\theta$ maxima per cast are more concentrated to a smaller depth range than for dE_h/dt which reaches shallower depths. The CTD data also show some maxima at a depth of 3900 m, these are most likely caused by the buoyant plume. The turbidity anomaly maxima from the MAPRs are even more concentrated than $\Delta\theta$. The different results for each tracer discussed in this section

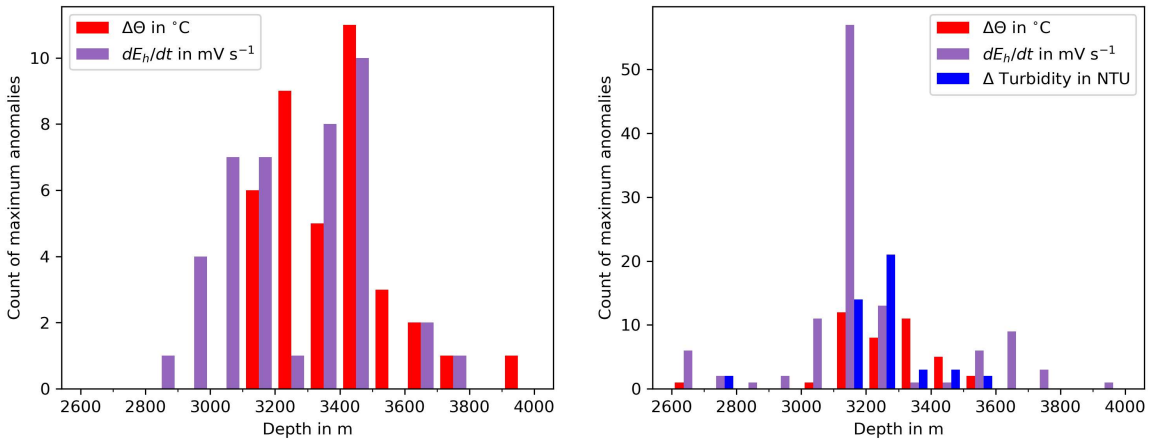

(a) **(b)**

Figure 6.6.: Distribution of the maximum anomaly per upcast or downcast binned to depth intervals of 100 m for **(a)** the CTD data and **(b)** the MAPR data.

could be explained by vent fluids exerted at different temperatures, which therefore rise to different heights, assuming different tracer compositions. This is clearly visible in Figure 6.7, which shows two maxima in $\Delta\theta$ at different depths for station *PS137-033-01*, which is also the station identified with high anomalies in Figure 5.2a. This behavior would result in not one homogenous bulk of plume fluid but a vertically heterogenous plume with different layers. ROV observations at the vent site confirm the presence of fluids with widely varying initial temperatures as described in [49].

Setting the results of the plume simulation in relation to the observed vertical extent based on δ^3He, the rise height and also the maximum anomaly agrees well for the first days of the simulation period (see Figure 5.10). The minimum plume depth z_{plume} of 2600 m is very close to the observed one at 2700 m while the maxima are further apart from each other with 3500 m for the simulation and 3100 m for the observation. For the later simulation period the tracer seems to precipitate very quickly and then accumulates only at the bottom. A possible explanation is the naive representation of δ^3He as a concentration in kg/m^3 leading to unrealistically high concentrations of 1000 kg/m^3. Reducing the tracer input in the bottom forcing to realistic levels could easily lead to a much more consistent behavior. In addition, Figure 5.11 suggests that the tracer input is not continuous although it is specified as such in the forcing file. In principle it is also still an open question, when the fluid dispersal in the simulation would reach a stationary state. While this is assumed for all interpretations in this work, it is unclear on which time scales it would reach this state or even if it would happen at all in the simulation. Figure 6.8 shows the time evolution of the vertical potential temperature profile, similar to the tracer con-

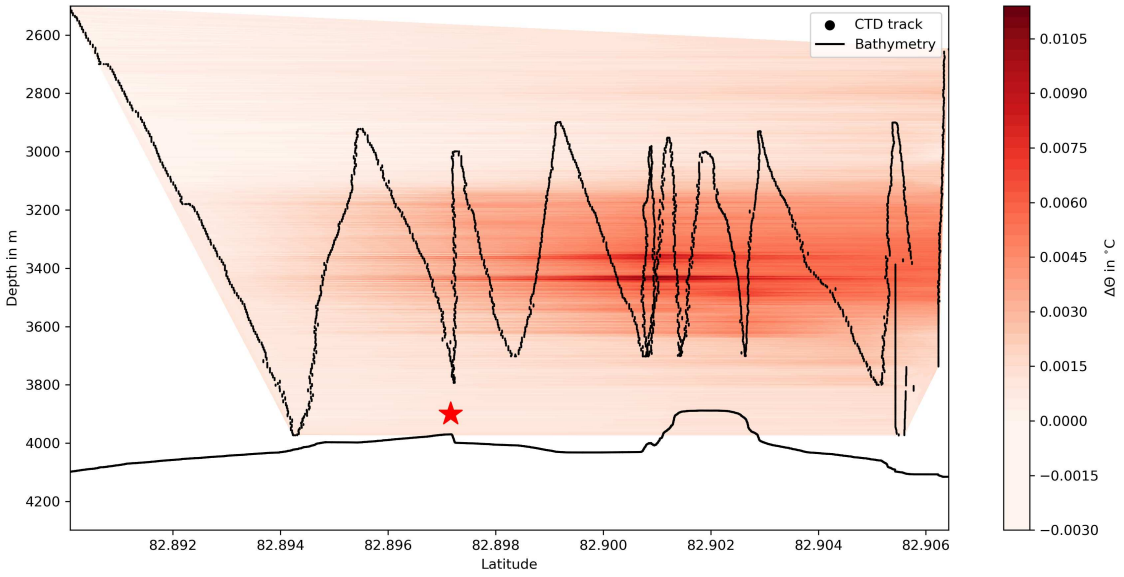

Figure 6.7.: Potential temperature anomaly $\Delta\theta$ interpolated along latitude for station *PS137-033-01*. The dots represent the CTD position obtained from the acoustic tracker, the solid line the bathymetry and the red star the vent location.

centration in Figure 5.11 before. While the profile initially agrees with the theory (see Figure2.2), almost all vertical gradients are erased during the simulation time. The initial stratification is imposed by the reanalysis data but it is not maintained by the model itself. Because of these inconsistencies, the interpretation of these results with respect to the plume dispersal should focus on the beginning of the simulation period only. However for this beginning it is shown that the setup can simulate realistic rise heights and that it can be employed for further investigations of the plume dispersal and heat flux.

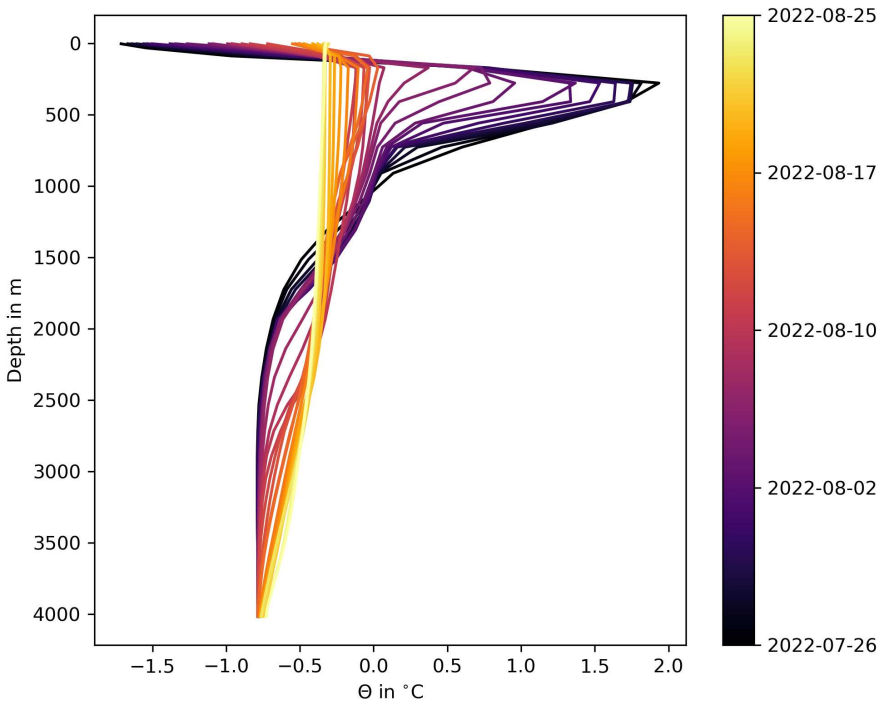

Figure 6.8.: Potential temperature θ from the ROMS simulation at the location of the simulated vent versus depth. Each line represents a daily average, with the darkest lines at the beginning and the lightest at the end of the simulation period.

6.3. Horizontal Extent

The assessment of the horizontal extent of the plume is limited by the measurement locations, which were ultimately constrained by the sea ice drift determining the ship movement, visible in the the patterns in Figure 5.12 and Figure 5.13. Nevertheless it can be seen, that high anomalies in the measured tracers are mostly confined to the immediate vicinity of the vent site, especially at the northwest flank of the Aurora seamount. This is also represented in Figure 5.14 and Figure 5.15 where most of the strongest anomalies are within 900 m of the vent. The majority of the measurements conducted on the southeastern side give only weak anomalies even close to the vent, similar as for the samples taken uphill at the top of the seamount. An exception are the δ^3He and turbidity samples directly adjacent to the vent in a distance of up to 250 m. A strong transport of hydrothermal fluid with an eastward component cannot be ruled out due to sparse measurements on that flank from this results alone. But the current observations from the mooring support a westward transport, matching the observed tracer distribution.

An interesting feature are the high turbidity anomalies in the westernmost station, station *PS137-028-01* visible in Figure 5.13c and Figure 5.15 in the section with roughly constant values. This section corresponds to the time period, when the CTD was kept at a constant depth with the microbiological pumps running, and which was removed from the CTD data set due to unreasonable temperature spikes. However, Figure 5.15 now clearly shows, that there is a high turbidity anomaly in the MAPR data, also in both deployed instruments. Therefore it remains unclear whether the data in this period could be influenced by hydrothermal plume fluid or not. If so, this would require either a more concentrated plume fluid to be advected up to 2300 m without affecting the measurements in between or another source at a closer location.

The difficulties in inferring the horizontal extent from the plume tracer signals can be discussed exemplarily with the δ^3He distribution of the CTD samples compared to the ROV sample taken directly at the vent, as shown in Figure 6.9. Compared to the vent samples with an average $\delta^3\text{He} = 674.02\,\%$, the CTD samples are one to two orders of magnitude lower, suggesting that most of the dilution of the vent fluid occurs less than 100 m away from the vent and that the dilution is far from linear with distance. The closest sample was also taken at a depth of 3205 m, approximately 700 m above the vent and thus at the depth of the non-buoyant plume layer. The δ^3He value here, which is already much smaller then the sample at the orifice, is therefore consistent with the theory, which says that the fluid is heavily diluted as it ascends in the buoyant plume. With the assumption of δ^3He as an inert tracer, a dilution factor can be calculated for each δ^3He sample starting from the average of three high temperature vent samples with approximately $\delta^3\text{He} = 674\,\%$ representing 100 % plume fluid. This results in the dilution shown by the right axis in Figure 6.9 with values between 0.7 % and 2.1 % for all samples. It also shows that the relationship of increasing dilution with distance is weak if only inferred from these data alone, due to the small number of samples and the large variation for similar distances.

The same applies to the samples taken during the previous *PS86* cruise (also shown in Figure 6.9) where the larger number of samples supports the initial results by matching the overall distribution. The single strong peak is located at a similar distance for both cruises and the other samples also vary in similar ranges. Concerning the relation of the dilution with distance, it is interesting to note that the values at even greater distances up to 5000 m do not decrease compared to samples closer to the site, which supports the assumption that the plume is already strongly diluted very close to the vent and then spreads out with a more or less constant dilution. Finally, the comparison also shows that the observations from *PS137* were taken too close to the site to define a maximum horizontal extent of the

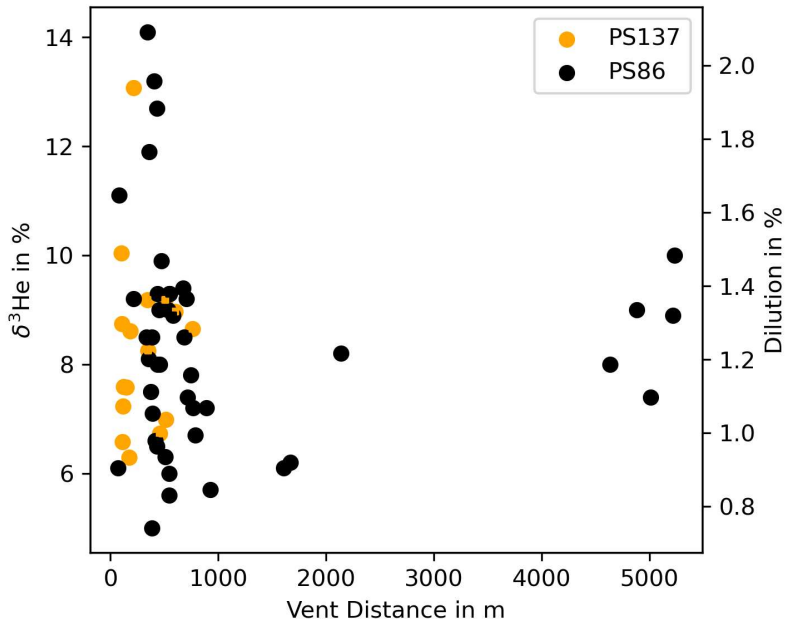

Figure 6.9.: δ^3He and dilutionfor samples below 2500 m from the cruises *PS137* and *PS86* versus geodesic distance from the vent. The dilution is the fraction between the average of three ROV samples taken at high temperature vent outlets being $\delta^3\text{He} = 674.02\,\%$ and the CTD sample.

plume, since samples from the *PS86* cruise at a distance even greater than 1000 m show similar values.

Calculating a similar dilution based on the temperature anomaly for *PS137*, which is not inert in principle but which was also measured directly at the vent, gives a maximum dilution of 0.002 % for a distance of 600 m and 0.0012 % for a distance of 2475 m, the latter being the sample taken farthest away from the vent site. The lower order of magnitude is reasonable given the less inert nature of this tracer.

When interpreting the results, especially for horizontal dispersal, another important uncertainty is the exact location and area of the vent field. The reference location used in this work is the location of the first discovered active chimneys. During the *PS137* expedition several additional chimneys were found, which also increases the area of possible plume fluid sources. These additional chimneys are located further down the seamount flank to the South-East [30]. This example shows that an exact location of the source is already a simplification and undiscovered chimneys could easily extend the area of fluid sources to hundreds of square meters, although the recent discoveries do not fit with the location of the maximum anomalies shown above. Figure 5.14a shows the highest tem-

perature anomalies more than 400 m from the assumed vent location. This also supports a larger extent of the vent field, especially since the highest of these $\delta\theta$ anomalies is located close to the seafloor and is therefore most likely part of the buoyant plume. It has also to be mentioned that the acoustic position tracker used for georeferencing the CTD rosette is assumed to give the true position, although the system is known to be prone to errors. While some of them are corrected as described in Section 3.5, it can not be proven that the remaining measurements are correct.

The horizontal dispersal of the plume resulting from the simulation is very different from the observational data. The different behavior of the model tracer, the accumulation at the seafloor as described above, is one likely cause. However, the most notable deviation here is the rapid advection of a concentrated plume to the north, leaving only very low tracer concentrations near the vent site. This does not match the diffuse, unconcentrated presence of plume tracers in the observational data, which gave the strongest anomalies to the northwest close to the vent. Most likely an unrealistic representation of the circulation causes the contradictory dispersal in the simulation, which will be discussed in the following section. Again, it is important to investigate the reason for the tracer accumulation at the bottom on longer timescales further and whether the tracer input is actually continuous as specified.

6.4. Currents and Plume Dispersal in Time

The current observations at the Aurora Vent Site reveal some remarkable features. For one the u and v components measured by the moored current meters are low, with all values below 7 cms^{-1} magnitude, while the Aquadopp measurements go up to approximately 12 cms^{-1}. But the Aquadopp measurement period corresponds to only two data points of the moored current meters, which are already 1-hour averaged values, which has to be kept in mind when comparing the two. This 1-hour averaged already reduces the maximum amplitude which can be measured by the mooring in principle. The different magnitudes indicate a higher variability in current speeds than the moored current meters alone can capture. The mean current direction to the west is dominant for the Aquadopp data, but for the moored current meters, a relevant fraction of approximately 15 % to 20 % of the values is also oriented to the east, except for the lowest moored current meter 474. This can be clearly seen in the progressive vector diagram (Figure 5.18).

Therefore in terms of direction now the short-term Aquadopp measurement is unable to capture this variability.

Due to the lack of direct current measurements in similar regimes nearby it is difficult to set these results into context. The closest regular mooring observations in this region are conducted south of the Gakkel Ridge in the Fram Strait. There, in the strong boundary current, the velocities are an order of magnitude higher, as reported in [33] and [22]. This at least leads to the conclusion that a strong, larger scale current is absent at the Aurora site which is consistent with the main current direction being across the ridge valley and not along it. A valley-based circulation pattern as described for the Mid-Atlantic Ridge Valley in [34] can therefore be ruled out.

The 474 current meter, which is only 328 m above the seafloor measured very different currents than the others: It has a much less strong westward direction with approximately 40 % of the data points having an eastward component. The strong difference and the less clear direction could be explained by two separate flow regimes, where the upper one is governed by a slow westward current but the one close to the seafloor is strongly influenced by topographic interaction, which breaks the westward current at the Aurora Seamount.

The peaks in the spectrogram in Figure 5.20 indicate that the currents are modified by tidal and inertial forces. Since the vent site is close to the critical latitude where $f_C \approx f_{Tides}$, it is not possible to distinguishing clearly between these two. The influence of the tidal motions has already been discussed in [62] based on the same dataset but here it is shown, that their contribution to the spectrum is the dominant one, with the strongest amplitude at the frequencies close to the semidiurnal and the inertial ones. Low current velocities in combination with the tidal and inertial wave motion cause the plume to stay close to the vent site and being only advected back and forth in a limited area. It also supports the hypothesis presented in [62] that bottom trapped waves govern the plume dispersal to some extent.

The representation of currents in the simulation falls short based on a first analysis. The mean direction and strength of the current at the location corresponding to the mooring shows a very different direction and magnitude than the mooring data, also at the four different depth levels. All of them show a strong westward component, while the simulation results show a northward displacement. The currents in the simulation are also an order of magnitude larger. While the current system is very clearly not represented realistically, it can explain the northward transport of the tracer well (Figure 5.16). The

high velocities are consistent with the rapid advection away from the area of interest and out of the model domain. It has to be noted that the domain has only an area of approximately 20 km × 20 km, where it is unlikely to simulate meso-scale to synoptic circulation patterns if they are not imposed by the boundary conditions. The adaption of multiple nested domains covering different scales as also employed in [66] would likely improve the simulated hydrography. Additionally the mooring data could be used directly to nudge the simulation at the corresponding location, in a similar ways as it is already used for the boundary conditions. The absence of influence of ocean-surface interaction does also not necessarily has to hold true as is discussed in [14] and currently investigated. Regarding the representation of topography-influenced currents, it should also to be mentioned that the bathymetry is heavily distorted by the smoothing during the grid generation. Comparing the data in Figure 3.2 and the model domain in Figure 4.1, shows that even the Aurora seamount itself is no longer distinguishable.

Chapter 7.

Conclusion and Outlook

The main results of this work with respect to the spatial plume dispersal are summarized in Figure 7.1. The maximum anomaly per up- or downcast for each tracer as the clearest plume signal is displayed and combines the information about the vertical and horizontal extent. It shows that most of the strong anomalies are grouped over a narrow depth range of 3100 m to 3500 m, corresponding to the depths of the maximum anomalies described in Section 5.2. This marks the core region of the buoyant plume, with the total plume extent being larger, up to a depth of 2700 m. The order of magnitude of the estimated heat flux from the vent system also depends strongly on choosing the depth of this core region or the depth of the highest anomaly as the plume rise height, resulting in heat fluxes between 1 MW and 181 MW based on E_h measurements. Similar results in respect to the vertical

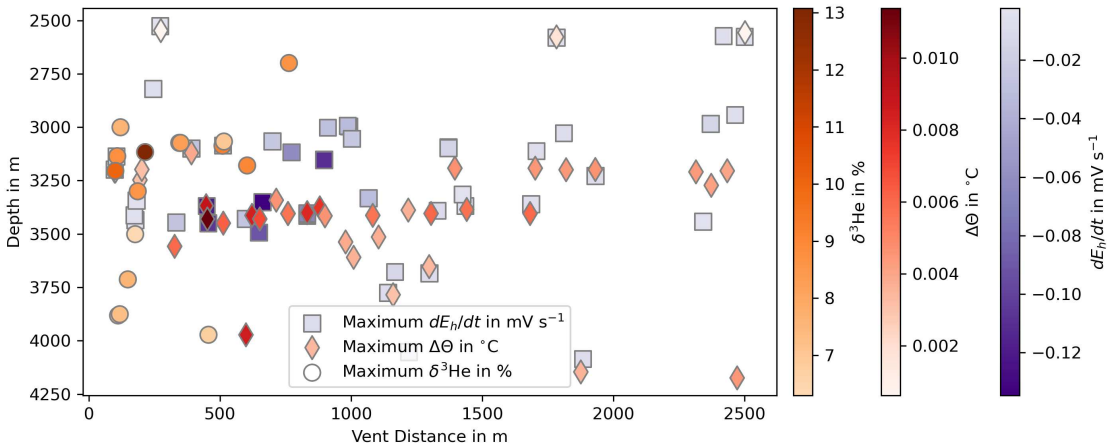

Figure 7.1.: Depth and geodesic distance from the vent site for the maximum anomaly in dE/dt, $\Delta\theta$ and δ^3He per upcast or downcast for all CTD measurements below 2500 m. The horizontal axis represents the mean distance of each cast from the vent side.

extent are obtained by the simulation of the passive tracer in the ROMS model, although they cannot be sustained by the dynamics in the setup used here. The visible offset between the vent location and the core of the buoyant plume can be explained by advection as one possible cause. But the other possibility would be, that the main hydrothermal fluid outflow is actually not located at the assumed coordinates but approximately 400 m to 600 m to the north-northwest. This is supported by the one $\Delta\theta$ maximum near the seafloor which indicates, that the buoyant plume is also located there.

Several approaches have been investigated to derive the discussed plume anomalies, depending on the characteristics of the available data. These methods can strongly influence the results and are a major source of uncertainty in the determination of the plume extent. They could be improved by utilizing true background measurements free from hydrothermal plume influence but also with a similar hydrography. Another strategy would be to investigate the possible plume dispersal based on density profiles. The CTD rosette data could be complemented by the data from additional long-term CTD probes that where also deployed at the AURORA 1 mooring and which have not been analyzed yet. Together with the density characteristics of the confirmed plume measurements from the CTD rosette, the vertical extent could be constrained further.

The varying location of the anomalies with respect to the different tracers supports the hypothesis of an inhomogeneous fluid composition and hence also an varying spatial dispersal, resulting in an inhomogeneous, patchy, non-buoyant plume layer. Anomalies in the horizontal plume were detected up to 2500 m from the vent site. Only a small-scale northwestward advection was observed in the vicinity of the presumed vent location. Thus, the plume is not spreading continuously in one direction but remains close to the vent site and is diluted there over time. This is in agreement with the results from previous measurements from the *PS86* expedition although a larger horizontal extent could be observed there.

The horizontal dispersal of the plume can be explained by the observed currents: The non-buoyant plume remains at the vent site due to very low mean velocities. Combined with tidal or inertial oscillations with frequencies of one and two cycles per day the plume is likely to move only back and forth in a limited area of a few square kilometres. Only the inert δ^3He tracer can be detected at greater distances due to its long lifetime. However, the simulation showed a very different behavior with strong northward currents causing a rapid advection of the plume tracer, leaving only a very small amount of it near the vent site. Thus, neither the current system nor the horizontal plume dispersal is realistically represented in the simulation.

It can be concluded that a more thorough investigation of the hydrographic conditions at the Aurora Site is necessary to determine the plume dispersal more accurately, both in terms of the observational data and the simulation results. While the acquisition of more data requires a great deal of effort, the simulation could be an easily accessible tool with some improvements. This is very promising because the setup presented in this work barely scratches the surface of ROMS' capabilities. The first step would be to realistically simulate the current system and scale the setup accordingly, but ultimately it could even be extended to investigate biogeochemical question related to the dispersal of hydrothermal plumes.

Appendix A.

Additional Figures & Tables

	Serial Numbers per instrument	**Accuracy, Resolution**	**Description**
CTD			SBE 911plus
Temperature	2460, 2417	±0.001 °C, 0.0002 °C	SBE3plus
Conductivity	2055, 2054	±0.0003 S/m, 0.0003 S/m	SBE4c
Pressure	0485	±0.9 m, 0.105 m	SBE9
Turbidity	72,73,74		Seapoint Turbidity Meter
ORP	4,72,73,74		Electron Reduction Potential, *PMEL*

Table A.1.: Sensor configuration of the CTD system and MAPR used on the cruise *PS137* with the device name, the serial number, the accuracy if known and a short description. Sampling frequencies for the CTD sensors equals 24 Hz and for the MAPR sensors 0.2 Hz. Based on [49] and [53].

Device	Depth in m	Height in m	Designation	Serial Number
CTD logger	114	3759	SBE37	7729
Current meter	3064	791	RCM11	512
CTD logger	3064	791	SBE37	10938
Current meter	3215	640	RCM11	506
CTD logger	3215	640	SBE37	10935
Current meter	3366	489	RCM11	569
CTD logger	3366	489	SBE37	10939
Current meter	3572	283	RCM11	474
CTD logger	3572	283	SBE37	10936

Table A.2.: Setup of sensors in the mooring at the Aurora vent site. Depth is the depth below sea surface and height is the height above the seafloor. The sampling frequency for the CTD loggers and the current meter was set to 1 hour. The accuracies for the CTD loggers are for conductivity ±0.0003 S/m, for temperature ±0.0002 °C and for pressure ±7 m. The accuracy for the current meters is ±0.15 cm/s. The CTD loggers are not used in this work. Based on [52] and [1].

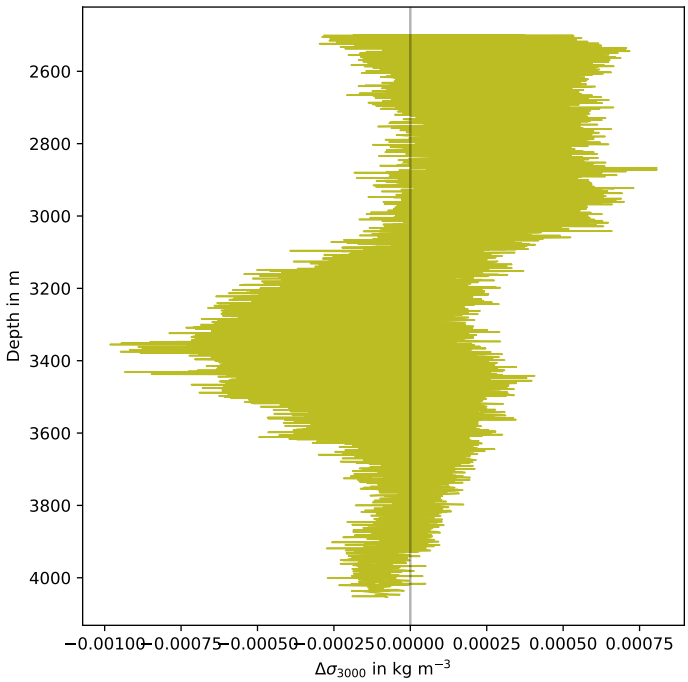

Figure A.1.: Anomalies in σ_{3000} for all MAPR measurements at the Aurora Vent Field compared to the fit of the background profile. The black line marks the level of zero deviation.

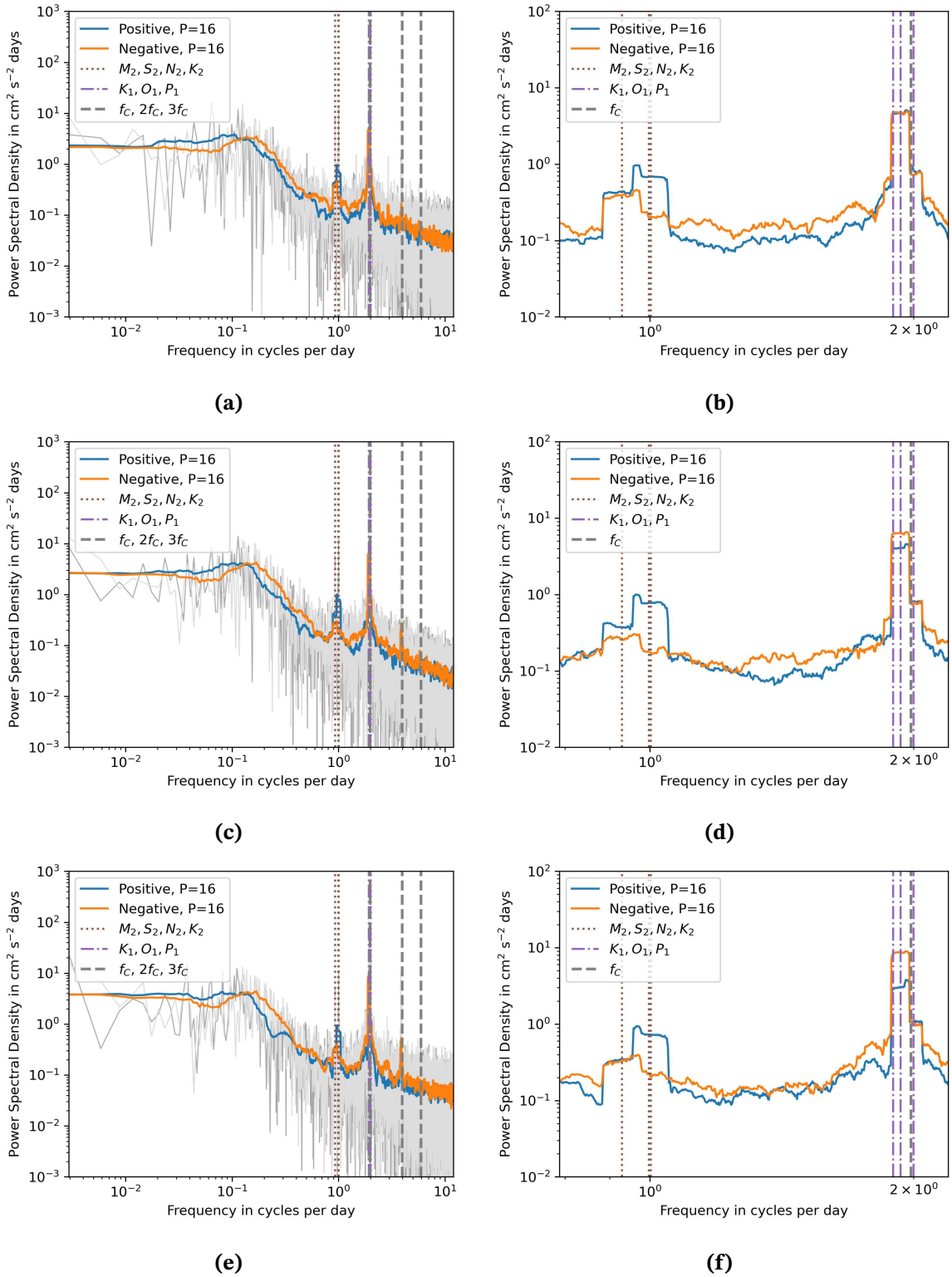

Figure A.2.: Spectral estimates of the positive (blue) and negative (orange) rotating components of the current meters 512 (**(a)** and **(b)**), 506 (**(c)** and **(d)**) and 569 (**(e)** and **(f)**) for the full frequency range (left) and a close-up on the peaks at 1 and 2 cycles per day (right). It is filtered with the multitaper method with $P = 16$, while the grey background represents the unfiltered components. The dominant seven tidal frequencies are marked by the dotted and dashed-dotted lines and the Coriolis frequency f_C as well as its multiples by the dashed lines. Tidal frequencies based on [28].

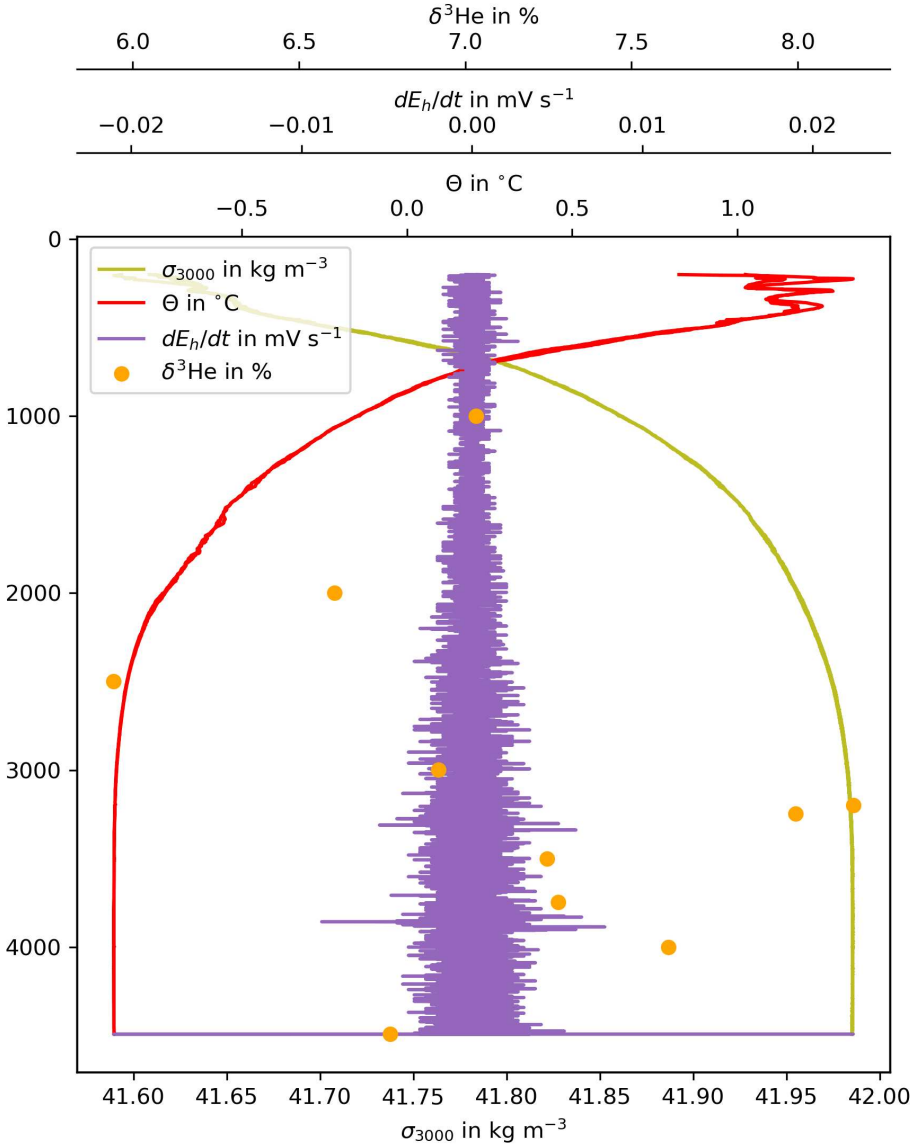

Figure A.3.: δ^3He, dE_h/dt, θ and σ_{3000} versus depth for the background station *PS137-018-01*.

ρ_0	c_p	g	α
$1000\,\mathrm{kgm}^{-3}$	$3890\,\mathrm{Jkg}^{-1}\mathrm{K}^{-1}$	$9.8\,\mathrm{ms}^{-2}$	$1.3\times10^{-4}\,\mathrm{K}^{-1}$

Table A.3.: Physical constants used in the calculation of the heat flux.

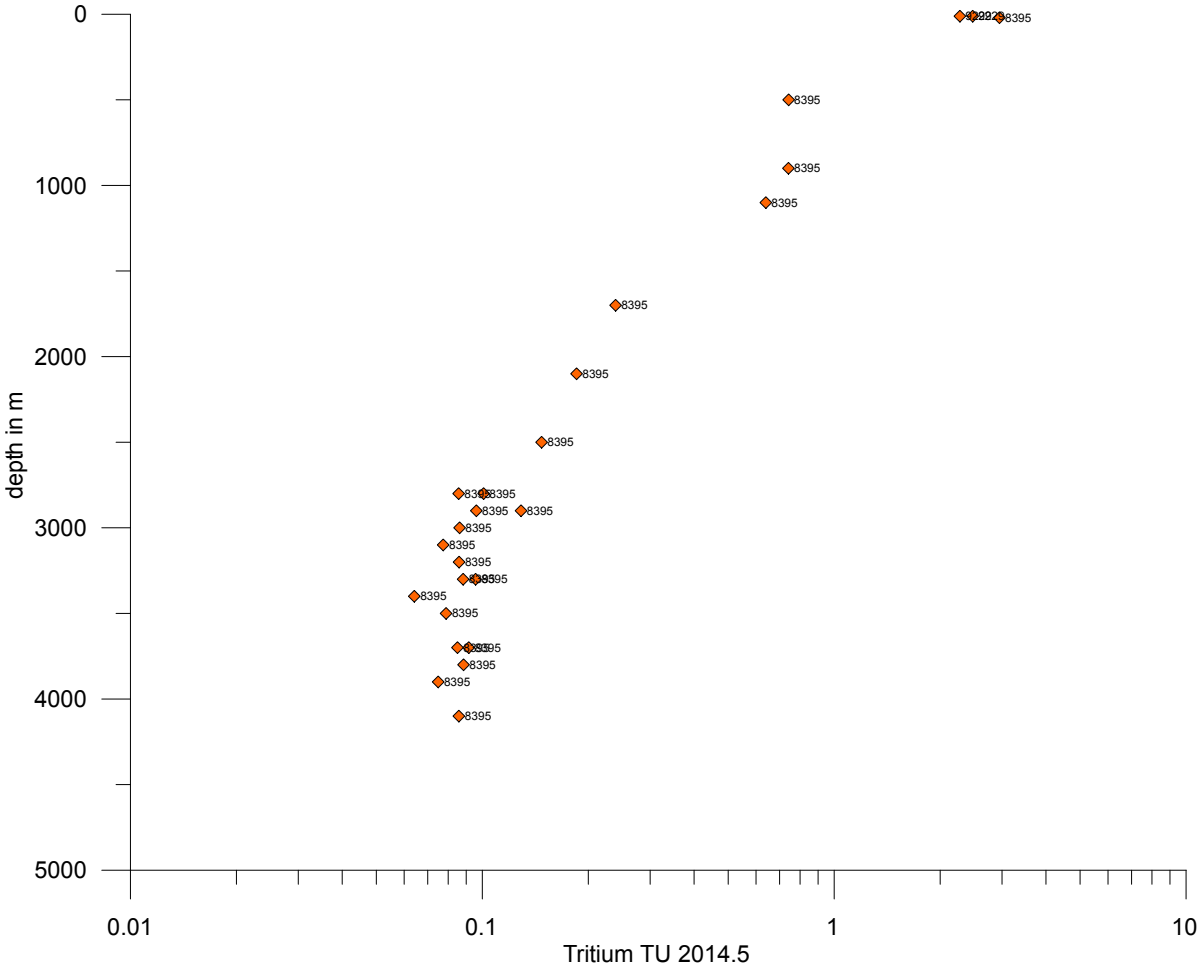

Figure A.4.: Tritium concentration based on the *PS86* cruise modified from [Sültenfuss, J., personal communication, Jan. 2025].

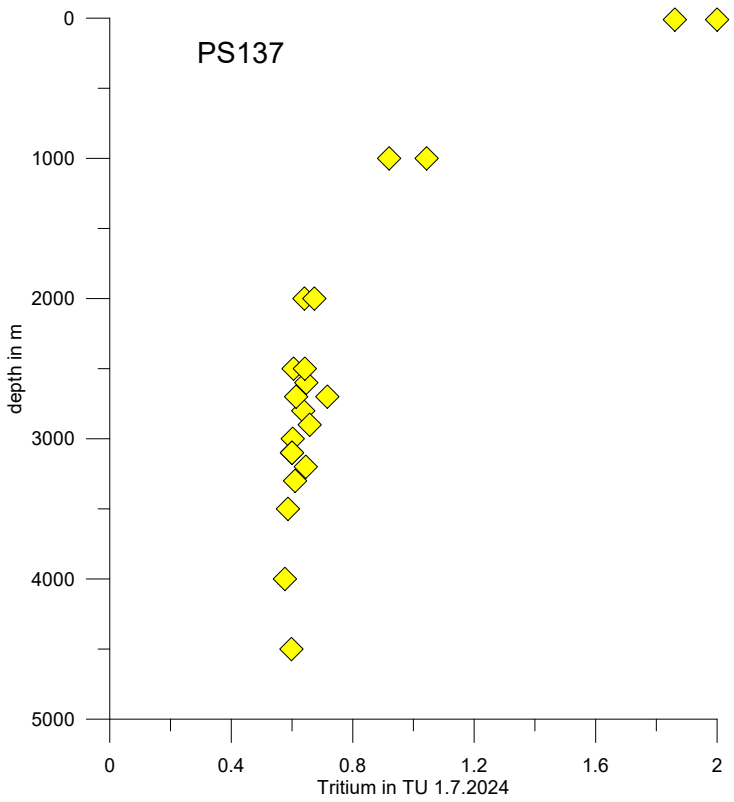

Figure A.5.: Tritium concentration based on the *PS137* cruise modified from [Sültenfuss, J., personal communication, Jan. 2025].

Appendix B.

Software

B.1. Data Processing

The *SeaBird* software was used in the version 7.26.2.14 and can be downloaded at https://software.seabird.com/. The processing setting files are documented in [43]. Further processing and analysis was done in *Python v3.11.11* using the *SpyderIDE v6.0.5* and *Jupyter Lab*. The code is documented in two separated parts. The *hy-vent* package [44] contains the necessary functions for analysis and plotting. The code to create the specific results shown in this work is documented in [43].

B.2. ROMS Application and Setup

The ROMS application as used in this work, is documented at [42]. ROMS was used in the release version ROMS/TOMS 4.2 from 19/03/2025. The modified version of ROMS including the passive tracer is documented at [3]. The model was build and run on Linux *Ubuntu* 22.04. LTS with the *gfortran* compiler v11.4.0 and *GNU make* v4.3.

The initial and boundary condition files, as well as the heat flux forcing file were created with *MATLAB* scripts kindly provided by G. Xu. They can be made available on request. *MATLAB* was used in the version 23.2.0.2515942 (R2023b) Update 7.

B.3. Usage of AI based Applications

AI based applications were used in this work in the following way: DeepL was used to assist with spelling and wording mistakes as well as for translations from German to English. The *Meta-llama* model in the version Llama-3.3-70B-Instruct and previous ones implemented at HuggingFace was used to assist in code understanding and conception.

Bibliography

1 AANDERAA: *Aandereaa Doppler Current Meter RCM 11 Datasheet*. Aanderaa, Oct. 2004

2 ARANGO, H. G.: *ROMS Matlab Processing Scripts*. https://github.com/myroms/roms_matlab. Version: Oct. 2023

3 ARANGO, H. G. ; METTE, J. : *jmetteUni/roms: Thesis version*. http://dx.doi.org/10.5281/ZENODO.15420448. Version: 2025

4 In: ARBIC, B. K. ; ALFORD, M. H. ; ANSONG, J. K. ; BUIJSMAN, M. C. ; CIOTTI, R. B. ; FARRAR, J. T. ; HALLBERG, R. W. ; HENZE, C. E. ; HILL, C. N. ; LUECKE, C. A. ; MENEMENLIS, D. ; METZGER, E. J. ; MÜELLER, M. ; NELSON, A. D. ; NELSON, B. C. ; NGODOCK, H. E. ; PONTE, R. M. ; RICHMAN, J. G. ; SAVAGE, A. C. ; SCOTT, R. B. ; SHRIVER, J. F. ; SIMMONS, H. L. ; SOUOPGUI, I. ; TIMKO, P. G. ; WALLCRAFT, A. J. ; ZAMUDIO, L. ; ZHAO, Z. : *A Primer on Global Internal Tide and Internal Gravity Wave Continuum Modeling in HYCOM and MITgcm*. GODAE OceanView, 2018

5 BAKER: *Tracking Down Hydrothermal Vents*. https://blogs.agu.org/geospace/2015/11/25/tracking-down-hydrothermal-vents/. Version: Nov. 2015

6 BAKER, E. T.: MAPR: A new instrument for hydrothermal plume mapping. In: *RIDGE events* 8 (1997), S. 23–25

7 BAKER, E. T. ; CHEN, Y. J. ; MORGAN, J. P.: The relationship between near-axis hydrothermal cooling and the spreading rate of mid-ocean ridges. In: *Earth and Planetary Science Letters* 142 (1996), Nr. 1-2, S. 137–145. http://dx.doi.org/https://doi.org/10.1016/0012-821X(96)00097-0. – DOI https://doi.org/10.1016/0012–821X(96)00097–0

8 BAKER, E. T. ; EDMONDS, H. N. ; MICHAEL, P. J. ; BACH, W. ; DICK, H. J. ; SNOW, J. E. ; WALKER, S. L. ; BANERJEE, N. R. ; LANGMUIR, C. H.: Hydrothermal venting in magma deserts: The ultraslow-spreading Gakkel and Southwest Indian Ridges. In:

Geochemistry, Geophysics, Geosystems 5 (2004), Nr. 8. http://dx.doi.org/https://doi.org/10.1029/2004GC000712. – DOI https://doi.org/10.1029/2004GC000712

9 In: BAKER, E. T. ; GERMAN, C. R.: *On the Global Distribution of Hydrothermal Vent Fields*. American Geophysical Union (AGU), 2004. – ISBN 9781118665879, S. 245–266

10 BAKER, E. T. ; MARTINEZ, F. ; RESING, J. A. ; WALKER, S. L. ; BUCK, N. J. ; EDWARDS, M. H.: Hydrothermal cooling along the Eastern Lau Spreading Center: No evidence for discharge beyond the neovolcanic zone. In: *Geochemistry, Geophysics, Geosystems* 11 (2010), Aug., Nr. 8. http://dx.doi.org/10.1029/2010gc003106. – DOI 10.1029/2010gc003106. – ISSN 1525–2027

11 BECKMANN, A. ; HAIDVOGEL, D. B.: Numerical simulation of flow around a tall isolated seamount. Part I: Problem formulation and model accuracy. In: *Journal of Physical Oceanography* 23 (1993), Nr. 8, S. 1736–1753

12 BJÖRK, G. ; WINSOR, P. : The deep waters of the Eurasian Basin, Arctic Ocean: Geothermal heat flow, mixing and renewal. In: *Deep Sea Research Part I: Oceanographic Research Papers* 53 (2006), jul, Nr. 7, S. 1253–1271. http://dx.doi.org/10.1016/j.dsr.2006.05.006. – DOI 10.1016/j.dsr.2006.05.006

13 BOETIUS, A. : *The Expedition PS86 of the Research Vessel POLARSTERN to the Arctic Ocean in 2014*

14 BRACAMONTES RAMÍREZ, J. ; WALTER, M. : Observations of deep near-inertial internal waves in the Eurasian Basin. (2025), Jan. http://dx.doi.org/10.5194/egusphere-egu24-1892. – DOI 10.5194/egusphere–egu24–1892

15 BUDGELL, W. P.: Numerical simulation of ice-ocean variability in the Barents Sea region: Towards dynamical downscaling. In: *Ocean Dynamics* 55 (2005), Jul., Nr. 3–4, S. 370–387. http://dx.doi.org/10.1007/s10236-005-0008-3. – DOI 10.1007/s10236–005–0008–3. – ISSN 1616–7228

16 BUSS, A. : *Plume dispersal at hydrothermal vent fields with natural CO2 seeps in the North-West Pacific*, University of Bremen, Master Thesis, Jun. 2011

17 COCHRAN, J. R. ; KURRAS, G. J. ; EDWARDS, M. H. ; COAKLEY, B. J.: The Gakkel Ridge: Bathymetry, gravity anomalies, and crustal accretion at extremely slow spreading rates. In: *Journal of Geophysical Research: Solid Earth* 108 (2003), Nr. B2. http://dx.doi.org/https://doi.org/10.1029/2002JB001830. – DOI https://doi.org/10.1029/2002JB001830

18 COLBERG, F. ; BRASSINGTON, G. B. ; SANDERY, P. ; SAKOV, P. ; AIJAZ, S. : High and medium resolution ocean models for the Great Barrier Reef. In: *Ocean Modelling* 145 (2020), Jan., S. 101507. http://dx.doi.org/10.1016/j.ocemod.2019.101507. – DOI 10.1016/j.ocemod.2019.101507. – ISSN 1463–5003

19 EDMONDS, H. ; MICHAEL, P. ; BAKER, E. ; CONNELLY, D. ; SNOW, J. ; LANGMUIR, C. ; DICK, H. ; MÜHE, R. ; GERMAN, C. ; GRAHAM, D. : Discovery of abundant hydrothermal venting on the ultraslow-spreading Gakkel ridge in the Arctic Ocean. In: *Nature* 421 (2003), Nr. 6920, S. 252–256. http://dx.doi.org/https://doi.org/10.1038/nature01351. – DOI https://doi.org/10.1038/nature01351

20 EROFEEVA, S. ; EGBERT, G. : *Arc5km2018: Arctic Ocean Inverse Tide Model on a 5 kilometer grid, 2018*

21 EUROPEAN UNION-COPERNICUS MARINE SERVICE: *Global Ocean Physics Reanalysis*

22 FAHRBACH, E. ; MEINCKE, J. ; ØSTERHUS, S. ; ROHARDT, G. ; SCHAUER, U. ; TVERBERG, V. ; VERDUIN, J. : Direct measurements of volume transports through Fram Strait. In: *Polar Research* 20 (2001), Dec., Nr. 2, S. 217–224. http://dx.doi.org/10.1111/j.1751-8369.2001.tb00059.x. – DOI 10.1111/j.1751–8369.2001.tb00059.x. – ISSN 1751–8369

23 FENNEL, K. ; WILKIN, J. ; LEVIN, J. ; MOISAN, J. ; O'REILLY, J. ; HAIDVOGEL, D. : Nitrogen cycling in the Middle Atlantic Bight: Results from a three-dimensional model and implications for the North Atlantic nitrogen budget. In: *Global Biogeochemical Cycles* 20 (2006), Jul., Nr. 3. http://dx.doi.org/10.1029/2005gb002456. – DOI 10.1029/2005gb002456. – ISSN 1944–9224

24 FIRING, E. ; , FILIPE ; BARNA, A. ; ABERNATHEY, R. : *TEOS-10/GSW-Python: v3.4.1.post0*

25 FOFONOFF, N. ; MILLARD, R. : *Algorithms for computation of fundamental properties of seawater*. https://unesdoc.unesco.org/ark:/48223/pf0000059832_eng. Version: 1983

26 GEBCO BATHYMETRIC COMPILATION GROUP 2023: *The GEBCO_2023 Grid - a continuous terrain model of the global oceans and land.*

27 GERMAN, C. R. ; REEVES, E. P. ; TÜRKE, A. ; DIEHL, A. ; ALBERS, E. ; BACH, W. ; PURSER, A. ; RAMALHO, S. P. ; SUMAN, S. ; MERTENS, C. ; WALTER, M. ; RAMIREZ-LLODRA, E. ; SCHLINDWEIN, V. ; BÜNZ, S. ; BOETIUS, A. : Volcanically hosted venting

with indications of ultramafic influence at Aurora hydrothermal field on Gakkel Ridge. In: *Nature Communications* 13 (2022), October, Nr. 1, S. 6517–. http://dx.doi.org/10.1038/s41467-022-34014-0. – DOI 10.1038/s41467–022–34014–0

28 GILL, A. E.: Atmosphere-Ocean Dynamics

29 IOC ; SCOR ; IAPSO: *The international thermodynamic equation of seawater – 2010: Calculation and use of thermodynamic properties.* NESCO (English), 196 pp., 2010

30 ISLER, T. ; JAKUBA, M. ; KWASNITSCHKA, T. ; PURSER, A. ; KLESH, A. ; SCHLINDWEIN, V. ; GERMAN, C. R.: High-resolution bathymetry coupled with 3D models of hydrothermal vents from opportunistically-acquired imagery: Aurora vent field, Arctic Ocean. In: *Journal of Maps* 20 (2024), Sept., Nr. 1. http://dx.doi.org/10.1080/17445647.2024.2404878. – DOI 10.1080/17445647.2024.2404878. – ISSN 1744–5647

31 JAMES, C. : *GridBuilder v1.3.3*. https://austides.com/downloads/. Version: March 2023

32 KANZOW, T. ; BORNEMANN, H. (Hrsg.) ; SAWADKUHI, S. A. (Hrsg.): *The Expedition PS131 of the Research Vessel POLARSTERN to the Fram Strait in 2022*

33 KARAM, S. ; HEUZÉ, C. ; HOPPMANN, M. ; STEUR, L. de: Continued warming of deep waters in the Fram Strait. In: *Ocean Science* 20 (2024), Jul., Nr. 4, S. 917–930. http://dx.doi.org/10.5194/os-20-917-2024. – DOI 10.5194/os–20–917–2024. – ISSN 1812–0792

34 LAHAYE, N. ; GULA, J. ; THURNHERR, A. M. ; REVERDIN, G. ; BOURUET-AUBERTOT, P. ; ROULLET, G. : Deep Currents in the Rift Valley of the North Mid-Atlantic Ridge. In: *Frontiers in Marine Science* 6 (2019), Sept. http://dx.doi.org/10.3389/fmars.2019.00597. – DOI 10.3389/fmars.2019.00597. – ISSN 2296–7745

35 LAVELLE, J. W.: Buoyancy-driven plumes in rotating, stratified cross flows: Plume dependence on rotation, turbulent mixing, and cross-flow strength. In: *Journal of Geophysical Research: Oceans* 102 (1997), feb, Nr. C2, S. 3405–3420. http://dx.doi.org/10.1029/96jc03601. – DOI 10.1029/96jc03601

36 LILLY, J. M.: *jonathanlilly/time-series: Ocean / Atmosphere Time Series Analysis v0.31*

37 LUPTON, J. E. ; DELANEY, J. R. ; JOHNSON, H. P. ; TIVEY, M. K.: Entrainment and vertical transport of deep-ocean water by buoyant hydrothermal plumes. In: *Nature* 316 (1985), Aug., Nr. 6029, S. 621–623. http://dx.doi.org/10.1038/316621a0. –

DOI 10.1038/316621a0. – ISSN 1476–4687

38 LUPTON, J. E.: Hydrothermal helium plumes in the Pacific Ocean. In: *Journal of Geophysical Research: Oceans* 103 (1998), Jul., Nr. C8, S. 15853–15868. http://dx.doi.org/10.1029/98jc00146. – DOI 10.1029/98jc00146. – ISSN 0148–0227

39 In: LUPTON, J. E.: *Hydrothermal Plumes: Near and Far Field*. American Geophysical Union, 2013 ISSN 2328–8779, S. 317–346

40 MARCHESIELLO, P. ; MCWILLIAMS, J. C. ; SHCHEPETKIN, A. : Open boundary conditions for long-term integration of regional oceanic models. In: *Ocean Modelling* 3 (2001), Jan., Nr. 1–2, S. 1–20. http://dx.doi.org/10.1016/s1463-5003(00)00013-5. – DOI 10.1016/s1463–5003(00)00013–5. – ISSN 1463–5003

41 MASON, E. ; MOLEMAKER, J. ; SHCHEPETKIN, A. F. ; COLAS, F. ; MCWILLIAMS, J. C. ; SANGRÀ, P. : Procedures for offline grid nesting in regional ocean models. In: *Ocean Modelling* 35 (2010), Jan., Nr. 1–2, S. 1–15. http://dx.doi.org/10.1016/j.ocemod.2010.05.007. – DOI 10.1016/j.ocemod.2010.05.007. – ISSN 1463–5003

42 METTE, J. : *jmetteUni/aurora-0-he: Thesis version*. http://dx.doi.org/10.5281/ZENODO.15420483. Version: 2025

43 METTE, J. : *jmetteUni/aurora-plume-dispersal-figures: Thesis version*. http://dx.doi.org/10.5281/ZENODO.15420426. Version: 2025

44 METTE, J. : *jmetteUni/hy-vent: Thesis version*. http://dx.doi.org/10.5281/ZENODO.15420189. Version: 2025

45 MICHAEL, P. ; LANGMUIR, C. ; DICK, H. ; SNOW, J. ; GOLDSTEIN, S. ; GRAHAM, D. ; LEHNERT, K. ; KURRAS, G. ; JOKAT, W. ; MÜHE, R. u. a.: Magmatic and amagmatic seafloor generation at the ultraslow-spreading Gakkel ridge, Arctic Ocean. In: *Nature* 423 (2003), Nr. 6943, S. 956–961. http://dx.doi.org/https://doi.org/10.1038/nature01704. – DOI https://doi.org/10.1038/nature01704

46 PRIETO, G. A.: The Multitaper Spectrum Analysis Package in Python. In: *Seismological Research Letters* 93 (2022), March, Nr. 3, S. 1922–1929. http://dx.doi.org/10.1785/0220210332. – DOI 10.1785/0220210332. – ISSN 1938–2057

47 RAMIREZ-LLODRA, E. ; ARGENTINO, C. ; BAKER, M. ; BOETIUS, A. ; COSTA, C. ; DAHLE, H. ; DENNY, E. ; DESSANDIER, P.-A. ; EILERTSEN, M. ; FERRE, B. u. a.: Hot Vents Beneath an Icy Ocean: The Aurora Vent Field, Gakkel Ridge, Revealed. In:

Oceanography 36 (2023), Nr. 1. http://dx.doi.org/https://doi.org/10.5670/oceanog.2023.103. – DOI https://doi.org/10.5670/oceanog.2023.103

48 RÜTH, C. : *Heliumisotopen- und Neon-Messungen im Südantlantik: ozeanographische und geochemische Anwendungen*, Institute for Environmental Physics, University of Bremen, Diss., 1998

49 SCHLINDWEIN, V. ; BORNEMANN, H. (Hrsg.) ; SAWADKUHI, S. A. (Hrsg.): *The Expedition PS137 of the Research Vessel POLARSTERN to the Arctic Ocean in 2023*

50 SCHLOSSER, P. ; KROMER, B. ; EKWURZEL, B. ; BÖNISCH, G. ; MCNICHOL, A. ; SCHNEIDER, R. ; REDEN, K. von ; ÖSTLUND, H. ; SWIFT, J. : The first trans-Arctic 14C section: comparison of the mean ages of the deep waters in the Eurasian and Canadian basins of the Arctic Ocean. In: *Nuclear Instruments and Methods in Physics Research Section B: Beam Interactions with Materials and Atoms* 123 (1997), March, Nr. 1–4, S. 431–437. http://dx.doi.org/10.1016/s0168-583x(96)00677-5. – DOI 10.1016/s0168–583x(96)00677–5. – ISSN 0168–583X

51 SEA-BIRD SCIENTIFIC: *Seasoft V2:SBE Data Processing*. Sea-Bird Scientific, 2017. https://www.seabird.com/asset-get.download.jsa?id=55174002258

52 SEABIRD: *37-SMP Datasheet*. SeaBird, Sept. 2021

53 SEABIRD: *SBE 911plus Datasheet*. SeaBird, 2022

54 SHCHEPETKIN, A. F. ; MCWILLIAMS, J. C.: The regional oceanic modeling system (ROMS): a split-explicit, free-surface, topography-following-coordinate oceanic model. In: *Ocean Modelling* 9 (2005), Jan., Nr. 4, S. 347–404. http://dx.doi.org/10.1016/j.ocemod.2004.08.002. – DOI 10.1016/j.ocemod.2004.08.002. – ISSN 1463–5003

55 SÜLTENFUSS, J. ; ROETHER, W. ; RHEIN, M. : The Bremen mass spectrometric facility for the measurement of helium isotopes, neon, and tritium in water. In: *Isotopes in Environmental and Health Studies* 45 (2009), Jun., Nr. 2, S. 83–95. http://dx.doi.org/10.1080/10256010902871929. – DOI 10.1080/10256010902871929. – ISSN 1477–2639

56 TALLEY, L. D.: *Descriptive Physical Oceanography*. 6th ed. San Diego : Elsevier Science Technology, 2011. – ISBN 9780080939117. – Description based on publisher supplied metadata and other sources.

57 TESKE, A. ; REYSENBACH, A.-L. : Editorial: Hydrothermal microbial ecosystems. In: *Frontiers in Microbiology* 6 (2015). http://dx.doi.org/10.3389/fmicb.2015.00884. – DOI 10.3389/fmicb.2015.00884. – ISSN 1664–302X

58 THURNHERR, A. M. ; RICHARDS, K. J. ; GERMAN, C. R. ; LANE-SERFF, G. F. ; SPEER, K. G.: Flow and Mixing in the Rift Valley of the Mid-Atlantic Ridge. In: *Journal of Physical Oceanography* 32 (2002), Jun., Nr. 6, S. 1763–1778. http://dx.doi.org/10.1175/1520-0485(2002)032<1763:famitr>2.0.co;2. – DOI 10.1175/1520–0485(2002)032<1763:famitr>2.0.co;2. – ISSN 1520–0485

59 TURNER, J. S.: *Buoyancy Effects in Fluids*. Cambridge University Press, 1973. http://dx.doi.org/10.1017/cbo9780511608827. http://dx.doi.org/10.1017/cbo9780511608827. – ISBN 9780511608827

60 TURNER, J. ; CAMPBELL, I. : Temperature, density and buoyancy fluxes in "black smoker" plumes, and the criterion for buoyancy reversal. In: *Earth and Planetary Science Letters* 86 (1987), Nov., Nr. 1, S. 85–92. http://dx.doi.org/10.1016/0012-821x(87)90191-9. – DOI 10.1016/0012–821x(87)90191–9. – ISSN 0012–821X

61 WALKER, S. L. ; BAKER, E. T. ; RESING, J. A. ; NAKAMURA, K. ; MCLAIN, P. D.: A New Tool for Detecting Hydrothermal Plumes: an ORP Sensor for the PMEL MAPR. In: *AGU Fall Meeting Abstracts* Bd. 2007, 2007, S. V21D–0753

62 WALTER, M. ; TÜRKE, A. ; DIEHL, A. ; GERMAN, C. R. ; MERTENS, C. ; METTE, J. ; MONIEN, P. ; PRAUSE, S. ; SÜLTENFUSS, J. ; BACH, W. ; SCHLINDWEIN, V. ; BOETIUS, A. : Properties and Dispersal of a Hydrothermal Plume in a Weakly Stratified Under-Ice Environment. (2024), Nov. http://dx.doi.org/10.22541/essoar.173042129.93578183/v1. – DOI 10.22541/essoar.173042129.93578183/v1

63 WARNKE, F. ; UNLAND, E. ; HÖPPNER, L. ; DREUTTER, S. ; DORSCHEL, B. ; SCHLINDWEIN, V. : *Multibeam bathymetry processed data (Atlas Hydrosweep DS 3 echo sounder entire dataset) of RV POLARSTERN during cruise PS137, Western Gakkel Ridge, Arctic Ocean*

64 WEGENER, G. ; MOLARI, M. ; PURSER, A. ; DIEHL, A. ; ALBERS, E. ; WALTER, M. ; MERTENS, C. ; GERMAN, C. R. ; BOETIUS, A. : Hydrothermal vents supporting persistent plumes and microbial chemoautotrophy at Gakkel Ridge (Arctic Ocean). In: *Frontiers in Microbiology* 15 (2024), Oct. http://dx.doi.org/10.3389/fmicb.2024.1473822. – DOI 10.3389/fmicb.2024.1473822. – ISSN 1664–302X

65 WIKIROMS: *Vertical S-coordinate*. https://www.myroms.org/wiki/Vertical_S-coordinate. Version: Jul. 2019

66 XU, G. ; GERMAN, C. R.: Dispersion of deep-sea hydrothermal plumes at the Endeavour Segment of the Juan de Fuca Ridge: a multiscale numerical study. In: *Frontiers in Marine Science* 10 (2023), jul. http://dx.doi.org/10.3389/fmars.2023.1213470. – DOI 10.3389/fmars.2023.1213470

Acknowledgements

I hereby want to thank the people, who helped me preparing this work: First and foremost my supervisor Maren Walter, for offering me this topic and for the amazing experiences that came along with it. I also would like to thank Guangyu Xu for guiding me through the ROMS setup and providing scripts and examples and Gunter Wegener for his support in various administrative and content-wise matters. I want to thank Christian Mertens for comments, explanations and guidance and him as well as Torsten Kanzow for reviewing this work. Thank you to Anja Gatzka for her help in understanding the PEP regulations and Janina for printing the documents. Last but not least, thank you to all persons who provided useful comments and helped to improve this work and who were with me along the way. Have a cup of tea.

Figure 1.: Eastfrisian Tea with your very personal "Wulkje" plume. Figure from https://denise-bucketlist.de/ostfriesische-teezeremonie-anleitung, 2025-05-15.